AD NUMBER

AD463240

NEW LIMITATION CHANGE

TO

Approved for public release, distribution unlimited

FROM

Distribution authorized to U.S. Gov't. agencies and their contractors; Administrative/Operational Use; 15 JAN 1965. Other requests shall be referred to Defense Atomic Support Agency, Washington, DC.

AUTHORITY

DASA ltr 4 Oct 1966

DASA REPORT NUMBER 1613

FINAL REPORT

CONTRACT NO. DA-49-146-XZ-145

DEPARTMENT OF DEFENSE

DEFENSE ATOMIC SUPPORT AGENCY

WASHINGTON 25, D. C.

463240

"Analysis of ARGUS/Explorer IV Records"

JANUARY 15, 1965

SAINT LOUIS UNIVERSITY

PHYSICS DEPARTMENT

SAINT LOUIS, MISSOURI 63103

FOR ERRATA

AD 463240

THE FOLLOWING PAGES ARE CHANGES

TO BASIC DOCUMENT

SAINT LOUIS
UNIVERSITY
"FIRST WEST OF THE MISSISSIPPI"

DEPARTMENT OF PHYSICS

221 NORTH GRAND BOULEVARD
SAINT LOUIS, MISSOURI 63103

June 1, 1965

NOTICE

The attached should be inserted as the last page for document

DASA Report Number 1613

Contract No. DA-49-146-XZ-145

"Analysis of ARGUS/Explorer IV Records"

20 copies of above document were forwarded to you on 17 May 1965.

Unclassified

Security Classification

DOCUMENT CONTROL DATA - R&D

(Security classification of title, body of abstract and indexing annotation must be entered when the overall report is classified)

1. ORIGINATING ACTIVITY (Corporate author) SAINT LOUIS UNIVERSITY	2a. REPORT SECURITY CLASSIFICATION Unclassified 2b. GROUP

3. REPORT TITLE

"Analysis of ARGUS/Explorer IV Records"

4. DESCRIPTIVE NOTES (Type of report and inclusive dates)

Final 1 April 1963 - 15 January 1965

5. AUTHOR(S) (Last name, first name, initial)

A. H. Weber, R. M. Delaney, J. F. Fennell, J. A. George, D. J. Manson, S.J., J. R. Ockersz, S.J., J. M. Paikeday, (Saint Louis University); J. K. Bock, (Ballistic Research Laboratories).

6. REPORT DATE	7a. TOTAL NO. OF PAGES	7b. NO. OF REFS
January 15, 1965	94	21

8a. CONTRACT OR GRANT NO. DA-49-146-XZ-145 b. PROJECT NO. c. d.	9a. ORIGINATOR'S REPORT NUMBER(S) DASA Report Number 1613 9b. OTHER REPORT NO(S) (Any other numbers that may be assigned this report)

10. AVAILABILITY/LIMITATION NOTICES

Qualified requestors may obtain copies of this report from DDC.

11. SUPPLEMENTARY NOTES	12. SPONSORING MILITARY ACTIVITY
None	Department of Defense Defense Atomic Support Agency

13. ABSTRACT

The present report contains further analysis of the radiation data obtained by satellite Explorer IV, 1958 Epsilon, especially for ARGUS charged particle geomagnetic field trapping. The present work was undertaken to supplement the previous analysis (Lundquist, Naumann and Weber, J. Geophys. Res. 67, 4125 (1962)) for the naturally trapped radiation.

DD FORM 1 JAN 64 1473

Unclassified

Security Classification

QUALIFIED REQUESTORS MAY OBTAIN COPIES OF THIS REPORT FROM DDC.

"DASA Report Number 1613"

Final Report

"Analysis of ARGUS/Explorer IV Records"

Defense Atomic Support Agency, Washington, D. C., 20301;

Contract No. DA-49-146-XZ-145: "Research to extract all remaining significant information from the ARGUS/Explorer IV records."

Period of contract: 1 April 1963 - 15 January 1965

Personnel

A. H. Weber, Chief Investigator
R. M. Delaney, Co-Chief Investigator
J. F. Fennell
J. A. George
D. J. Manson, S.J.
J. R. Ockersz, S.J.
J. M. Paikeday
(all above are on staff, Physics department, Saint Louis University)

J. K. Bock, Ballistic Research Laboratories
Aberdeen Proving Ground, Maryland

January 15, 1965

Saint Louis University

Physics Department

St. Louis, Missouri 63103

Final Report - Defense Atomic Support Agency Contract No. DA-49-146-XZ-145

Acknowledgments

1. This research was supported by the Advanced Research Projects Agency Nuclear Test Detection Office and was monitored by the Defense Atomic Support Agency under Contract No. DA-49-146-XZ-145. In addition to the funding support of DASA, the authors wish to express their considerable appreciation of the valued cooperation and help of Major Charles W. Hulburt, and of Lieutenant Russell F. Kappenman of the same division.

   The assistance rendered by Major J. E. Mock, formerly of the Defense Atomic Support Agency, Washington, D.C. during the initial phase of the present contractual work is acknowledged also with gratitude.

2. Dr. Juergen K. Bock of the Nuclear Physics Branch of the Ballistic Research Laboratories, Aberdeen Proving Ground, Maryland, rendered essential scientific aid in the present work and is listed as a co-author of the present report. E. O. Baicy, Chief of the Nuclear Physics Branch of BRL was instrumental in effecting scientific liaison between his branch and the group in the physics department of Saint Louis University. The assistance of BRL in this scientific work was indispensable.

3. The Yalem Computer Center, Saint Louis University, rendered invaluable services via unrestricted time on the IBM-1620 Computer.

4. Washington University Computing Facilities, through National Science Foundation Grant G-22296, rendered valuable assistance and support of the present project during the last three months of the contract period.

5. The assistance of Messrs. Roy Cochran and D. G. Aichele of the staff of the Computation Laboratory, George C. Marshall Space Flight Center, Huntsville, Alabama is especially acknowledged. These computer experts provided a new group of "playbacks" of the set of telemetry tapes selected for analysis in the present work. These playbacks were much superior in elimination of noise and clarity of record to the group of records which were originally available. The availability of these new high quality playbacks enabled considerable improvement in the analysis.

6. Dr. Charles A. Lundquist (now at Smithsonian Astrophysical Observatory, Cambridge, Massachusetts) and Messrs. Robert J. Naumann and Stanley A. Fields of the Research Projects Laboratory, George C. Marshall Space Flight Center, Huntsville, Alabama made essential contributions to the present work.

Contents

Abstract

The present report contains further analysis of the radiation data obtained by satellite Explorer IV, 1958 Epsilon, especially for ARGUS charged particle geomagnetic field trapping. The present work was undertaken to supplement the previous analysis (Lundquist, Naumann and Weber, J. Geophys. Res. 67, 4125 (1962)) for the naturally trapped radiation.

Directional count-rates (using the original telemetry data from the scintillation counter, Detector A, Channel 2) as a function of time and θ (angle between counter and plane perpendicular to geomagnetic field) are plotted and analysed with comparison of Natural and ARGUS trapping for two passes of the satellite over Huntsville, Alabama. Complete analysis of all data acquired by Pass 414 (including ARGUS Event I data) is presented as an example of the detailed analytic procedure which is required, with partial analysis of Pass 454 (Event II) included for comparison. The true (corrected for deadtime, effective counter area and efficiency) count-rate vs θ curves were reduced analytically to obtain angular distributions of the directional charged particle flux densities, $J(\theta')$ ($cm^{-2}sec^{-1}ster^{-1}$) vs θ' (angle between direction of J and counter axis).

The results indicate that the Natural angular flux density distributions are roughly constant in shape for nearly the same region in space in agreement with previously published results. For ARGUS regions the angular distribution of the directional radiation is determined for time periods in which the background omnidirectional pene-

trating radiation (recorded by the G-M counters, Channels 1 and 3) is sensibly constant. Sudden changes in the omnidirectional background counting rate are shown to modify the shapes of the count-rate versus θ curves which correspond to individual modulations of the scintillation detector count-rates for Pass 414 in the ARGUS region. It is concluded on the basis of the limited data completely analysed that the corresponding angular distribution of the directional radiation in space, and therefore also the related mirror-point distributions, for ARGUS trapped particles are affected quite markedly by the omnidirectional penetrating radiation present as background. ARGUS particle fluxes observed were $1.0\text{-}1.9 \times 10^8$ and $.65 \times 10^8$ $cm^{-2}sec^{-1}ster^{-1}$ for Passes 414 (Event I) and 454 (Event II) respectively.

Omnidirectional count-rates (Detectors C, unshielded G-M counter, Channel 3; D, shielded G-M counter, Channel 1) versus time are presented for Passes 414, 415, 416, 427, 440, 453, 454, 466, and 479 following Event I, and for Passes 453, 454, 455, 466 and 479 following Event II.

Some broad energy dependence of the omnidirectional radiation is shown by plots of both the ratios of, and the differences between, the unshielded and shielded G-M count-rates which were obtained for the same set of Explorer IV passes. Time decay curves of the omnidirectional ARGUS trapped radiation were constructed for constant L both for the unshielded G-M count-rates and the ratio of unshielded to shielded G-M count-rates. The ratio curves for L = 1.72 and 1.73 (Fig. 5.4) indicate an unexplained radiation hardening-softening-hardening sequence.

The Explorer IV roll-period history was studied in some detail in the region of the reported (Naumann, 1961) anomalous behavior. Using a

power spectrum analysis of the count-rate modulations of the directional scintillation counter (Detector A) it is shown, as suggested by J. Bock (1964), that there is no anomalous roll-period discontinuity if beat and harmonic frequencies (of the roll and tumble rates) are recognized and eliminated (see Fig. 3.3 of present report).

Considerably more data remains to be analysed to verify more positively or modify the tentative conclusions concerning directional particle distributions for both the natural (especially pre ARGUS) and ARGUS trapping, to determine natural and ARGUS mirror-point distributions and trapping mechanisms, and to explain certain features of the omnidirectional radiation energy dependence.

"Analysis of ARGUS/Explorer IV Records"

Chapter 1

Introduction

The present report includes a further analysis of the large amount of geomagnetically trapped particle radiation (due to both natural and ARGUS injection) data obtained by Explorer IV, satellite 1958 Epsilon, during July - September 1958.

A previous report (Lundquist, Naumann, and Weber, J. Geophys. Res. 67, 4125 (1962)) presented an analysis of the naturally trapped radiation as detected by the directional scintillation counter (Detector A, Channel 2) on board the satellite and telemetered from Explorer IV to the Huntsville, Alabama ground station.

The present work was centered on ARGUS type trapping and was intended to supplement the previous report. The objectives were to apply analysis similar to that employed for the naturally trapped particles (op. cit.) to the directional ARGUS trapped particles and also to attempt further analysis of the omnidirectional penetrating radiations, both for natural and ARGUS trapping, using the data obtained by the G-M detectors (Detectors C and D, Channels 3 and 1).

The following chapters of the present report develop these objectives and present all results so far obtained.

Chapter 2

Satellite Explorer IV Instrumentation, Motion and Telemetry

2.1 Instrumentation. Calibrations

A complete description of the detection instrumentation has been published by Van Allen et al, (1959 a, b). A block diagram showing the arrangement of the 4 detectors (A, B, C, D) and the corresponding telemetry channels 2 and 5, 4, 3, 1 is shown by Fig. 2.1. A sketch of the physical arrangement of components in the satellite is shown by Fig. 2.2. A summary of the characteristics of the four radiation detectors is given in the literature (Table 1, Van Allen et al, 1959b).

Both the scintillation counter and the G-M counter count rates must be corrected for deadtimes (op. cit.). For Detector A, the plastic scintillator-photomultiplier counter and associated electronics, the deadtime correction is accomplished by the equation

$$C = C_{obs} / (1 - \tau_0 C_{obs}) ; \qquad (2.11)$$

where C_{obs} is the observed counting rate, C is the true counting rate, and τ_0 is the deadtime (92 microseconds). For Detector C, the Anton 302 G-M counter, the equation

$$C_{obs} = C\, e^{-\tau_1 C} , \qquad (2.12)$$

where τ_1 (more properly defined as deionization time, rather than deadtime) = 62.5 ± 1.3 microseconds, was used (op. cit.). A plot of Eq. (2.12) is shown by Fig. 2.3. A discussion of the actual deadtimes used in the present analysis follows.

In the present work both the τ_D and τ_1 values of Van Allen were checked. The value of τ_1 = 62.5 ± 1.3 microseconds was confirmed. However, for Detector A count-rates near a maximum of 10^4 per sec were observed in the telemetry records (Pass 414). Considering 10^4 per sec as the saturation counting rate yields (setting denominator of Eq. (2.11) to zero) τ_D = 100 microsec. In turn, Baicy et al (1962) determined τ_D as 112 microsec. Since Baicy's value of τ_D would permit a maximum C_{obs} of about 9000 per sec only, it was concluded (for the present work) that the prototype detector calibrated by Baicy had a τ_D differing from that of the detector actually flown in Explorer IV.

It was decided, in the present analyses, to use τ_D = 100 microsec for Detector A, a somewhat arbitrary decision. Such decision is however necessary in the absence of detailed calibration information. It should be emphasized that any uncertainty in τ_D will be reflected in the shape of the directional flux density $J(\theta')$ curves of Chapter 4. The maxima of these $J(\theta')$ curves, near $\theta' = 0$, will be especially sensitive to the τ_D value used.

Additional calibration information especially for the directional scintillation counter (Detector A) was determined for a prototype package (Baicy et al, 1962), as follows.

1. Detector A. The pulse height discriminator of the Detector A circuit (Fig. 2.1) had a threshold of 700-KeV for electrons. The deadtime for the circuit was measured electronically as 112 microseconds. The discriminator threshold for gamma-rays was between 0.66 and 1.17 MeV. The gamma radiation was penetrating enough so that small shielding effects

were not observed. No multiple scattering into the detector from other parts of the package was evident. The x-ray calibration established a 1 MeV photonic threshold; detector window response curves demonstrated the existence of a directional plus a penetrating omnidirectional component, and with increasing energies, the omnidirectional component obscured the directional component. The calibration indicated that the half-width angular response curve for photonic radiation is about 30% broader than that obtained for electrons (Fig. 4.2). Over the measured energy range (0.2 to 1.5 MeV), the angular response curves were found to be almost independent of energy. The discriminator transmission efficiency ϵ and effective area, A_{eff} for β-rays were

$$\epsilon = 0, \quad \epsilon A_{eff} = 0 \quad \text{for} \quad E < 700 \text{ KeV}, \tag{2.13}$$

$$\epsilon = 85\%, \quad \epsilon A_{eff} = 0.52 \text{ mm}^2 \quad \text{for} \quad E > 700 \text{ KeV} \tag{2.14}$$

The calibration data noted by Eqs. (2.13 and 2.14) were employed in the present work for the calculations of directional electron fluxes. For an average photon energy of 1.25 MeV, the omnidirectional factor was

$$(\epsilon A_{eff})_{omni} = 6.29 \times 10^{-2} \text{ mm}^2 . \tag{2.15}$$

2. Detectors C and D. The counters were identical Anton type 302 G-M tubes located side by side with a center line separation of 3.6 cm, with Detector D having additional shielding (Van Allen et al, 1959b).

The output of the G-M tubes and associated circuitry began to saturate at approximately 2000 counts/sec for photonic radiation. An analysis of observed counting rate for pass 414 indicated saturation was at approximately 5800 counts/second. A further increase of radiation flux produced a decrease of count-rate. The G-M tubes were much more efficient for photonic radiation than Detector A. No counts were obtained for electrons up to 1.5 MeV due to the satellite shell stopping power of 1.2 gm/cm^2. Because of low conversion efficiency, it was not possible to observe any bremsstrahlung produced by incident electrons on the satellite shell. The omnidirectional effective areas for Detectors C and D were found for photons (Baicy et al, 1962).

Detector C was shielded by 1.2 gm/cm^2 of stainless steel. If the shielding were aluminum, the extrapolated range would be given as a function of energy by Marshall and Ward (1937)

$$R_e = 0.526E - 0.094, \tag{2.16}$$

where R_e is measured in gm/cm^2 and E in MeV. Equation (2.16) yields the absorber thickness for 10 percent transmission for electrons of energy E. The range for 50 percent transmission of electrons is, same units as Eq. (2.16),

$$R_{1/2} = 0.38E - 0.1. \tag{2.17}$$

To obtain the thickness of aluminum equivalent to a given thickness of another absorber of nucleon number A, the absorber thickness is multiplied by the factor (Husain and Putnam, 1957)

$$(Z/13)^{1/3}\,(27/A). \tag{2.18}$$

The 1.2 gm/cm^2 of stainless steel (Z = 26) therefore are equivalent to 1.46 gm/cm^2 of aluminum, the extrapolated range corresponding to 2.95 MeV electrons. For 50 percent transmission the electron energy is 4.1 MeV. These ranges correspond favorably with the published values (Table 1, Van Allen et al, 1959b).

The equilibrium flux-energy beta-ray spectrum of U^{235} was reported by Carter et al (1959) as

$$N(E) = 3.88 \exp (-0.575E - 0.055E^2), \qquad (2.19)$$

where E is the β-ray kinetic energy in MeV, and N(E) is the absolute differential spectral intensity of β-rays in electrons per fission per MeV. The integrated fluxes have been obtained by numerical integration (Van Allen et al, 1963) whence the fraction of electrons of energy greater than 3 MeV is 7.7×10^{-2}.

Detector D had 1.6 gm/cm^2 of lead in addition to the 1.2 gm/cm^2 of stainless steel. The total shielding is equivalent to 3.28 gm/cm^2 of aluminum which corresponds to an extrapolated range of 6.2 MeV electrons. The fraction of electrons of energy greater than 6.2 MeV is 1.6×10^{-3}, approximately.

The efficiency of the G-M tubes for the direct counting of penetrating electrons and for counting non-penetrating electrons via intermediate bremsstrahlung, assuming a fission spectrum of β-rays, should be investigated. Motz and Carter (1963) studied the response of an Anton 302 G-M counter to a fission β-spectrum. They found that up to about 2 gm/cm^2 of lead absorber, the transmission curves were as expected for β-transmission; however, for greater thicknesses the transmission was enhanced by bremsstrahlung. The shielding of Detector D is equivalent to 2.16 gm/cm^2 of lead thus indicating bremsstrahlung production should be considered.

2.2 Body motion of Explorer IV

The satellite Explorer IV was injected into orbit July 26, 1958 at approximately 1500 UT at a longitude of 264.82 degrees East, a latitude of 12.95 degrees North and an altitude of 368.2 km. The initial perigee of the orbit was 163 miles, the apogee 1380 miles, period 110.27 minutes; the inclination to the equatorial plane 50.29 degrees. Eccentricity of the orbit was 0.1297. The nodal shift per revolution was 27.9 degrees. The injection pitch flight angle was 89.6 degrees, the yaw flight angle 0.8 degrees.

Figure 2.2 is a sketch of the satellite showing dimensions and configuration. The total weight was 38.4 lbs of which 25.8 lbs was instrumentation. The center of gravity was located 45 in. from the nose. The moment of inertia about the long or Z'-axis was 0.50 in. lb sec^2, about the X'-axis, 42.0 in. lb sec^2. The cross sectional area was 30.7 sq in., the maximum visible projected area, 458 sq in. The skin of the satellite was stainless steel which had been given a fine sandblast resulting in an emissivity 0.54 and 0.46 for the wavelength range 8-12 microns.

Electrically the skin of the satellite was divided into three insulated sections as shown in Fig. 2.2. The nose cone and instrument section (designated by L) served as the antenna (asymmetrical dipole) for the low power (10 mw) 108.00 mc-sec^{-1} transmitter. The two middle sections served as the antenna (symmetrical dipole) for the 108.03 mc-sec^{-1} high power (25 mw) transmitter. The resulting antenna radiation patterns are sketched in Fig. 2.4.

At the separation of the second stage the satellite was spinning about the Z'-axis (Fig. 2.2) at a rate of 24π radians/sec. This Z'-axis spin represents a maximum energy configuration. As rotational energy is dissipated (through vibrational friction since the satellite is not completely rigid) conservation of angular momentum required an increase in moment of inertia about the L-axis to compensate for decrease in angular velocity. Hence the motion changes from pure spin (or roll) about the (longitudinal) symmetry axis (A, Fig. 2.2) of the satellite to a more complicated motion of spin and tumble. The rate at which this transition occurs depends on the energy dissipation rate. The transition from the initial pure spin to nearly pure flat or propeller-like motion was observed to occur in about 9 days. This transition was confirmed by the calculations of Snoddy (1959) which showed that the temperature variations of the satellite could be explained by the increased average surface area presented to the sun if the opening angle, between the pure spin axis and the spin-tumble axis, θ (Fig. 2.5) would increase about 10 degrees per day. The transition from maximum to minimum rotational energy is treated by Goldstein (1959), Slater and Frank (1947), and others. Using the Euler angles as described by Slater and Frank (op. cit.) the following important results can be derived

$$L = I_{Z'}\omega_{Z'}/\cos\theta\,;$$

$$\dot{\phi} = I_{Z'}/I_{X'}(\omega_{Z'})_0\,,\quad I_{X'} = I_{Y'}\,;$$

$$\dot{\phi} = I_{Z'}/I_{X'}(\omega_{Z'}/\cos\theta)\,, \tag{2.21}$$

In Eqs. (2.21) the primes refer to the satellite fixed rotating coordinate system Fig. 2.5 and the angular momentum vector $\hat{L}$ is considered to be constant for the present and its direction used to define a space fixed Z -axis as shown in Fig. 2.5, where X and Y form a right hand space fixed coordinate system with Z. If energy is dissipated the Z' -axis performs a torque-free precession about $\hat{L}$ with precession rate $\dot{\phi}$ where ϕ is the Euler angle measured in the X-Y plane (Fig. 2.5) and is the angle from the space fixed X-axis to the line of nodes, θ is the angle (Z, Z') or the opening angle of the precession. The third Euler angle ψ is the angle in the plane of rotation about Z' from the line of nodes to the rotating satellite fixed X'-axis. By the first of Eqs. (2.21) if ω_z, decreases, $\cos\theta$ must decrease and θ increase. The precession angular velocity $\dot{\phi}$ is constant and may be evaluated from the second of Eqs. (2.21), the initial condition when rotation is about the Z -axis only. Since the ratio of the transverse moment of inertia to the longitudinal is 84, the precession frequency is 1/84 of the initial spin rate of 24 π radians/sec. or 0.286 π radians/sec. (period, 7 secs). When the motion has degraded to the pure propeller-type (termed "tumble" as opposed to "spin-tumble") motion, the corresponding frequency is termed the tumble frequency ($\dot{\phi}$ is the corresponding tumble angular velocity) and has been measured as described in Sec. 3.3 by observing the frequency of r-f signal fading at such times when the satellite is properly orientated relative to the receiving station. The satellite continues to have a slight angular spin velocity $\dot{\psi}$ about the Z' -axis. The period of this spin or roll motion was observed to vary in magnitude during the lifetime of the satellite from 1

to approximately 100 secs. The combination of the spin and tumble motions result in the sweeping of the onboard radiation counters over almost all directions in space; in particular the directional counter (Detector A) was able to observe counting rates at all angles relative to the geomagnetic field direction between 0 and $\pi/2$. The analysis of directional radiation flux in space is seen therefore to depend on obtaining with good precision the orientation of the scintillation counter with respect to the magnetic flux density $\hat{B}$ as a function of time. During the time of acquisition of the data analyzed in the present report the satellite remained in the flat propeller-like configuration and rotation about the angular momentum vector will always be referred to as tumble (velocity or rate, $\dot{\phi}$) and motion about the Z' -axis will be referred to as spin (or roll) (velocity or rate, $\dot{\psi}$), as has been noted above.

2.3 Interpretation of satellite Explorer IV telemetry data

Figure 2.6 is a reproduction of a portion of a record of the telemetry information received from the satellite at Huntsville, Alabama on August 27, 1958 following 0416 UT, for the region of ARGUS trapping. The radiation counter data shown was recorded on magnetic tape and played back for the pen on paper recording using electronic filters suitable for reducing noise. The variations in the signal represent the abrupt changes in frequency of the audio channel modulating the carrier of one of the transmitters. For example, the first line of information (Channel 1) represents audio switching back and forth from 370 to 430 cycles/sec. Each frequency switch follows the accumulation of 32 counts from the shielded G-M counter, Detector D (reference, Fig. 2.1). Similarly, changes in the second line (Channel 2) of information follow the accumulation of 1024 counts (per frequency switch) of the scintillation counter, Detector A; the third line (Channel 3) shows frequency switching following the accumulation of 1024 counts (per switch) for the unshielded G-M counter, Detector C. Detector A is the directional counter and the rapid changes, or modulations, of counting rate of Channel 2 correspond to the changing orientation of the counter axis with respect to the magnetic field direction as noted in Sec. 3.1.

Figure 2.7 illustrates the r-f field strength information received at the Huntsville ground station. This information is used to determine the orientation of the satellite and its radiation counters relative to the geomagnetic field direction (see Chap. 3). Each telemetry record

also contains a recording (not shown in Figs. 2.6, 2.7) of the time signal from WWV, permitting real time determinations to 0.05 sec.

Records similar to Figs. 2.6 and 2.7 were reduced for Passes 414, 415, 416, 427, 428, 440, 441, 453, 454, 455, 466, 479, 492, 505, and 518 by using a Telecomputing digitizer. An initial reference time t_o was established for each time interval T (24 secs). N is the number of digitizer counts per 24 sec interval and $(n_{i+1} - n_i)$ is the number of digitizer counts per frequency change. These data were supplied to an IBM 1620 computer along with the scaling factor S (noted on Fig. 2.1) and used to compute the observed count rate (counts/sec), as follows

$$C_{obs} = NS/2T(n_{i+1} - n_i), \tag{2.31}$$

and the corresponding time t_i is calculated by

$$t_i = t_o + (n_i + n_{i+1}).(T)/2N \tag{2.32}$$

S is divided by 2 since S is the number of counts accumulated during a full cycle of two frequency switches. The Fortran program used for the calculations of Eqs. (2.31) and (2.32) is designated as Program 2.1 (all computer programs used in the present work are available at Physics department, Saint Louis University, St. Louis, Missouri). The count rate vs time computer output for Program 2.1 was plotted with a Dymec data plotting system. Figure 2.9 includes the resulting observed count-rate vs time for the directional scintillation counter (Channel 2,

Detector A) as Explorer IV traversed a region of naturally injected geomagnetically trapped particles a short time (about 6 minutes) before the satellite entered the artifically injected ARGUS shell (Pass 414). Figures 2.10 and 2.11 are similar plots for this ARGUS penetration (telemetry playback record shown by Fig. 2.6).

Figures 2.9 and 2.10 include also (Upper curves) plots of $\cos^4\theta$ (θ , angle between scintillation counter axis and the plane perpendicular to the geomagnetic field direction) vs time following the suggestion of J. Bock of the Ballistics Research Laboratories; θ as a function of time is determined by Eq. (3.11). It is interesting to note that the modulations of the observed count rates vs time (Figs. 2.9, 2.10 Lower) are rather well represented by the trigonometric function (Figs. 2.9, 2.10 Upper) since the calculation of by Eq. (3.11) is based on experimentally determined parameters.

As noted in the caption for Fig. 2.10, the Detector A count-rate modulations were individually (a through q, Figs. 2.10 (Lower) and 2.11) smoothed and least-square fitted by 4th degree polynomials, using computer Program 2.2, of the form

$$A_0 + A_1 t + \ldots A_n t^n \qquad (2.33)$$

To interpret the nulls in the ground station r-f field strength traces shown by Fig. 2.7 it is helpful to consider two cases with reference to the satellite antenna radiation patterns shown by Fig. 2.4. First, consider the receiver antenna in the plane of tumble of the satellite with $\hat{U} \perp \hat{L}$ as shown by Fig. 2.8 Upper. Nulls in the field strength pattern for each transmitter occur whenever the nose or

tail of the satellite points toward the receiver producing the field strength pattern shown by traces 6 (due to 108.03 mc-sec^{-1} transmitter; reference, Fig. 2.4 Lower) and 7 (due to 108.00 mc-sec^{-1} transmitter; reference, Fig. 2.4 Upper). Second, consider the receiver antenna in a plane perpendicular to the plane of tumble of the satellite with $\hat{U} \parallel \hat{L}$ (Fig. 2.8 Lower). The satellite antenna radiation patterns shown by Fig. 2.4 produce no nulls for either transmitter antenna. Instead, because both the transmitter antennas and the receiving antenna are linearly polarized, nulls occur twice for every revolution of the satellite about $\hat{L}$ when the plane of polarization of the transmitting antennas and the receiving antenna are perpendicular. These polarization nulls are characterized by lack of the extra side nulls shown for the "nose" nulls by Fig. 2.7 Lower. Polarization nulls are not seen in Fig. 2.7 because the line-of-sight vector $\hat{U}$ was perpendicular approximately to the angular momentum vector $\hat{L}$.

Naumann (1961) was able to use r-f field strength information as described in the preceeding paragraph together with known directions for the line-of-sight vector $\hat{U}$ (refer Eq. 3.28) from the receiving station to determine the time history orientation of the angular momentum vector $\hat{L}$. On August 18, 1958 the antenna system at the Huntsville ground station for the 108.03 mc receiver was modified to form a variably polarized array which changed its polarization as the satellite passed overhead. This arrangement allowed use of the variation of the amplitude of the nulls with the variation of the plane of polarization of the receiving antenna to yield additional and more accurate information on the direction of $\hat{L}$. The directions of $\hat{L}$ used

to analyze the passes in this report are those of Naumann (1961). The direction of $\hat{L}$ was found to be not constant as expected but varied slowly from day to day; however for telemetry acquisition periods up to some 20 min the direction could be considered constant. Naumann (1962) has suggested an explanation of the observed variation of angular momentum in terms of the interaction of the magnetic moment of the satellite with the earth's magnetic field. The orientations of $\hat{L}$ determined in this way checked with Snoddy's (1959) prediction of variations in temperature due to the variation in satellite projected area toward the sun and orbital trajectory variations due to presentation of different frontal drag orientations.

The rate at which r-f nulls occurred when the line-of-sight vector $\hat{U}$ was nearly in the plane of tumble variation permits the calculation of the satellite tumble rate if the variation due to motion along the trajectory is corrected for (see Sec. 3.3, Eq. 3.32). The tumble period actually observed is 6.90 sec approximately (see Fig. 2.7), nearly 7 sec as calculated (Eqs. 2.21, Sec. 2.2).

Fig. 2.1 Block diagram of radiation Detectors A, B, C, D and corresponding telemetry Channels 2 & 5, 4, 3, 1. The numbers 2048, 16, DC, 2048, 64 designate the scaling factors for a complete cycle (2 switches) for each channel. (Van Allen et al, 1959).

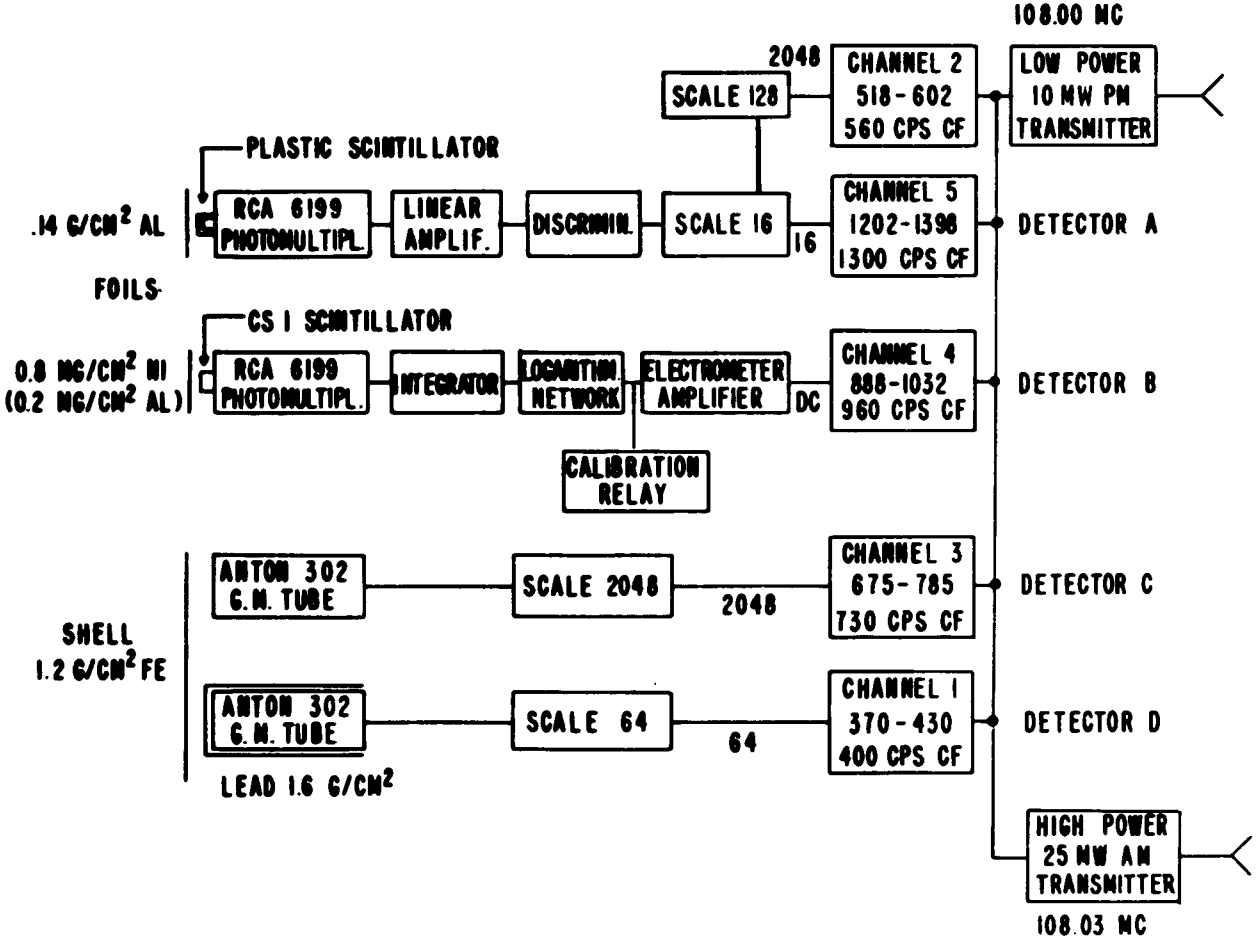
108.00 MC
2048
SCALE 128
CHANNEL 2
518-602
560 CPS CF
LOW POWER
10 MW PM
TRANSMITTER
PLASTIC SCINTILLATOR
.14 G/CM² AL
FOILS
RCA 6199
PHOTOMULTIPL.
LINEAR
AMPLIF.
DISCRIMIN.
SCALE 16
16
CHANNEL 5
1202-1398
1300 CPS CF
DETECTOR A
CS I SCINTILLATOR
0.8 MG/CM² NI
(0.2 MG/CM² AL)
RCA 6199
PHOTOMULTIPL.
INTEGRATOR
LOGARITHM.
NETWORK
ELECTROMETER
AMPLIFIER
DC
CHANNEL 4
888-1032
960 CPS CF
DETECTOR B
CALIBRATION
RELAY
SHELL
1.2 G/CM² FE
ANTON 302
G.M. TUBE
SCALE 2048
2048
CHANNEL 3
675-785
730 CPS CF
DETECTOR C
ANTON 302
G.M. TUBE
SCALE 64
64
CHANNEL 1
370-430
400 CPS CF
DETECTOR D
LEAD 1.6 G/CM²
HIGH POWER
25 MW AM
TRANSMITTER
108.03 MC

Fig. 2.2 Sketch showing shape, size and packaging of the Explorer IV satellite.

Upper. Complete satellite in 3 sections: nose cone and instrumentation section (together designated by L), propellant and exhaust nozzle (remaining length).

Lower. Nose cone and instrumentation section only. $\hat{A}$, satellite symmetry-axis vector (in direction of z'); $\hat{P}$, Detector A (directional scintillation counter) axis direction.

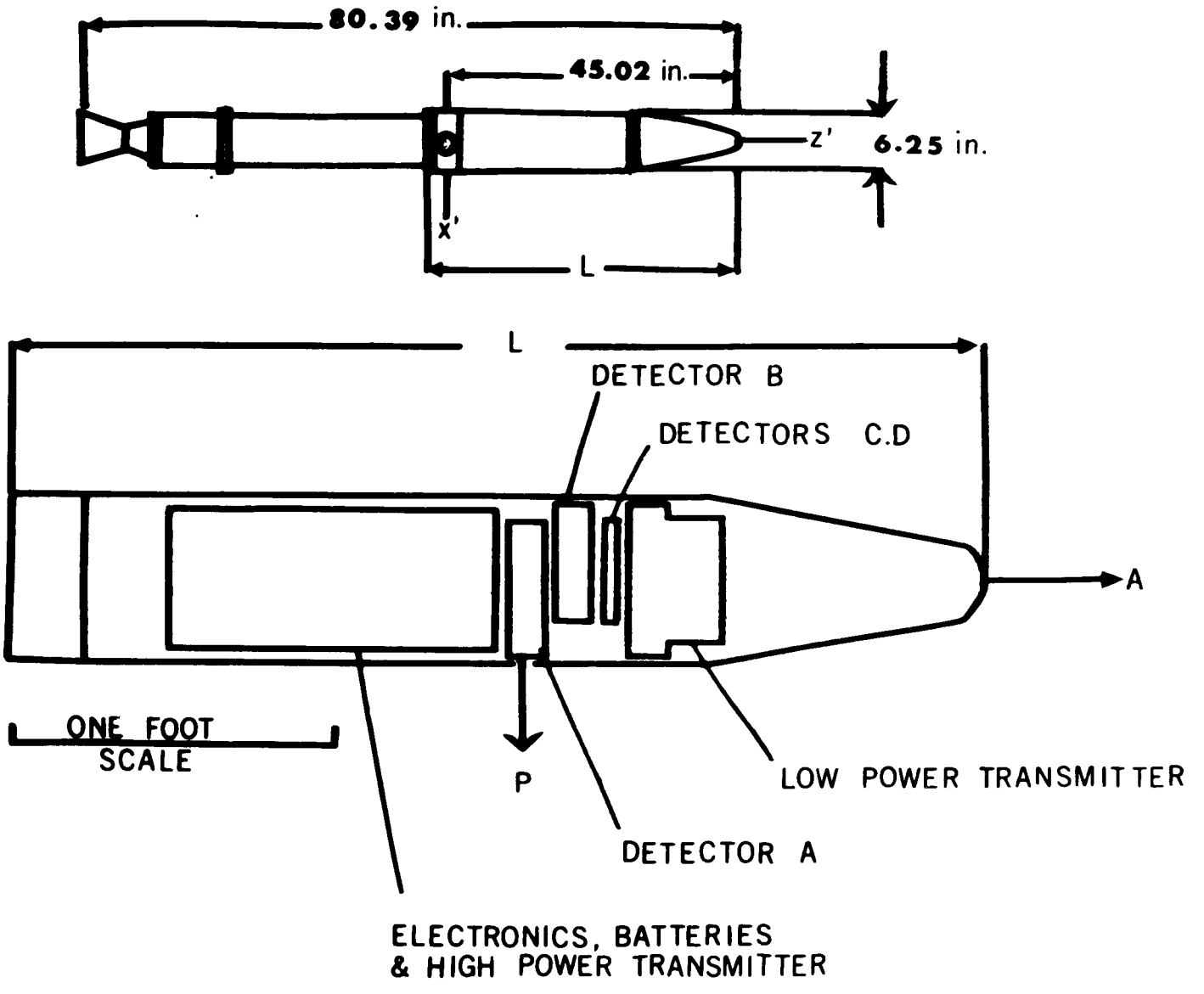
80.39 in.
45.02 in.
z'
6.25 in.
x'
L
L
DETECTOR B
DETECTORS C.D
A
ONE FOOT
SCALE
P
LOW POWER TRANSMITTER
DETECTOR A
ELECTRONICS, BATTERIES
& HIGH POWER TRANSMITTER

Fig. 2.3 Plot of Eq. (2.12), true omnidirectional counting rate C vs observed counting rate C_{obs} for Detector C, Anton 302 G-M counter.

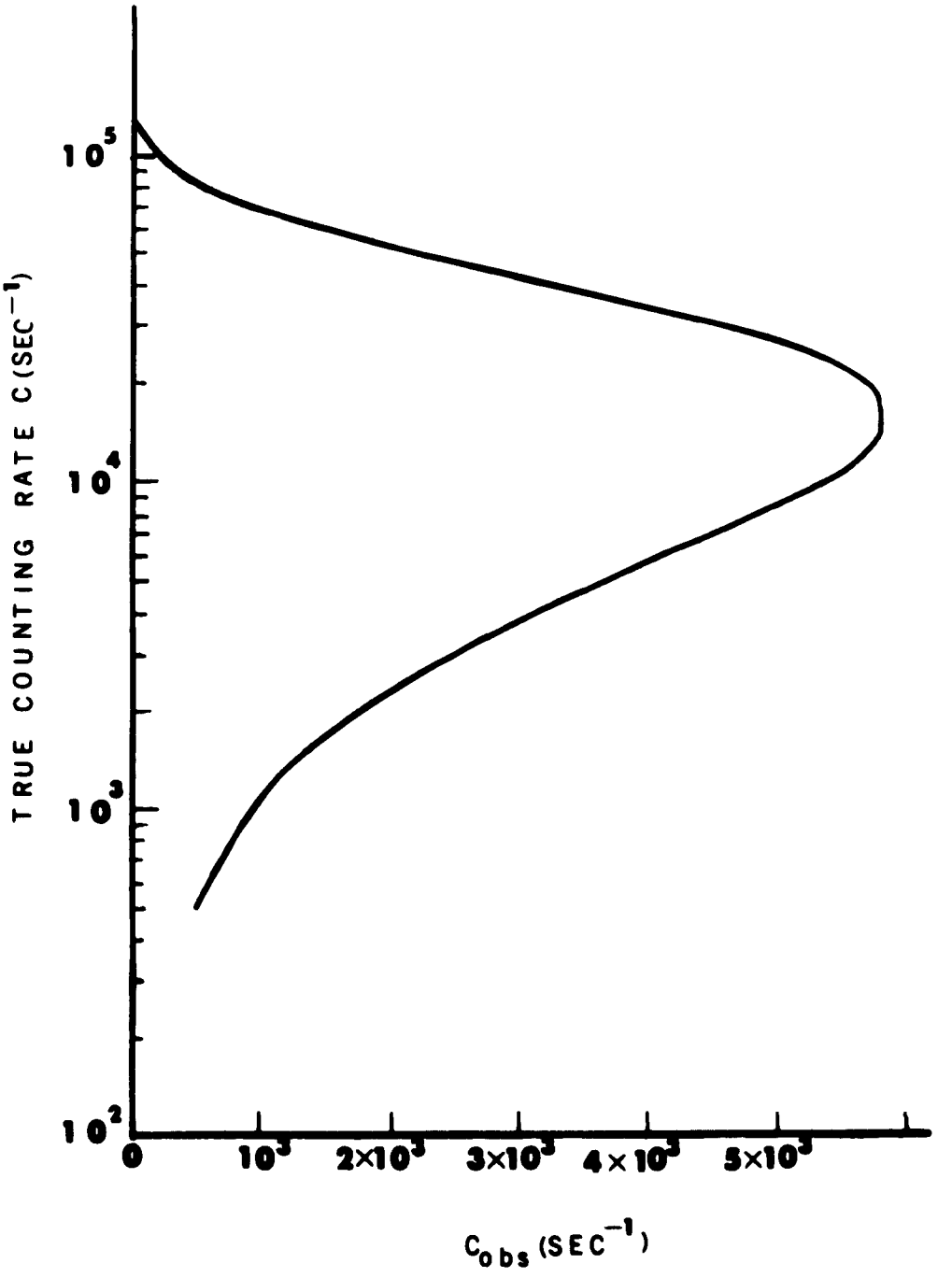
TRUE COUNTING RATE C(SEC^{-1})
10^5
10^4
10^3
10^2
0
10^3
2×10^3
3×10^3
4×10^3
5×10^3
C_{obs} (SEC^{-1})

Fig. 2.4. Antenna radiation patterns for transmitters of Explorer IV (Naumann, 1961).

Upper. Pattern of asymmetrical dipole for 108.00 mc-sec^{-1} low power (10 mw) transmitter.

Lower. Pattern of symmetrical dipole for 108.03 mc-sec^{-1} high power (25 mw) transmitter.

Both patterns are symmetrical about the long symmetry axis of the satellite.

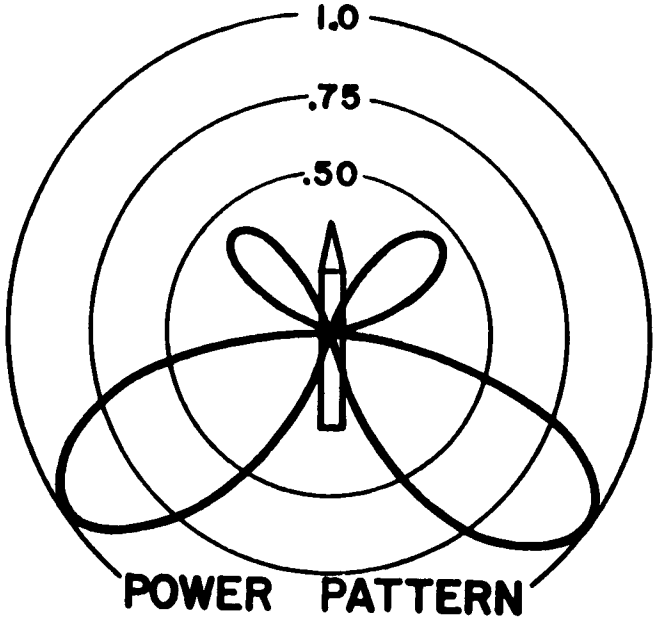

POWER PATTERN

108.00 mc

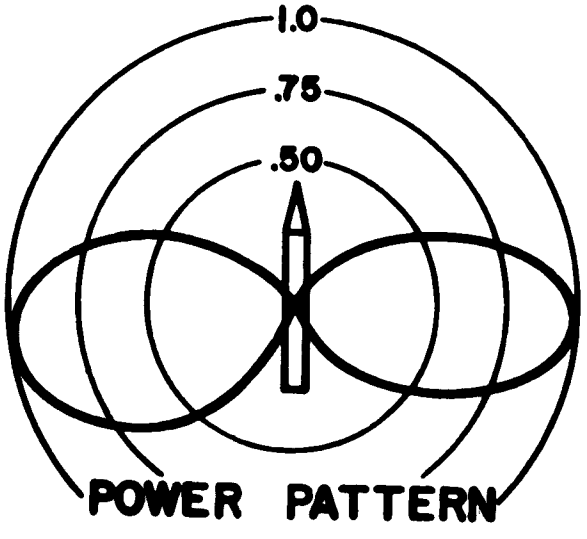

POWER PATTERN

108.03 mc

Fig. 2.5 Important geometry for describing satellite spin (or roll) and tumble. X', Y', Z' are fixed relative to satellite (see Fig. 2.2), with Z' as spin axis. XYZ are space fixed with Z (spin-tumble axis) taken as the axis of (constant) angular momentum $\hat{L}$. θ, ϕ, ψ are Euler angles.

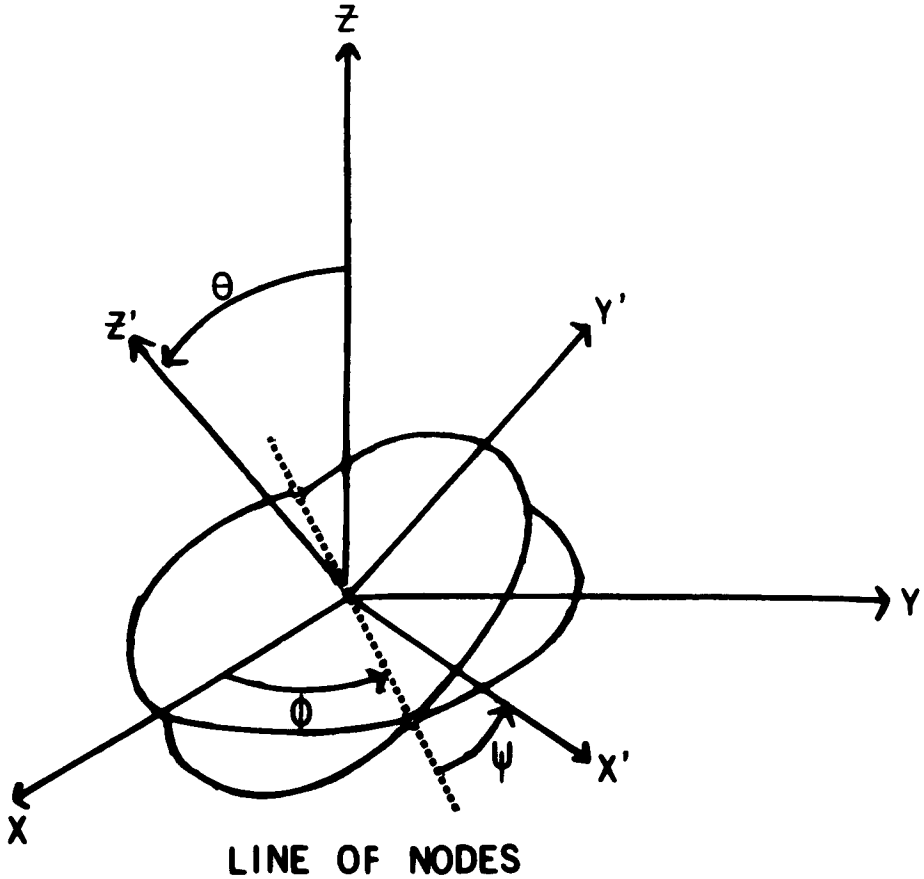
Z
Z'
θ
Y'
Y
X
X'
φ
ψ
LINE OF NODES

Fig. 2.6 Portion of "playback" record of the telemetry tape, received (August 27, 1958; 0416 UT) at Huntsville, Alabama for Pass 414 of Explorer IV Satellite.

The decreased amplitude of the recording for the middle portion of Channel 1 indicated saturation of the shielded G-M counter by the trapped ARGUS radiation.

The total number of telemetry channels recorded for records such as Fig. 2.6 are the following (3 channels only appear in Fig. 2.6)

Channel 1 - Detector D (reference, Fig. 2.1)

Channel 2 - Detector A (reference, Fig. 2.1)

Channel 3 - Detector C (reference, Fig. 2.1)

Channel 4 - Detector B (reference, Fig. 2.1)

Channel 5 - Detector A (reference, Fig. 2.1)

Channel 6 - r-f pattern, 108.03 mc-sec^{-1} transmitter

Channel 7 - r-f pattern, 108.00 mc-sec^{-1}

Channel 8 - time (WWV time signals).

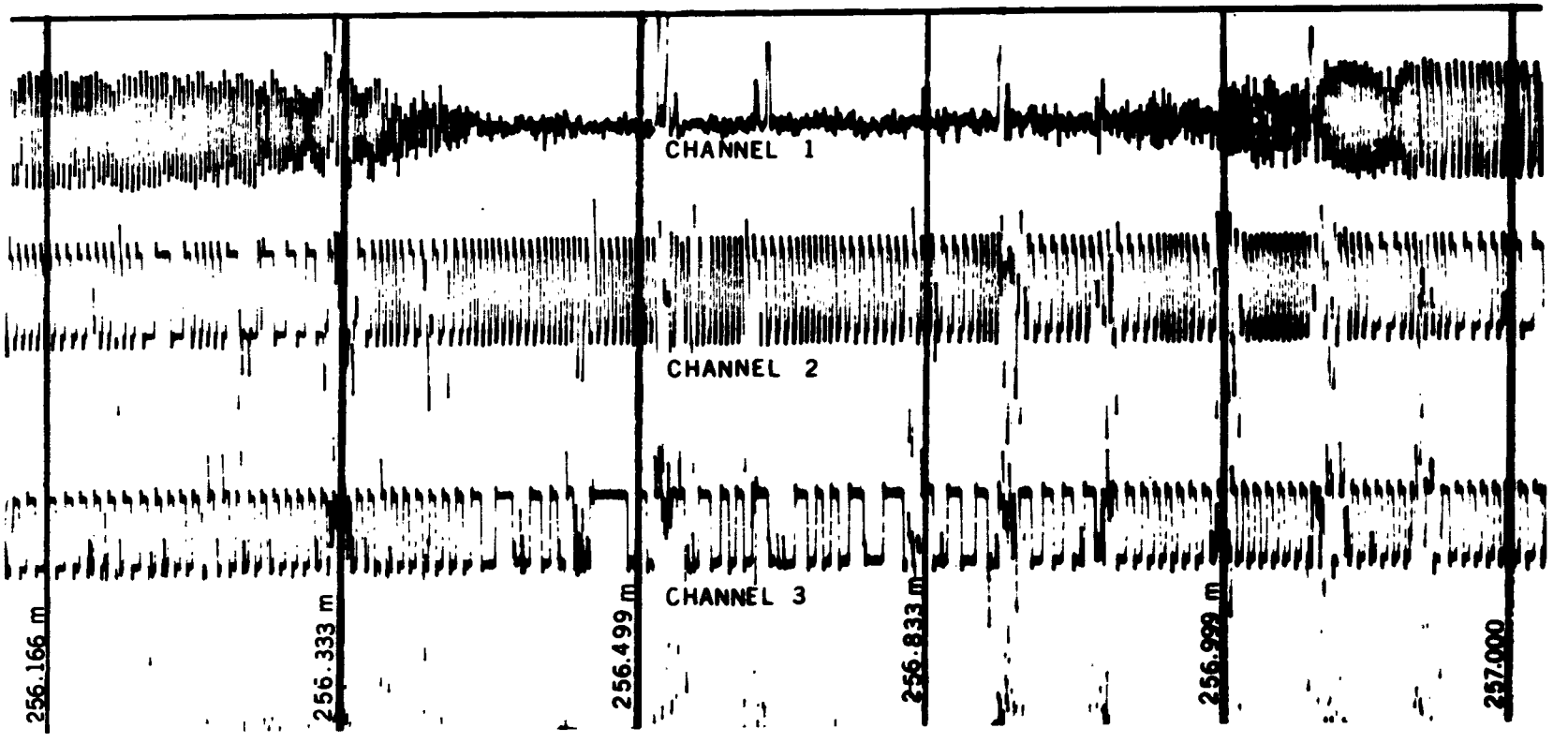
CHANNEL 1
CHANNEL 2
CHANNEL 3
256.166 m
256.333 m
256.499 m
256.833 m
256.999 m
257.000

Fig. 2.7 Sketch (smoothed) of r-f field strength modulations of the Huntsville ground station receiver AGC showing variations due to rotation of the satellite antennas (and of the satellite itself) relative to the line-of-sight from receiver to satellite. The patterns correspond to the alignment shown by Fig. 2.8 Upper; namely,

Trace 6 is for the 108.03 mc-sec^{-1} "high power" transmitter, radiation pattern shown by Fig. 2.4 Lower; Trace 7 for the 108.00 mc-sec^{-1} "low power" transmitter, radiation pattern Fig. 2.4 Upper.

N, T designate "nose" and "tail" ends of the satellite respectively.

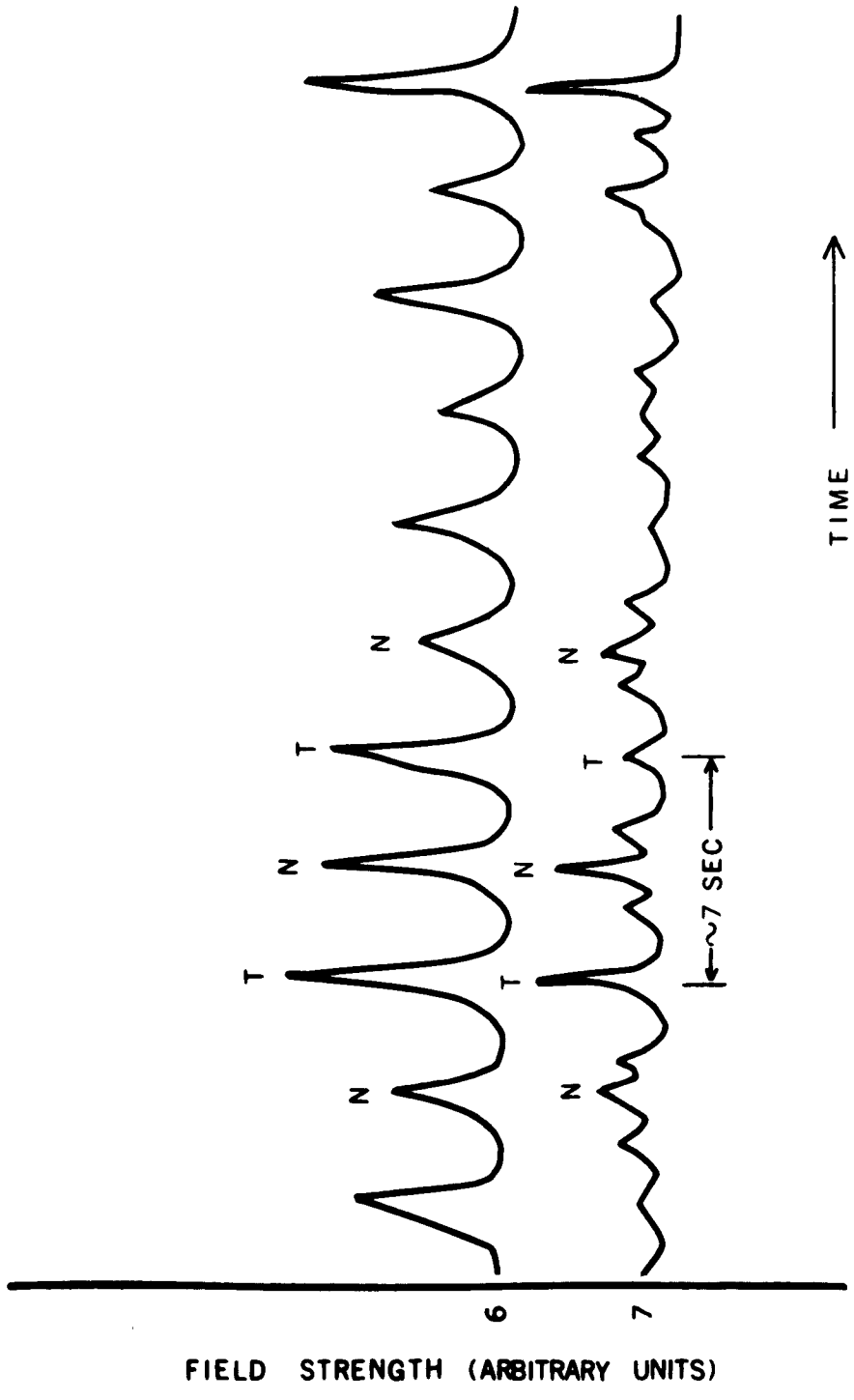
N
T
N
T
N
T
N
T
N
~7 SEC
TIME
6
7
FIELD STRENGTH (ARBITRARY UNITS)

Fig. 2.8 Sketch illustrating alignment of Explorer IV Satellite relative to ground station (Huntsville, Alabama) receiver antenna, RA.

Upper. $\hat{U} \perp \hat{L}$ Linearly polarized receiver antenna in the plane of tumble motion of satellite. $\hat{U}$, unit vector defining receiver station - to - satellite line-of-sight, in plane of tumble.

Lower. $\hat{U} \parallel \hat{L}$ Linearly polarized receiver antenna with $\hat{U}$ directed perpendicular to plane of tumble.

($\hat{A}$, satellite symmetry axis vector direction; reference Fig. 2.2).

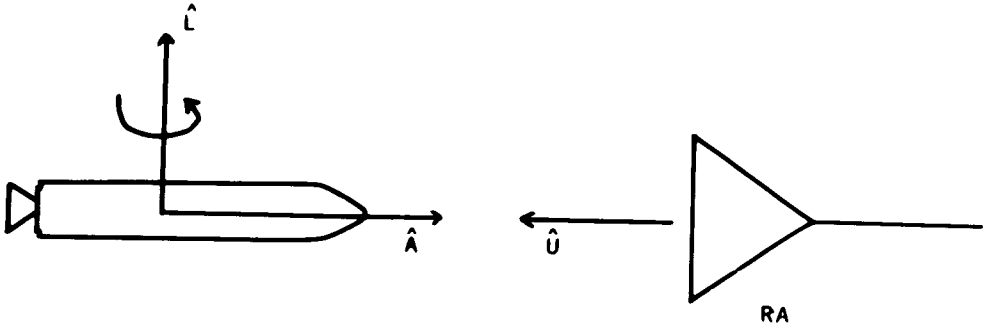
L̂
Â
Û
RA

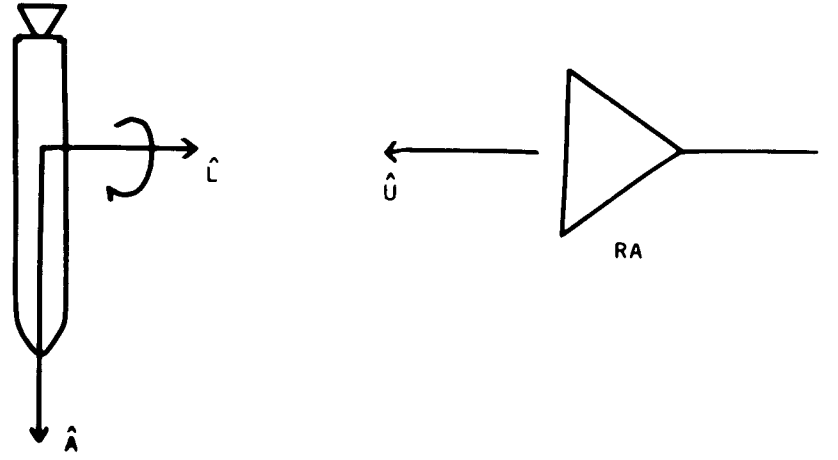
L̂
Â
Û
RA

Fig. 2.9 Lower, observed directional count-rate vs time (scintillation counter Detector A, Channel 2, Pass 414) for naturally injected trapped particle radiation compared with

Upper, variation of the arbitrarily chosen trigonometric function $\cos^4 \theta$ (θ, angle between scintillation counter axis and the plane perpendicular to the geomagnetic field direction) vs time; θ is calculated by Eq. (3.11) and such calculations are based on experimentally determined parameters.

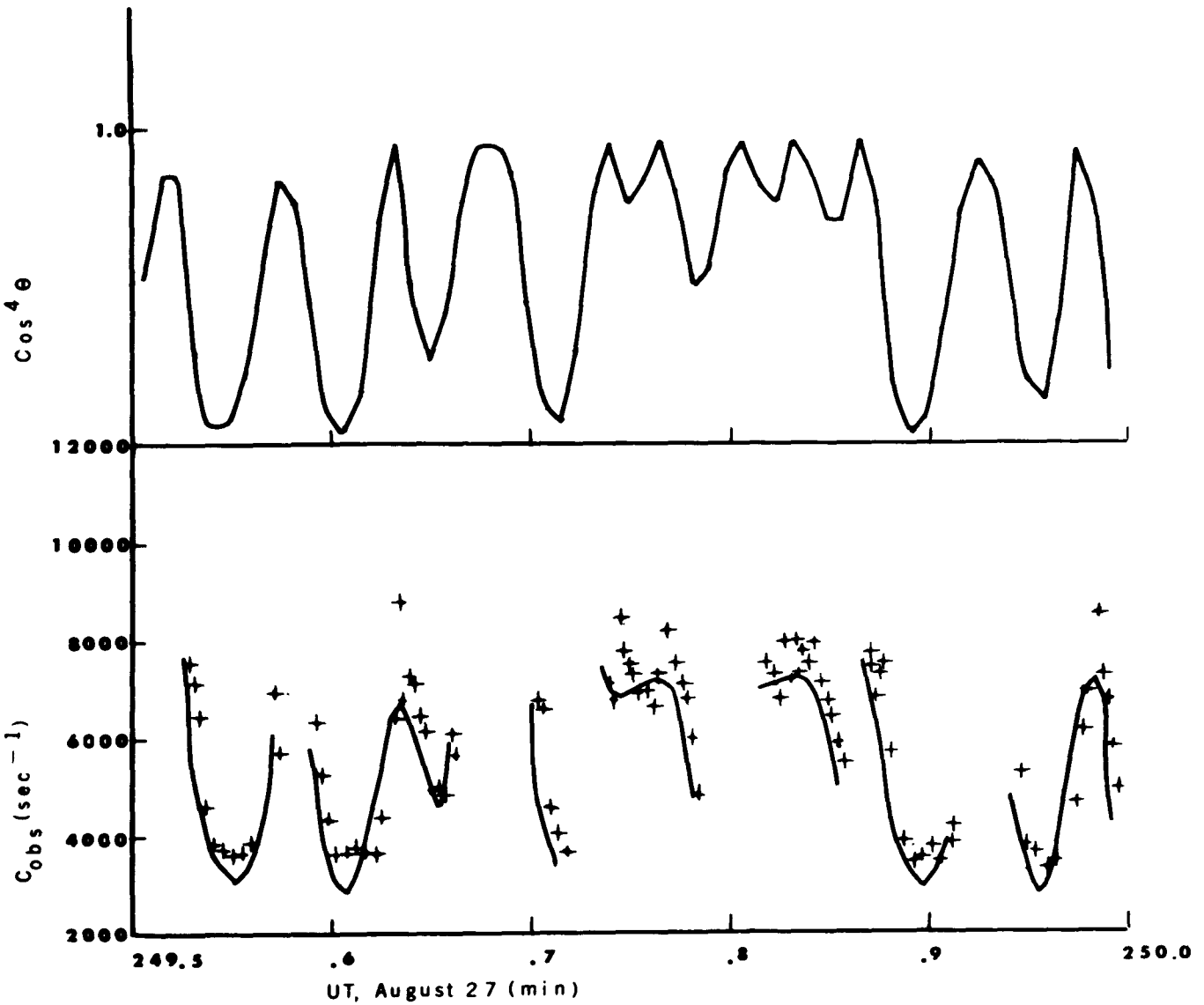
1.0
$\cos^4\theta$
12000
10000
8000
6000
4000
2000
C_{obs} (sec^{-1})
249.5
.6
.7
.8
.9
250.0
UT, August 27 (min)

Fig. 2.10 Lower, observed directional count-rate vs time (scintillation counter Detector A, Channel 2, Pass 414) for first half-minute of ARGUS shell penetration. Crosses, observed counting rates; solid lines are fits to observed points using a 4th-degree polynomial $A_0 + A_1 t + A_2 t^2 + A_3 t^3 + A_4 t^4$ (reference, Eq. (2.33)); where t is time in minutes since t_0, the time for the first data point for each polynomial.

The coefficients A_0, A_2, A_3, A_4 of the polynomials for the regions a, b, c, d, e, f, g, h, are listed tabularly as follows

Region	t_0 UT (min)	A_0	A_1	A_2	A_3	A_4
a	256.023	6.86245×10^3	-4.986728×10^4	1.0808205×10^7	-2.6862416×10^8	0
b	256.083	7.0753632×10^3	2.1318083×10^5	-1.68195×10^7	8.2345469×10^7	0
c	256.117	5.4850211×10^3	1.5342788×10^5	4.596898×10^5	-1.2041847×10^8	-3.3326533×10^8
d	256.177	2.1510846×10^3	2.4988362×10^5	4.6240195×10^7	-3.0009905×10^9	4.1530796×10^{10}
e	256.282	3.0680853×10^3	6.9111941×10^5	-2.0685974×10^7	0	0
f	256.318	5.0895242×10^3	-1.6534164×10^5	2.0491214×10^7	-4.7797797×10^8	3.1632694×10^9
g	256.381	7.2269874×10^3	$1.7P8405 \times 10^5$	1.1304334×10^7	-7.6906466×10^8	8.767632×10^9
h	256.420	6.3699230×10^3	3.4931835×10^5	-1.2803989×10^7	1.9409553×10^8	-1.0190348×10^9

The solid curve labeled B is the omnidirectional "true" counting rate (G-M counter, Detector C, Channel 3) reduced by a factor of 1/10 and is included to show the variation in the omnidirectional penetrating "background" radiation which occurring during the observation of the directional counting rates.

Upper, variation of $\cos^4 \theta$ as a function of time; for comparison with the observed counting rates vs time, Lower curve.

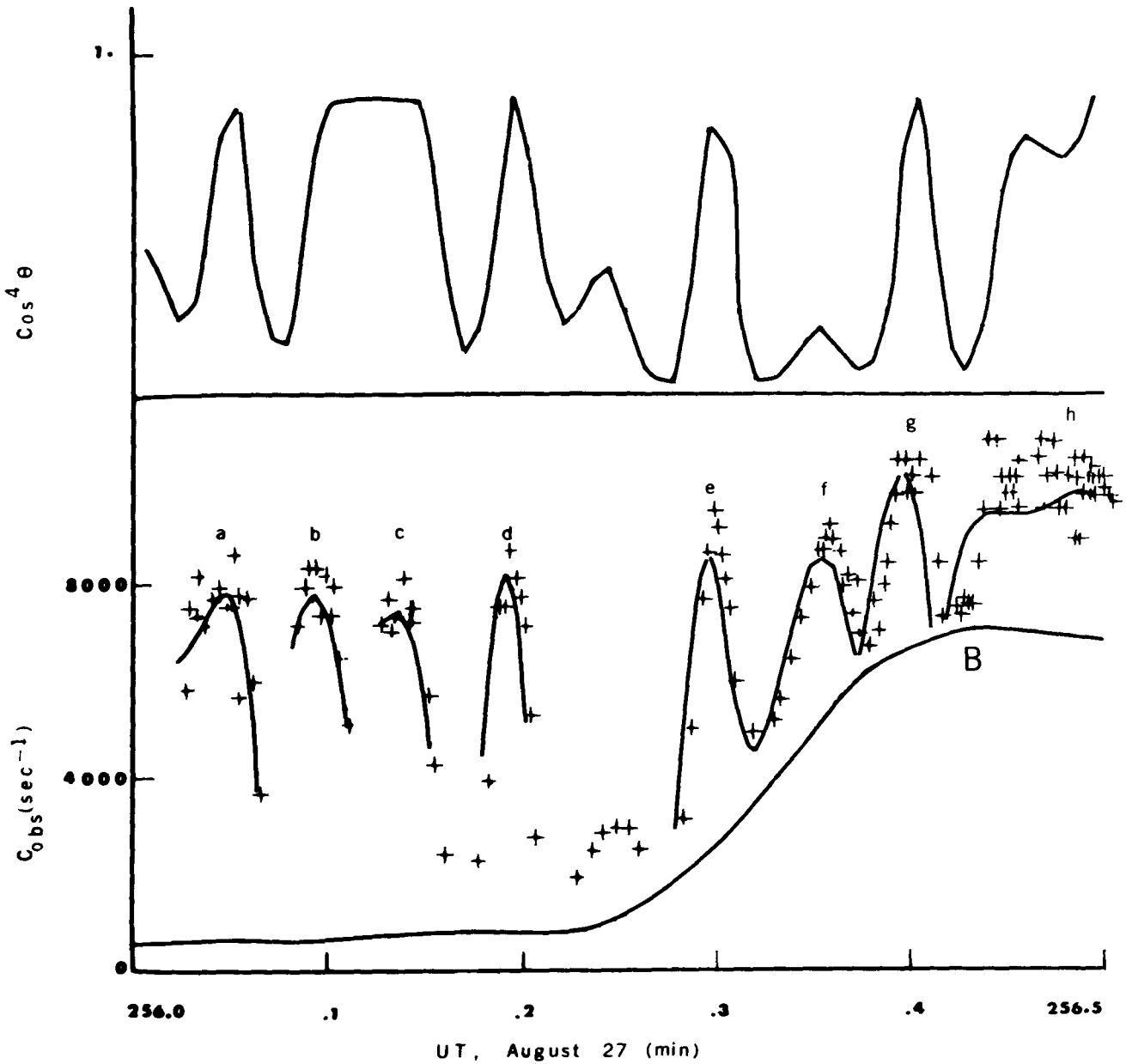
1.
$Cos^4\theta$
8000
4000
0
$C_{obs}(sec^{-1})$
a
b
c
d
e
f
g
h
B
256.0
.1
.2
.3
.4
256.5
UT, August 27 (min)

Fig. 2.11 Observed directional count-rate vs time (scintillation counter, Detector A, Channel 2, Pass 414) for the second half-minute of ARGUS shell penetration.

Figure 2.11 follows Fig. 2.10 immediately in time.

The descriptive details of Fig. 2.10 caption apply also to Fig. 2.11. The variations in the omnidirectional "penetrating" background radiation, solid curve B, are to be noted especially.

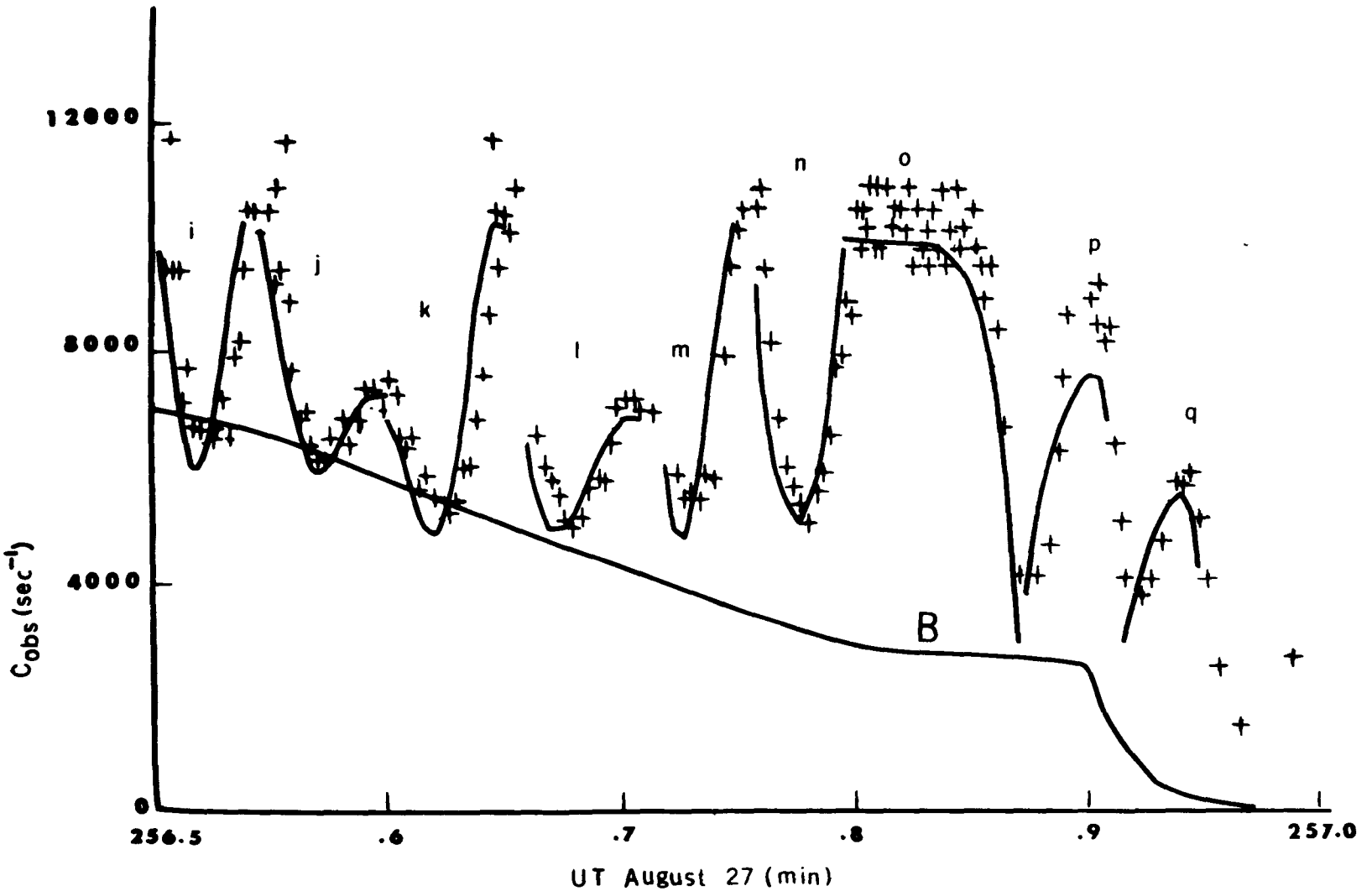
12000
8000
4000
0
C_{obs} (sec^{-1})
i
j
k
l
m
n
o
p
q
B
256.5
.6
.7
.8
.9
257.0
UT August 27 (min)

Chapter 3

Determination of Count-Rate C_{obs} as Function of the Angle θ Made by the Scintillation Counter with the Plane Perpendicular to the Geomagnetic Field

3.1 Satellite coordinate systems and geometry

The directional particle flux at any satellite position on a geomagnetic field line is related simply to the mirror point distribution (Weber et al, 1962). The first step in the calculation of the directional flux at a point in space is the measurement of the counting rate $C_{obs}(\theta)$ as a function of the angle θ between $\hat{P}$, a unit vector along the axis of the directional counter, and a plane perpendicular to the geomagnetic flux density $\hat{B}$ (unit vector). By Fig. 4.1,

$$\theta = \arcsin(\hat{P}\cdot\hat{B}), \text{ or } \theta = \arccos(\hat{P}\cdot\hat{B}_{\perp}),$$

where $\hat{B}_{\perp}$ is a unit vector perpendicular to $\hat{B}$; and, for pure tumble motion of the satellite

$$\theta = \arcsin\left[b_1 \sin(\dot{\psi}t+\delta) - b_2 \cos(\dot{\psi}t+\delta)\sin(\dot{\phi}t+\gamma) + b_3 \cos(\dot{\psi}t+\delta)\cos(\dot{\phi}t+\gamma)\right] \tag{3.11}$$

In Eq. (3.11), $\lambda = \pi/2 - \theta$, the tumble rate $\dot{\phi}$ and the spin or roll rate $\dot{\psi}$ are defined in Sec. 2.2, γ and δ are initial phase angles defined by Fig. 3.1, and b_1, b_2, b_3 are the components of

vector $\hat{B}$ on the X_s, Y_s, Z_s axes of the satellite inertial coordinate system, Fig. 3.1. From Eq. (3.11), θ can be calculated as a function of time and compared with the counting rate $C_{obs}(\theta)$ as has been discussed in Sec. 2.3, and shown by Figs. 2.9 and 2.10, provided $\dot{\phi}$, $\dot{\psi}$ are known and the phase angles γ and δ evaluated at some reference time t_0.

The geometry of the present analysis involves several coordinate systems. Equation (3.11) is calculated in a Satellite Inertial Coordinate System (Fig. 3.1), in which X_s has the direction of the angular momentum vector $\hat{L}$ (pure tumble axis also) considered constant during a some 20-minute interval of telemetry data acquisition; the Z_s direction is defined by

$$\hat{Z}_s = \hat{L} \times \hat{B}_o / S, \quad \text{where} \quad s = \left[1 - (\hat{L} \cdot \hat{B}_o)^2\right]^{1/2} \tag{3.12}$$

and $\hat{B}_0$ is a unit vector in the direction of the geomagnetic flux density at time t_0; and Y_s is determined by

$$\hat{Y}_s = \left[(\hat{L} \times \hat{B}_o \times \hat{L}\right] / S = (\hat{B}_o - \hat{L}K)/S, \quad \text{where} \quad K = \hat{L} \cdot \hat{B}_o \tag{3.13}$$

The Satellite Inertial Coordinate System of Fig. 3.1 is determined such that $\hat{B}$ is in the X_s-Y_s plane at $t=t_o$.

The axes X_s, Y_s, Z_s of the Satellite Inertial Coordinate System are to be unit vectors in the Vernal Equinox Coordinate System (Sec. 3.2) which is the basic reference coordinate system used in the present work. In the Vernal Equinox Coordinate System the X axis points to the Vernal

Equinox of 1951, the Y axis is in the earth's equatorial plane and the Z axis coincides with the axis of rotation of the earth at equinox. The components b_1, b_2, b_3 of Eq. (3.11) in the Satellite Inertial Coordinate System may be calculated at any time by

$$\begin{aligned} b_1 &= \hat{B}\cdot\hat{X}_s, \\ b_2 &= \hat{B}\cdot\hat{Y}_s, \\ b_3 &= \hat{B}\cdot\hat{Z}_s, \end{aligned} \tag{3.14}$$

it being noted that b_3 is zero at t_0.

Figure 3.1 indicates also that the tumble phase angle γ is defined by the direction of the satellite symmetry vector $\hat{A}$, (see also Fig. 2.2).

A third coordinate system, a Satellite Fixed Coordinate System (Fig. 3.1) is used to define δ, the spin or roll phase angle. In this system X_r is space-fixed in the direction of $\hat{L}$, Y_r is in the direction of vector $\hat{A}$ (which rotates in a plane perpendicular to $\hat{L}$ for the pure tumble, propeller-like motion). Angle δ is the angle between $\hat{P}$ and $\hat{Z}_r$ at time t_0, $\hat{L}$ is supplied by Naumann (1961) in the Vernal Equinox Coordinate System, $\hat{B}$ can be converted from the ephemeris system of coordinates to the VEC System (Sec. 3.2) and the Satellite Inertial Coordinate System is established at an initial reference t_0 time for each pass. The direction of the vector $\hat{A}$ is determined from the direction of $\hat{U}$ the line-of-sight vector (see Eq. 3.28) from the ground station to the satellite at the time t_0 of an r-f null by

$$\hat{A} = \pm \left[(\hat{L}\times\hat{U})\times\hat{L}\right] / \left|\hat{L}\times\hat{U}\right| \tag{3.15}$$

where the + sign is used for a tail null, minus sign for nose null.

The phase angle γ is then the arccosine of the dot product of $\hat{A}$ and $\hat{Y}_s$. With the various parameters of Eq. (3.11) determined θ may be calculated for any time following t_0 and compared with the count rate C_{obs} evaluated from the polynomial expressions as discussed in Sec. 2.3.

3.2 Conversion of 1958 Epsilon orbital data to the Vernal Equinox Coordinate System

The final reference coordinate system used in the present work is the Vernal Equinox Coordinate System (VE) defined and briefly discussed in the preceeding Sec. 3.1. Hence it is necessary to convert the geomagnetic field information of the 1958 Epsilon Orbital Data Series (Smithsonian Astrophysical Observatory, 1959) to the VE Coordinate System. Table 3.1 is a sample listing of 1958 Epsilon Orbital Data Series (op. cit., SAO, 1959) for Explorer IV Pass 414.

In order to compute the geomagnetic field components B_x, B_y and B_z in VE coordinates, Program 3.1 was used to convert the orbital information of Table 3.1 to the form shown in Table 3.2 where time is expressed in minutes UT, latitude is geocentric latitude, and B_x, B_y and B_z are the components of the $\hat{B}$ unit vector in the VE Coordinate System. Program 3.1 yields the converted data at 1 min time intervals and also computes 6th-order polynomial fits to these data (latitude, longitude, altitude, VE geomagnetic field components and satellite velocity components) so as to provide interpolation for any time within the 30 min interval fitted by the polynomials.

Some details of the conversion of the Explorer IV orbital data to Vernal Equinox coordinates follow. Calculation of the vector $\vec{R}$ (Fig. 3.2) from the center of the earth to the Huntsville ground station and the vector $\vec{r}$ from the center of the earth to the satellite in Vernal Equinox coordinates is included also.

The satellite orbital data (see Table 3.1) lists the geographic latitude and longitude of the intersection point of the international

ellipsoid and the radius vector $\vec{r}$ to the satellite. The height listed in Table 3.1 is the distance from this intersection point to the satellite. The geomagnetic flux density Table 3.1 is in rectangular topocentric coordinates relative to a spherical earth's surface with north N, east E and down D components calculated from the expansion of the earth's magnetic potential in spherical harmonics using Finch and Leaton coefficients of 1955.

The latitude most commonly listed on maps and in tables is called the geodetic latitude Δ (Fig. 3.2). This is the angle between the perpendicular to the tangent to the international ellipsoid (Fig. 3.2) and the plane of the equator. Table 3.1 lists the geographic latitude, defined by the angle between a local plumb bob and the plane of the equator, includes the effects of local gravitational anomalies and the local centrifugal force. The difference between geographic and geodetic latitude is small and called the station error. For all calculations in this report, geodetic and geographic latitude Δ are taken to be the same. For purposes of vector calculation and conversion to the VE Coordinate System it is necessary to use the geocentric latitude Δ' (Fig. 3.2), which is related to geodetic latitude by

$$\tan\Delta' = \tan\Delta\, b^2/a^2;\ b^2/a^2 = 1/1.0043, \tag{3.21}$$

and a and b are the equatorial and polar radii respectively of the international ellipsoid. The distance r of the satellite from the center of the earth in earth radii is equal to

$$r = b/(a^2\sin^2\Delta' + b^2\cos^2\Delta')^{1/2} + \text{height } 1958\epsilon / a\ , \tag{3.22}$$

where height $_{1958\epsilon}$ is the altitude listed in 1958 Epsilon Orbital Data Series (SAO, 1959). $\vec{R}$ the radius vector from the center of the earth to a station in VE coordinates in terms of the geodetic latitude Δ and the longitude Θ is given by

$$\begin{aligned} R_x &= (C+H)\cos\Delta \cos\Theta \\ R_y &= (C+H)\cos\Delta \sin\Theta \\ R_z &= (S+H) \sin\Delta, \end{aligned} \tag{3.23}$$

where longitude angle Θ is the hour angle to the Vernal Equinox given by

$$\Theta = \Theta_{gi} + 0.0043752695\,(t-t_i) + \Theta_E, \tag{3.24}$$

in which Θ_{gi} is the angle between the Greenwich meridian at t_i and t is in minutes after t_i, Θ_E is the east longitude of the station point; and

$$C = 1/(1-(2f-f^2)\sin\Delta)^{1/2}, \tag{3.25}$$

$H \equiv$ receiver antenna height above the international ellipsoid in earth radii units $f = (a-b)/a = 1/297.0$, and $c(1-f) \equiv S$.

The vector $\vec{r}$ from the center of the earth to the satellite is given in VE coordinates by

$$\begin{aligned} r_x &= h \cos\Delta'_s \cos\theta_s \\ r_y &= h \cos\Delta'_s \sin\theta_s \\ r_z &= h \sin\Delta'_s \end{aligned} \tag{3.26}$$

where Δ'_S is the geocentric latitude of the satellite, θ_S is the east longitude of the satellite from the Vernal Equinox. Thus, the satellite vector $\vec{r}$ is calculated using Δ' from the converted ephemeris while the station vector $\vec{R}$ is calculated using Δ in Eq. (3.23) which includes correction for the station height above the geoid and the difference between geodetic and geocentric latitude.

The geomagnetic field strength is converted by Program 3.1 to the VE system using the matrix equation

$$B_{VE} = \begin{pmatrix} B_Z \\ B_Y \\ -B_X \end{pmatrix} = \begin{pmatrix} 1 & 0 & 0 \\ 0 & \cos\theta_s & -\sin\theta_s \\ 0 & \sin\theta_s & \cos\theta_s \end{pmatrix} \begin{pmatrix} \cos\Delta' & 0 & -\sin\Delta' \\ 0 & 1 & 0 \\ \sin\Delta' & 0 & \cos\Delta' \end{pmatrix} \begin{pmatrix} b_N \\ b_E \\ b_D \end{pmatrix} \quad (3.27)$$

where b_N, b_E and b_D are the normalized (divided by B magnitude) of B_N, B_E and B_D. Once $\hat{B}$ is determined in Vernal Equinox coordinate, Eqs. (3.12), (3.13), (3.14) may be applied to calculate b_1, b_2 and b_3 for use in Eq. (3.11).

The ground station to satellite line-of-sight vector $\hat{U}$ from which the satellite symmetry vector $\hat{A}$ is calculated, Eq. (3.15), is given by

$$\vec{U} = \vec{r} - \vec{R} \quad (3.28)$$

It remains to evaluate the tumble and spin or roll rates $\dot{\phi}$ and $\dot{\psi}$ and the tumble and spin or roll phase angles γ and δ. The determination of these parameters is considered in Sec. 3.3.

3.3 Determination of tumble and spin or roll rates and phase angles; $\dot{\phi}, \dot{\psi}, \gamma, \delta$. The spin or roll period anomaly. Closure-search.

The tumble angular velocity, or rate, $\dot{\phi}$ may be determined as suggested by Naumann (1961) from the observations of the period of r-f nulls (Sec. 2.3) correcting for the orbital motion of the satellite as is indicated by Eq. (3.32) below. The direction of $\hat{A}$, Fig. 2.2 may be determined by

$$\hat{A}_i = \pm [(\hat{L} \times \hat{U}_i) \times \hat{L}] / |L \times \hat{U}_i| \tag{3.31}$$

where $\hat{A}_i$ and $\hat{U}_i$ are $\hat{A}$ and $\hat{U}$ respectively at the time of the ith null. The angle ϕ through which the satellite has tumbled between the first and the ith null is

$$\phi = \dot{\phi} t_i - \phi_0 = 2n\pi \pm \arccos(\hat{A}_1 \cdot \hat{A}_i) \tag{3.32}$$

where n is the number of tumble revolutions between the first and the ith null. The sign of the arccosine term depends on the sense of the tumble rate and the direction of orbital angular momentum vector. Equation (3.32) may be used to evaluate $\dot{\phi}$. However, for the present report the tumble rate as determined by Bock (1964) was used. Bock was able to determine the tumble rate to 5 decimal place accuracy by using an analog method. For Pass 414 Bock (op. cit.) evaluated the tumble

rate by the empirical expression

$$\dot{\phi} = 0.145037 - 0.56877 \times 10^{-6} t \text{ rev/sec } (14{,}868 < t < 15{,}420 \text{ sec UT}) \quad (3.33)$$

where t is measured in seconds after 0^h UT August 27, 1958.

The tumble phase angle γ (Sec. 3.1, Fig. 3.1) was determined by

$$\gamma = \arccos (\hat{A} \cdot \hat{Y}_s), \quad (3.34)$$

where $\hat{Y}_s$ is a unit vector in Vernal Equinox coordinates (Fig. 3.1). The time t_0 when $\hat{B}_0$ (magnetic flux density unit vector at t_0, Fig. 3.1) is in the X_s-Y_s plane, is then the initial time at which the Satellite Inertial Coordinate System was determined, and t in Eq. (3.11) is expressed in seconds after t_0.

Naumann's (1961) method of determining the spin or roll angular velocity, or rate, $\dot{\psi}$ was used for Pass 454 and attempted for Pass 414. Equation (3.11) indicates that for times when $\cos(\dot{\psi} t + \delta) = 0$, the count-rate of the directional scintillation counter will not show any variation due to tumble rotation and will be modulated only by the spin or roll of the satellite. By the determination of the period of such modulations Naumann was able to measure the time history of the roll period as shown by the circle points of Fig. (3.3). The interval August 24-29, 1957 exhibited the anomalous increase - decrease in roll period (the increase means a decreasing spin rate, the decrease which followed means an increasing spin rate.

In the present work, all attempts to use the roll rates determined by Naumann for Pass 414 (August 27, 1958) failed to yield any coherent picture of the variation of the Detector A count-rate with the angle θ

(between the counter axis and a plane perpendicular to the geomagnetic field direction). Although all values of δ (in 2° steps) were used to produce plots of θ as a function of time, using Eq. (3.11), for roll periods from 30-60 secs, no plot of θ vs time could be produced which matched the variations in counting rate for more than a minute.

A more recent determination of the roll period time history was achieved by Bock (1964) which resulted in the non-anomalous dashed line of Fig. (3.3). Use of the monotonically increasing roll periods (gradual slowing down of satellite spin) of Bock resulted in a coherent plot of the Detector A count-rate vs θ for Pass 414 (see also Sec. 3.4)

Further evidence for the correctness of Bock's non-anomalous roll periods was developed in the present work through Fourier series analyses of the Detector A count-rates for Passes 414, 427 and 453, as is detailed in Appendix 1, Power Spectrum. This analysis is concerned with beat-frequency periodicities appearing in the count-rate data. The squares used in Fig. 3.3 show the results of this kind of analysis for Passes 414, 427 and 453 and suggest strongly that the anomalous roll periods plotted by Naumann for the interval August 24-29, 1957 are due to measurement of beat frequencies rather than single modulation frequencies in the Detector A count-rates.

For Pass 414 Bock (1964) evaluated the true roll rate by the empirical expression

$$\dot{\psi} = 0.093858 - 0.3103975 \times 10^{-6} t + 0.2099974 \times 10^{-12} t^2 \text{ rev/sec} \quad (3.35)$$

where t is measured in seconds after the acquisition time for the pass or 14,868 sec UT.

The roll phase angle δ is the most difficult parameter to determine in Eq. (3.11). Naumann's (1961) method does not work when roll and tumble rates are nearly the same. Hence, δ was determined in the present work (Program 3.3) by a brute-force variational procedure termed "closure-search" as follows.

If all the variables of Eq. (3.11) except δ are determined θ can be calculated for any time of interest by performing a variation on δ. The procedure adopted was to determine the time of an r-f null shortly after ground station acquisition of the satellite. This time was used as reference time t_0 from which t in Eq. (3.11) was measured. The satellite inertial axes (Sec. 3.1, Fig. 3.1) were calculated using Eqs. (3.12) and (3.13) and the value of B at t_0. $\hat{A}$ was computed using Eq. (3.15) and phase angle γ as explained in Sec. 3.1. Polynomials (3rd or less order) which fitted the counting rate for the short (.06 min, approximately) intervals between signal fade-outs were used to evaluate the Detector A count-rates for all desired times. θ was then calculated for each of these count-rate determinations for all values of δ in the range 0 - 360°. For each delta, C_{obs} as a function of λ, $\lambda = \pi/2 - \theta$, was considered by the computer throughout the time interval of the polynomial in question. If the polynomial fitted data yielding the same count rate at two different times (for example, polynomial e Fig. 2.10), ten time-pairs of equal count-rates were determined from the polynomial and pairs of λ corresponding to the time pairs calculated using Eq. (3.11). If more than 70 percent of the λ pairs were within 5° of being equal a graph of the function C_{obs} vs λ was plotted. If the polynomial fitted

data in which most of the counting rate values were unique (for example, polynomial c Fig. 2.10), the slope and C_{obs} intercept of a straight line fitted to C_{obs} vs λ was listed for each δ . This procedure was carried out for 98 polynomials for Pass 414 and one degree steps (0-360°) for δ , including both the natural and the ARGUS trapping regions.

The resulting plots and listing of slopes then were investigated to determine a single value of δ which satisfied the criterion that the graph of C_{obs} vs λ would be single valued for each of the 98 sections of the Detector A count-rate intervals considered. If any of the parameters of Eq. (3.11) were slightly incorrect the plots of C_{obs} vs λ were found to be multivalued so that C_{obs} vs λ points formed an open loop. The procedure as outlined therefore was termed a "closure-search" and the values of tumble rate, roll rate $\dot{\phi}, \dot{\psi}$ and b1, b2, b3, were considered to be correct when a single value of δ satisfied the closure criterion for all polynomials used.

For Pass 414 an r-f null was observed at 248.941 UT August 27, 1958. γ was calculated to be 351.6 and δ was evaluated by closure-search as 50°. This value of δ satisfied the closure criteria for all 98 sections of the Detector A count-rate data except those in which the background counting rate varied rapidly during a time period of about one-half the tumble period.

An additional check on the determination of parameters is demonstrated by Figs. 2.9 and 2.10 wnerein $\cos^4\theta$ vs time (Upper) is compared with C_{obs} vs time (Lower) for the scintillation counter. The $\cos^4\theta$, suggested by Bock, is an empirical analytic fit to the $C_{obs}(\theta)$ vs θ curves

of Sec. 2.3 of the present report. It is observed in Figs. 2.9, 2.10 that $\cos^4\theta$ vs time curves represent well the C_{obs} vs time curves for both the natural and the ARGUS trapping regions except for the time interval during which there is sudden increase in omnidirectional background radiation (curve B) in the ARGUS region. This background radiation effect is discussed in Chap. 5.

3.4 Observed directional count-rate for ARGUS trapping, C_{obs} vs θ.

Results and conclusions.

As noted and explained in preceding sections of the present chapter, the count-rate of the directional detector (Detector A, Channel 2) was determined as a function of the angle θ between the scintillation counter axis and the plane perpendicular to the geomagnetic field for both the natural and the ARGUS trapped radiation.

Figures 2.9 (natural trapping, Pass 414) and 2.10, 2.11 (ARGUS trapping, Pass 414) illustrate the results of the analyses of directional count-rate (C_{obs}) and angle θ (in form of $\cos^4\theta$) vs real time (UT).

Figures 3.4, 3.5 and 3.6 illustrate the results of the determination (Sec. 3.3, closure-search procedure) of observed directional count-rate C_{obs} vs θ for several of the modulations designated a, b, c .... q in Figs. 2.10 and 2.11.

Although the "disc-like" character of the trapped radiation is generally evidenced by the maxima of C_{obs} at $\theta = 0°$ and decreased values at larger angles, the plots of Figs. 3.4, 3.5 and 3.6 show considerable variation in the angular distributions of directional count-rates (C_{obs} vs θ) for ARGUS trapping. These variations are considered to be due mainly to 1. scatter in the data itself, and 2, effects of the omnidirectional penetrating radiation (curves B, Figs. 2.10 and 2.11) upon the counting-rate of directional Detector A.

Item 2 just noted is considered to be one of the special conclusions of the present work. However, since it has been possible in the time available to analyse but a small percent of the available Explorer IV directional count-rate data by the closure-search procedure (Sec. 3.3), any conclusions stated here must be considered as tentative. Keeping this reservation in mind, there is suggestive and fairly convincing evidence nevertheless that the shape of the angular distribution of count-rate (C_{obs} vs θ, Figs. 3.4, 3.5 and 3.6) is affected by the omni-directional penetrating radiation (curves B, Figs. 2.10 and 2.11); as follows:

(1) Plot b, c, d (Fig. 3.4, upper left) is a combined plot of modulations b, c, d of Fig. 2.10, Lower. Thus all 3 modulations can be represented in a single plot, suggesting that the low intensity and constant background penetrating radiation (curve B; Fig. 2.10, Lower) is not a disturbing factor in the C_{obs} vs θ analysis.

(2) Plot f (Fig. 3.4, upper right) is an example of the apparent effect of the rapidly increasing background (curve B, Fig. 2.10 Lower), it being suggested that the set of points indicating abnormally large count-rates (near $\theta = 50°$-$60°$) include some background radiation. It appears that the C_{obs} vs θ count-rate data should be corrected for changing background as the satellite moves through the ARGUS belt for regions such as f (Figs. 3.4, 2.10).

(3) Plot g (Fig. 3.4, lower left) exhibits a broader angular distribution of the directional count-rate. At the same time curve B, Fig. 2.10 Lower, involves an increasing background penetrating radiation which may have contributed to the directional count-rate intensity level to cause the broadening of curve g. It is difficult to make a quantitative esti-

mate of the precise contribution of the omnidirectional G-M count-rates to the directional scintillation detector count-rates since the calibrations of the detectors involved did not include intercalibration of the G-M and scintillation counters for the same penetrating radiations. Also, any penetrating component of the directional radiation might be more readily detected by the scintillation counter at larger θ values since there is generally more shielding in directions away from the counter axis.

(4) Plot h (Fig. 3.4, lower right) has broader angular distribution than plot g, the penetrating background radiation curve B, Fig. 2.10, Lower, is at the same time somewhat more intense than for plot g and so the effect of the penetrating background radiation is quite similar to that suggested for plot g. Further the count-rate of the directional detector is approaching saturation, the rate being in excess of 10^4 per sec, a situation which would produce relative broadening of the angular distribution by the flattening process.

(5) Plot j (Fig. 3.5, upper left) corresponds to a decreasing background radiation (curve B, Fig. 2.11) suggesting that the narrowness of the angular distribution of plot j is due to decreasing directional count-rate at larger θ values.

(6) Plots k, l, m, n, o (Fig. 3.5 and 3.6) show variation in the angular distribution of the directional count-rates similar to the plots of Figs. 3.4 and 3.5 already discussed and these variations suggest again the effect of penetrating background radiation (curve B, Fig. 2.11). Plots m and o suggest that a burst of penetrating radiation was encountered toward the end of the time periods for the two plots since the two groups

of points showing maximum count-rate for ranges of θ of about 0°-30° or 40° occur last in the time sequence. This penetrating radiation effect may be present for the entire sequence of plots 1 through p. The effects are not always clear and unmistakable but they do appear to be present.

(7) Finally plots p and q (Fig. 3.6 lower) seem to show the effect of the sudden decrease in curve B, Fig. 2.11, occurring at about the same time as the sharp decrease in count-rate for plot p (near θ = 5°) and the continued less-sharp decrease for plot q. These sudden decreases in count-rates are similar effects to the corresponding increase shown by plot f.

Table 3.1. Portion of 1958 Epsilon (Explorer IV, Pass 414) Orbital Data Series (Smithsonian "Astrophysical Observatory, 1959)

Time, UT (hr-min)	East Latitude (°)	Geographic Latitude (°)	Height (km)	Geomagnetic Flux Density Components (Gauss)			Satellite Velocity Components (km/hr)		
				B_N	B_E	B_D	V_N	V_E	V_D
04 05	268.34	-06.85	1953.4	.136	0.019	0.019	014996.1	16001.8	01745.6
04 06	269.84	-04.76	1923.1	.138	0.018	0.031	015089.3	16035.6	01874.0
04 07	271.34	-02.64	1890.7	.140	0.016	0.043	015173.0	16089.5	01999.1
04 08	272.85	-00.51	1856.3	.141	0.015	0.056	015246.8	16163.6	02120.7
04 09	274.38	001.64	1820.0	.142	0.013	0.069	015310.4	16258.5	02238.4
04 10	275.92	003.81	1781.8	.144	0.011	0.082	015363.2	16374.4	02351.8
04 11	277.49	005.99	1741.9	.144	0.009	0.096	015404.1	16512.2	02460.6
04 12	279.09	008.20	1700.2	.145	0.007	0.110	015432.1	16672.5	02564.4
04 13	280.73	010.41	1656.9	.145	0.005	0.125	015445.7	16856.1	02662.8
04 14	282.43	012.64	1612.0	.146	0.002	0.139	015443.1	17064.0	02755.5
04 15	284.17	014.88	1565.8	.145	-.001	0.154	015422.0	17297.2	02842.0
04 16	285.99	017.13	1518.2	.145	-.004	0.170	015379.7	17557.1	02921.8
04 17	287.88	019.38	1469.4	.144	-.008	0.185	015313.2	17844.8	02994.4
04 18	289.86	021.64	1419.4	.142	-.012	0.200	015218.3	18162.0	03059.5
04 19	291.94	023.89	1368.6	.140	-.016	0.215	015090.7	18510.3	03116.6
04 20	294.13	026.13	1316.9	.138	-.020	0.229	014924.8	18891.0	03165.0
04 21	296.45	028.36	1264.4	.136	-.024	0.243	014714.1	19306.2	03204.4
04 22	298.92	030.57	1211.5	.134	-.029	0.256	014450.9	19757.1	03234.2
04 23	301.55	032.75	1158.1	.131	-.033	0.268	014126.4	20245.0	03253.9
04 24	304.38	034.89	1104.5	.129	-.038	0.279	013730.3	20770.5	03262.9
04 25	307.40	036.98	1050.9	.127	-.042	0.289	013250.5	21333.7	03260.8
04 26	310.67	039.00	0997.4	.126	-.046	0.298	012673.6	21933.0	03247.1
04 27	314.18	040.93	0944.2	.125	-.049	0.305	011985.2	22564.5	03221.4
04 28	317.97	042.76	0891.5	.125	-.052	0.312	011169.4	23222.7	03183.1
04 29	322.07	044.46	0839.5	.125	-.053	0.317	010210.9	23897.3	03131.9
04 30	326.47	046.01	0788.3	.127	-.054	0.321	009095.9	24574.4	03067.4
04 31	331.20	047.37	0738.4	.130	-.053	0.325	007814.7	25234.3	02989.4
04 32	336.24	048.52	0689.7	.133	-.050	0.328	006362.7	25853.8	02897.7
04 33	341.58	049.43	0642.6	.138	-.046	0.330	004745.8	26404.7	02792.1
04 34	347.17	050.07	0597.3	.143	-.040	0.333	002982.2	26858.0	02672.7

Table 3.2. Orbital data of Table 3.1. with magnetic flux density components in Vernal Equinox Coordinate System

Time, UT (min)	East Longitude (°)	Geocentric Latitude (°)	Distance Satellite to Geocenter (Earth radii)	Components of Magnetic Flux Density Unit Vector in VE Coordinate System			Satellite Velocity Components (km/hr)		
				B_X	B_Y	B_Z	V_N	V_E	V_D
245.	268.34	-6.80	1.3062	.101	.093	.990	14996.1	16001.8	1745.6
246.	269.84	-4.72	1.3014	.020	.185	.982	15089.3	16035.6	1874.0
247.	271.34	-2.62	1.2964	-.067	.262	.962	15173.0	16089.5	1999.1
248.	272.85	-.50	1.2910	-.153	.339	.928	15246.8	16163.6	2120.7
249.	274.38	1.62	1.2853	-.244	.399	.883	15310.4	16258.5	2238.4
250.	275.92	3.78	1.2793	-.329	.445	.832	15363.2	16374.4	2351.8
251.	277.49	5.95	1.2730	-.414	.486	.769	15404.1	16512.2	2460.6
252.	279.09	8.14	1.2664	-.493	.512	.702	15432.1	16672.5	2564.4
253.	280.73	10.34	1.2596	-.568	.531	.627	15445.7	16856.1	2662.8
254.	282.43	12.55	1.2525	-.637	.532	.556	15443.1	17064.0	2755.5
255.	284.17	14.78	1.2452	-.703	.527	.477	15422.0	17297.2	2842.0
256.	285.99	17.02	1.2377	-.760	.512	.397	15379.7	17557.1	2921.8
257.	287.88	19.25	1.2300	-.813	.486	.319	15313.2	17844.8	2994.4
258.	289.86	21.50	1.2220	-.858	.453	.239	15218.3	18162.0	3059.5
259.	291.94	23.74	1.2140	-.895	.413	.161	15090.7	18510.3	3116.6
260.	294.13	25.97	1.2058	-.925	.367	.088	14924.8	18891.0	3165.0
261.	296.45	28.19	1.1974	-.948	.316	.018	14714.1	19306.2	3204.4
262.	298.92	30.40	1.1890	-.965	.257	-.048	14450.9	19757.1	3234.2
263.	301.55	32.57	1.1805	-.973	.197	-.112	14126.4	20245.0	3253.9
264.	304.38	34.70	1.1720	-.976	.129	-.170	13730.3	20770.5	3262.9
265.	307.40	36.79	1.1635	-.972	.062	-.224	13250.5	21333.7	3260.8
266.	310.67	38.81	1.1550	-.962	-.008	-.271	12673.6	21933.0	3247.1
267.	314.18	40.73	1.1465	-.946	-.078	-.313	11985.2	22564.5	3221.4
268.	317.97	42.56	1.1382	-.924	-.150	-.349	11169.4	23222.7	3183.1
269.	322.07	44.26	1.1299	-.897	-.220	-.382	10210.9	23897.3	3131.9
270.	326.47	45.81	1.1218	-.866	-.291	-.405	9095.9	24574.4	3067.4
271.	331.20	47.17	1.1139	-.831	-.359	-.423	7814.7	25234.3	2989.4
272.	336.24	48.32	1.1062	-.792	-.423	-.438	6362.7	25853.8	2897.7
273.	341.58	49.23	1.0988	-.752	-.487	-.443	4745.8	26404.7	2792.1
274.	347.17	49.87	1.0916	-.709	-.546	-.445	2982.2	26858.0	2672.7

Fig. 3.1 Geometries employed in determination of count-rates of Explorer IV directional scintillation counter in terms of orientation of the satellite relative to geomagnetic field direction. All symbols are explained in the text.

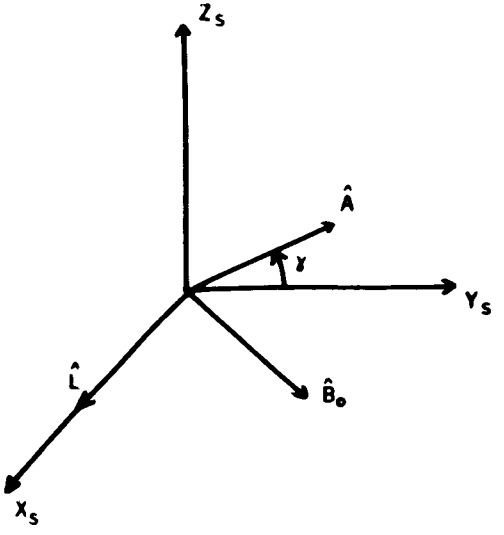

SATELLITE INERTIAL COORDINATE SYSTEM

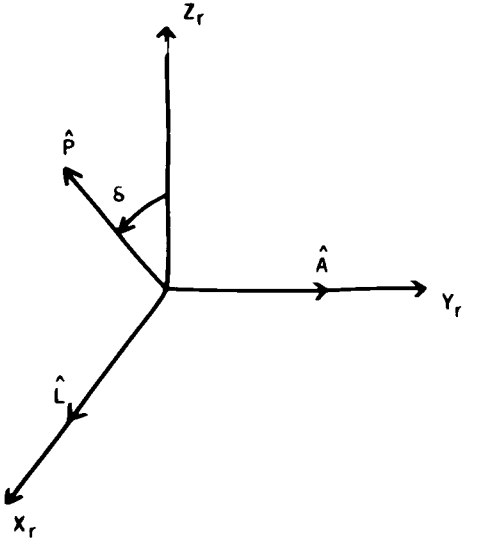

SATELLITE FIXED COORDINATE SYSTEM

Fig. 3.2 Sketch showing various geometric and vector quantities and their interrelations. Δ, geodetic latitude; Δ', geocentric latitude.

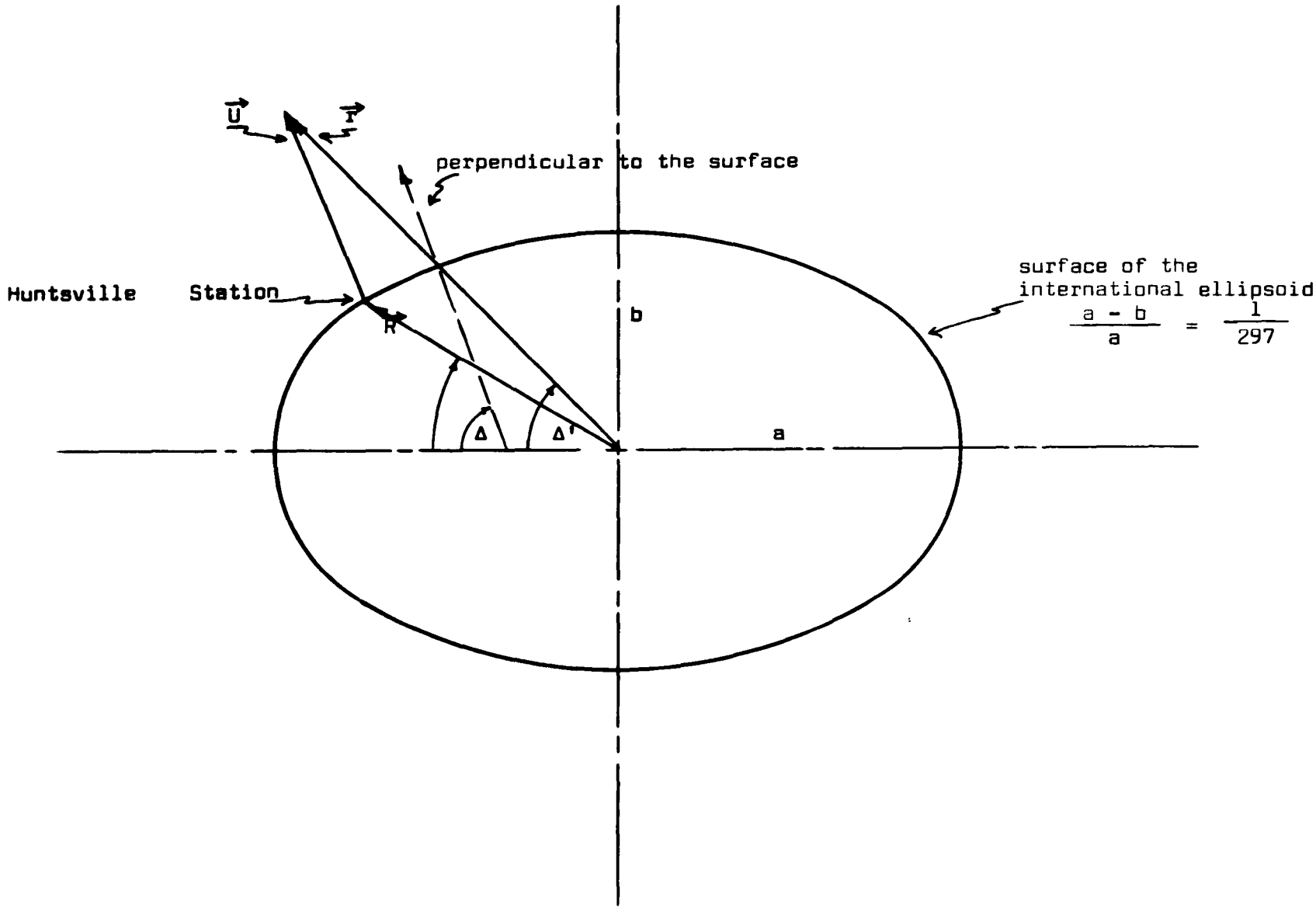
$\vec{U}$
$\vec{r}$
perpendicular to the surface
Huntsville Station
R
b
surface of the
international ellipsoid
$\frac{a-b}{a} = \frac{1}{297}$
Δ
Δ'
a

Fig. 3.3 Roll or spin period time history of Explorer IV Satellite showing anomalous increase-decrease (circle points) between August 24 and 29, 1958 - calculated by Naumann (1961).

Dashed-line (X points) represent a non-anomalous roll period history as determined by Bock (1964) by an analog computer method.

Squares locate beat-frequency periods measured in the Detector A count-rate data by the authors of the present report and suggest that Naumann's anomalous roll periods are due to measurement of beat frequency periods rather than single (correct) roll periods.

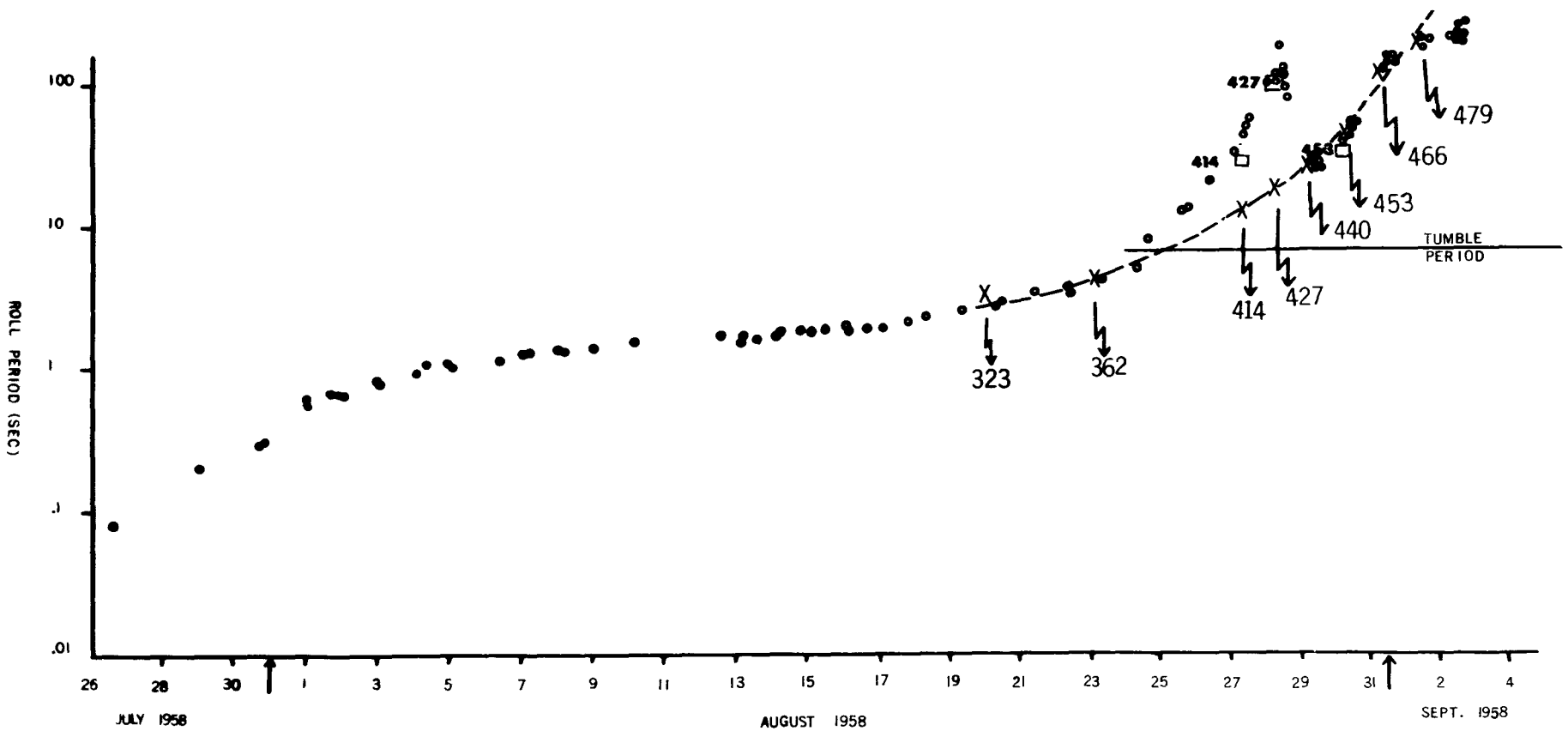
ROLL PERIOD (SEC)
100
10
1
.1
.01
26
28
30
1
3
5
7
9
11
13
15
17
19
21
23
25
27
29
31
2
4
JULY 1958
AUGUST 1958
SEPT. 1958
323
362
414
427
440
453
466
479
TUMBLE PERIOD

Figs. 3.4, 3.5, 3.6 Observed directional count-rate C_{obs} vs θ during penetration of ARGUS (Event I) shell, Pass 414.

The lower case letters in parentheses in the upper left hand corners of the individual plots correspond to the same lettered count-rate modulations shown by Figs. 2.10 and 2.11. The twelve separate plots were obtained by individual closure-search procedures as explained in Sec. 3.3.

Abscissa values for θ were calculated by Eq. (3.11) using observed times t and values of the other parameters as discussed in the text. The same time references (248.941 UT), and phase angles (γ = 351.6°, δ = 50°) were employed for all the plots of Figs. 3.4, 3.5, 3.6.

The various steps in the reduction and analysis of data followed to obtain the data for C_{obs} vs θ (Figs. 3.4, 3.5, 3.6) are

(1) C_{obs} vs time is obtained as in Figs. 2.10, 2.11;

(2) Polynomial-fitting to the plots of (1) is accomplished;

(3) γ and δ are evaluated from r-f null data and the closure-search procedure respectively;

(4) b_1, b_2 and b_3 are calculated from B_x, B_y, B_z in the Vernal Equinox Coordinate System and Naumann's estimate of angular momentum $\hat{L}$ direction.

(5) The magnitude of $\hat{L}$, $\dot{\phi}$ and $\dot{\psi}$ are obtained using J. Bock's decay coefficients;

(6) θ is calculated by Eq. (3.11).

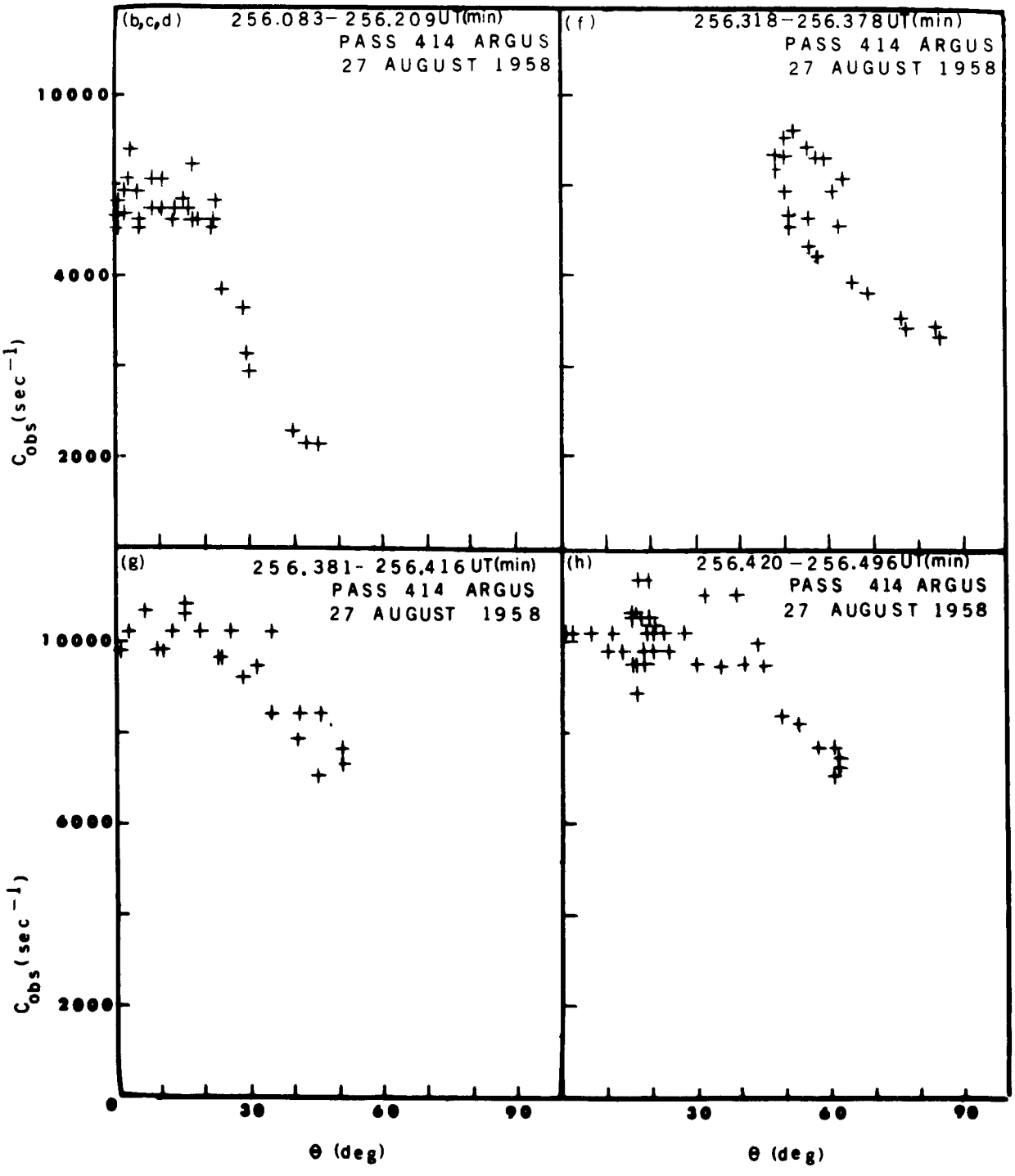
(b,c,d) 256.083-256.209UT(min)
PASS 414 ARGUS
27 AUGUST 1958
(f) 256.318-256.378UT(min)
PASS 414 ARGUS
27 AUGUST 1958
(g) 256.381-256.416UT(min)
PASS 414 ARGUS
27 AUGUST 1958
(h) 256.420-256.496UT(min)
PASS 414 ARGUS
27 AUGUST 1958
10000
4000
2000
6000
0
30
60
90
$C_{obs}(sec^{-1})$
θ (deg)

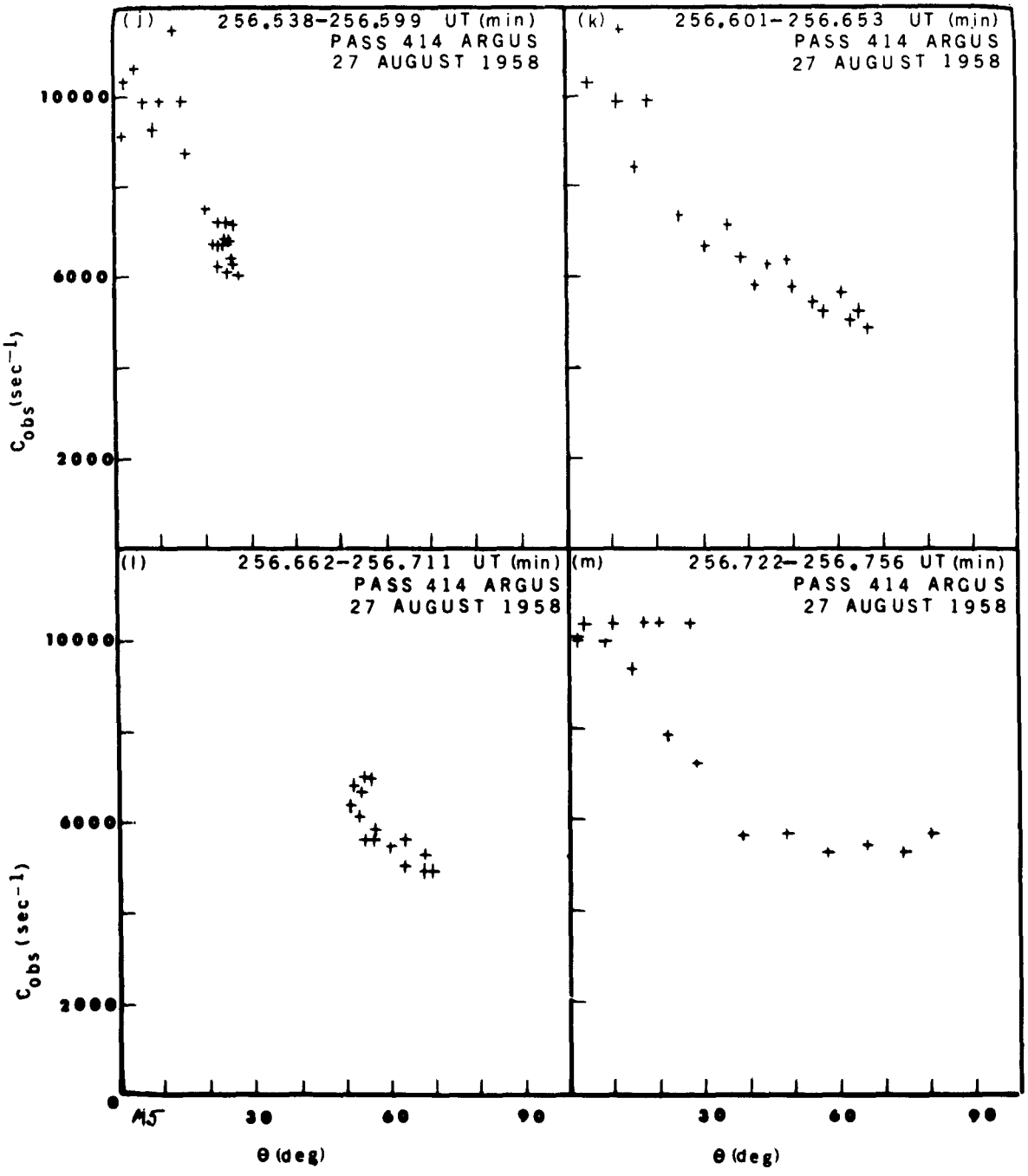
(j) 256.538–256.599 UT (min)
PASS 414 ARGUS
27 AUGUST 1958
(k) 256.601–256.653 UT (min)
PASS 414 ARGUS
27 AUGUST 1958
(l) 256.662–256.711 UT (min)
PASS 414 ARGUS
27 AUGUST 1958
(m) 256.722–256.756 UT (min)
PASS 414 ARGUS
27 AUGUST 1958
10000
6000
2000
0
C_{obs} (sec^{-1})
15
30
60
90
θ (deg)

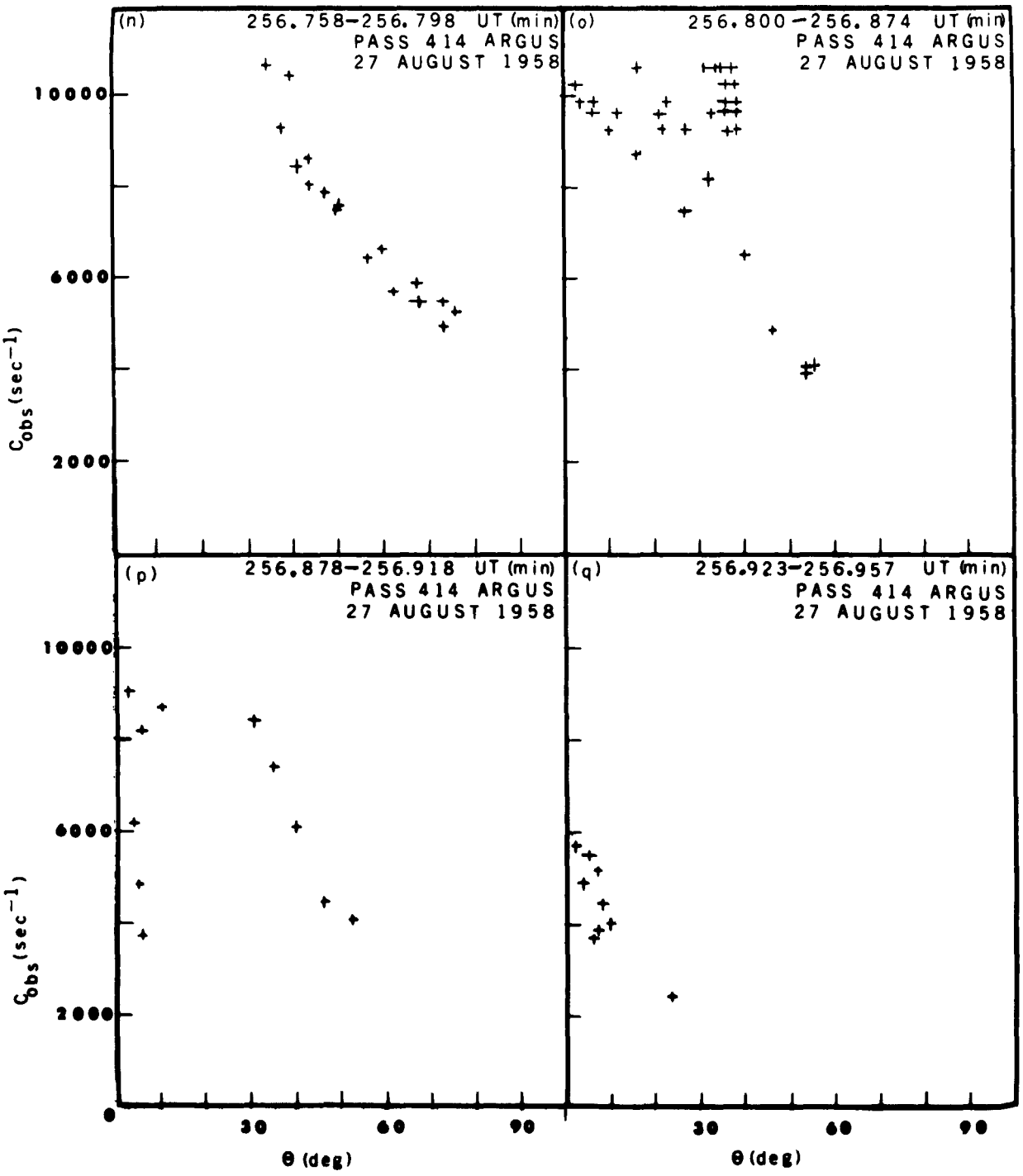
(n)
256.758–256.798 UT (min)
PASS 414 ARGUS
27 AUGUST 1958
(o)
256.800–256.874 UT (min)
PASS 414 ARGUS
27 AUGUST 1958
(p)
256.878–256.918 UT (min)
PASS 414 ARGUS
27 AUGUST 1958
(q)
256.923–256.957 UT (min)
PASS 414 ARGUS
27 AUGUST 1958
10000
6000
2000
0
30
60
90
θ (deg)
C_{obs} (sec^{-1})

Chapter 4

Determination of the Directional Flux Density $J(\theta')$ from Observed Directional Counting Rate $C(\theta)$

4.1 Conversion of the integral equation to matrix form

The directional flux density is related to the directional counting rate by the integral equation

$$C(\theta) = \iint S(\alpha) J(\theta') d\Omega' \tag{4.1}$$

where $C(\theta)$ is the true counting rate (cm^{-2}-sec^{-1}) expressed as a function of the angle between the geomagnetic flux density direction $\hat{B}$ (Fig. 4.1) and the direction of the scintillation counter (Detector A) axis $\hat{P}$, $S(\alpha)$ or $S(\theta, \theta', \phi')$ is the Detector A response function (α, angle between the direction of the counter axis $\hat{P}$ and the unit vector which defines the orientation of the element of solid angle, Fig. 4.1) and $J(\theta')$ is the directional flux density (particles/cm^2sec-ster). The observed counting rate $C_{obs}(\theta)$ is corrected for detector deadtimes to yield the true counting rate $C(\theta)$ by the equation:

$$C(\theta) = \frac{1}{A} \frac{C_{obs}(\theta)}{1 - \tau_D C_{obs}(\theta)} \; ; \tag{4.2}$$

A is the effective area of Detector A (0.005 cm^2; Baicy, 1962); τ_3 is the detector deadtime which has been estimated as 100 microseconds (Chapter 2). From Fig. 4.1 α is related to θ', ϕ' and θ by

$$\cos\alpha = \cos\theta'\sin\theta\sin\phi' + \sin\theta'\cos\theta \; . \qquad (4.3)$$

The Detector A response function $S(\alpha)$ is shown by Fig. 4.2 (Baicy, 1962). A good analytic fit to the curve of Fig. 4.2 is (Weber et al, 1962)

$$S(\alpha) = \exp(\gamma_1\alpha^2 + \gamma_2\alpha^4) \; , \qquad (4.4)$$

where $\gamma_1 = -.00274$, $\gamma_2 = -.000006151$, and α is expressed in degrees. In the determination of $J(\theta')$, integral Eq. (4.1) must be converted to matrix form for computer purposes. To accomplish the evaluation of the integral of Eq. (4.1) in selected intervals of θ', $J(\theta')$ is assumed constant in the interval. For such step-by-step integrals the limits of integration of θ' and ϕ' are determined from an analysis of the possible orientations of the counter axis with respect to the magnetic flux density $\hat{B}$ and the particle flux.

Also cylindrical symmetry of $J(\theta')$ relative to the cylinder axis in the direction of the magnetic flux density $\hat{B}$ was assumed so that $J(\theta') = J(-\theta')$ (where $J(\theta')$ is independent of ϕ'). From the response function Fig. 4.2 it is observed that a cone of half-angle 30° approximately and with its axis along the counter-axis approximately defines the region in which particles will be counted.

However, for the purposes of analysis, a hemisphere instead of a cone is considered for such a geometrical construct does not deviate appreciably from the actual physical situation because of the negligible value of $S(\alpha)$ for $\alpha > 30°$. From Fig. 4.1 it can be seen that the limits of integration of ϕ' depends in general on θ' and θ; ϕ' takes on all values from 0 to 2π for some values of θ' and goes from $0 + \Delta\phi'$ to $2\pi - \Delta\phi'$ for other values; where $\Delta\phi' > 0$ and depend on θ' and θ.

From geometrical considerations, it can be shown that $\Delta\phi' = \text{Arcsin}\,(\tan\theta'\tan\theta)$. In Eq. (4.5) $0 < \theta < \frac{\pi}{2}$ and $-\frac{\pi}{2} < \theta' < \frac{\pi}{2}$. Therefore $(\tan\theta'\tan\theta)$ can be greater than 1 for certain values of θ' and θ. Since $\Delta\phi'$ has to be real, Eq. (4.5) is restricted to those values of θ' and θ for which $\tan\theta'\tan\theta \leq 1$. Also, the value of $\Delta\phi'$ for $(\tan\theta'\tan\theta) > 1$ is required. It is shown readily that Eq. (4.5) is valid in the form

$$\Delta\phi' = \text{Arcsin}\,(\tan\theta'\tan\theta), \quad (\theta+\theta') \leq \frac{\pi}{2}, \qquad (4.5)$$

where $\theta' + \theta > \frac{\pi}{2}$, $\Delta\phi' = 0$.

The analysis above shows that the limits of integration for ϕ' are from 0 to 2π when θ' and θ are such that $\theta' + \theta > \frac{\pi}{2}$; and when $\theta' + \theta \leq \frac{\pi}{2}$, ϕ' ranges from $\Delta\phi'$ to $\pi - \Delta\phi'$ for θ' varying from $-(\frac{\pi}{2} - \theta)$ to 0; ϕ' ranges from $-\Delta\phi'$ to $\pi + \Delta\phi'$ for θ' varying from 0° to $\frac{\pi}{2} - \theta$. Thus Eq. (4.1) can be written in the explicit form

$$C(\theta) = \left\{ \int_{\theta'=\phi-\frac{\pi}{2}}^{0} \int_{\Delta\phi'}^{\pi-\Delta\phi'} + \int_{\theta'=0}^{\frac{\pi}{2}-\theta} \int_{-\Delta\phi'}^{\pi+\Delta\phi'} + \int_{\theta'=\frac{\pi}{2}-\theta}^{\frac{\pi}{2}} \int_{0}^{2\pi} \right\} J(\theta')S(\alpha)\,d\Omega'. \qquad (4.6)$$

To approximate the integral of Eq. (4.6) by a matrix equation it is assumed that $J(\theta')$ varies slightly only when θ' is varied by ± 2.5°. Thus $J(\theta')$ is required only for values of θ' given by $\theta'_i = \Delta\theta'\left(i - \frac{1}{2}\right)$, $i = 1, 2, \ldots 18$; and $\Delta\theta' = 5°$. The value of $J(\theta')$ anywhere inside the interval of width 5° is given by the linear approximation

$$J(\theta') = J(\theta'_i) + \frac{J(\theta'_{i+1}) - J(\theta'_i)}{\theta'_{i+1} - \theta'_i}\left(\theta' - \theta'_i\right) \qquad (4.7)$$

where $\theta'_i < \theta' < \theta'_{i+1}$. A similar type of reduction is carried out for the $C(\theta)$ function. Thus

$C_i = C(\theta_i)$; where $\theta_i = \Delta\theta\left(i - \frac{1}{2}\right)$ and $\Delta\theta = 5°$

Equation (4.6) can now be written as

$$C(\theta) = \sum_{\mu=1}^{M}\left\{\int_{-\bar{\delta}_{\mu+1}}^{-\bar{\delta}_\mu}\int_{\Delta\phi'}^{\pi-\Delta\phi'} + \int_{\bar{\delta}_\mu}^{\bar{\delta}_{\mu+1}}\int_{-\Delta\phi'}^{\pi+\Delta\phi'}\right\} J(\bar{\delta}_\mu)S(\alpha)\,d\Omega'$$

$$+ \sum_{\mu=M+1}^{18} J(\bar{\delta}_\mu)\int_{\delta_\mu}^{\delta_{\mu+1}}\int_0^{2\pi} S(\alpha)\,d\Omega' \qquad (4.8)$$

where $\bar{\delta}_\mu = 5°(\mu - \frac{1}{2})$, $\delta_\mu = 5°(\mu - 1)$ and the value of the integer M is to be chosen such that $\theta'_i + \theta_j \leq \frac{\pi}{2}$. Now, noting that $J(\theta') = J(-\theta')$ and also assuming that $J(\theta')$ to be linear in a sub-interval of width 5°, the integral Eq. (4.8)

reduces to

$$C(\theta_i) = C_i = \sum_{\mu=1}^{M} J_\mu \int_{-\xi_{\mu+1}}^{-\xi_\mu} \int_{\Delta\phi'_{\mu i}}^{\pi - \Delta\phi'_{\mu i}} S_i(\alpha)\, d\Omega' +$$

$$\sum_{\mu=1}^{M} J_\mu \int_{\xi_\mu}^{\xi_{\mu+1}} \int_{-\Delta\phi'_{\mu i}}^{\pi + \Delta\phi_{\mu i}} S_i(\alpha)\, d\Omega' + \sum_{\mu=M+1}^{18} J_\mu \int_{\xi_\mu}^{\xi_{\mu+1}} \int_{\phi'=0}^{2\pi} S_i(\alpha)\, d\Omega' \; ; \qquad (4.9)$$

where $d\Omega' = \cos\theta' d\theta' d\phi'$,

$\Delta\phi'_{i\mu} = \text{Arcsin}\,(\tan\theta'_\mu \tan\theta_i)$,

$S_i(\alpha) = S(\theta_i, \theta', \phi')$.

It can be shown that the value of M depends on the index i and is given by 18- i. The number 18 is the number of sub-intervals of width 5° in the interval $0° < \theta' < 90°$. Equation (4.9) can be written in the matrix form

$$C_i = \sum_{j=1}^{18} S_{ij} J_j \; , \quad i,j = 1,2,\ldots 18; \qquad (4.10)$$

where $J_j = J(\theta'_j)$,

and $$S_{ij} = \left\{ \int_{-\xi_{j+1}}^{-\xi_j} \int_{\Delta\phi'_{ij}}^{\pi - \Delta\phi'_{ij}} + \int_{\xi_j}^{\xi_{j+1}} \int_{-\Delta\phi'_{ij}}^{\pi + \Delta\phi'_{ij}} \right\} S_i\, d\Omega', \; i+j \le 19;$$

or, $$S_{ij} = \int_{\xi_j}^{\xi_{j+1}} \int_{0}^{2\pi} S_i(\alpha)\, d\Omega' \; , \quad \text{for} \quad i+j > 19 \; .$$

Thus the reduction of the integral form of Eq. (4.1) to the matrix form of Eq. (4.10) is completed when all the 324 elements of the S-matrix are determined. These matrix elements have been computed using the techniques of numerical integration. If $J(\theta')$ is considered independent of θ', the counting rate would be independent of direction of the counter axis and hence the sum $\sum_{j=1}^{18} S_{ij}$ should be independent of the index i. The computed values of the S-matrix elements have been shown to satisfy this condition with considerable accuracy (per cent differences are of the order of .025%).

4.2 Inversion of the matrix equation, Equation (4.10)

The determination of J_i involves solving 18 simultaneous equations, Eqs. (4.10). For a given set of C_i, a unique solution exists if the det(S)$\neq$ zero. In the present case, the S-matrix elements have the physical interpretation of an approximate measure of the resolving power of the directional detector. The det(S)=zero has the physical meaning that the scintillation counter would have zero directional sensitivity. From the shape of the response function, the determinant of S should be non-zero. However, it has been found that det(S)$\cong 10^{-27}$. However, it has been possible to invert the S-matrix with sufficient accuracy using an IBM 1620 computer so that numbers less than 10^{-99} only are treated as zero. Mathematically, the problem is straightforward once the inverted S-matrix elements are computed since the J_i can then be determined by the matrix equation

$$J_i = \sum_{j=1}^{18} (S^{-1})_{ij} C_i \quad , \quad i = 1, 2, \ldots 18. \tag{4.11}$$

The accuracy of the matrix inversion has been tested by computing the product $D_{ij} = \sum_{k=1}^{18} S^{-1}_{ik} S_{kj}$ and comparing it with the identity matrix. This comparison shows that for an assumed set of J_i used to compute a set of C_j by Eq. (4.10), the computed values of J_i determined by Eq. (4.11) are correct within ±.01%. This accuracy will be maintained if the C_j values are known accurately; ie, within an error determined mainly by the magnitude of the inverted S-matrix elements.

If "measured" values of C_i are derived from the flux density function $J(\theta')$ then the actual C_i values are obtained from the basic Eq. (4.1). If the measured values of C_i are denoted by C_i'' and related to C_i by the equation $C_i'' = C_i + \Delta_i$, where the actual value of Δ_i is not known, then by Eq. (4.11)

$$\begin{aligned} J_k' &= \sum_{i=1}^{18} (S^{-1})_{ki} C_i'' \quad , \\ &= \sum (S^{-1})_{ki} [\, C_i + \Delta_i \,] \quad , \\ &= \sum (S^{-1})_{ki} \Delta_i + J_k \\ &= \Delta J_k + J_k \quad , \qquad \Delta J_k = \sum (S^{-1})_{ki} \Delta_i \, . \end{aligned} \tag{4.12}$$

By Eq. (4.12) it can be seen that the error in the computed value of J is proportional to the absolute value of $(S^{-1})_{ij}$ for a given set of Δ_i. It has been found that the values of the inverted matrix elements lie between -5000 and +5000 so that an error of 1% in the counting rate would give rise to unreliable J-values. Although S^{-1} has been computed with sufficient accuracy, owing to the smallness of det(S), small errors in C_i can produce physically meaningless J_j ; this has been tested by using C values with assumed values of Δ_i and it has

been found that the measured C-values are not accurate enough to produce physically meaningful J_j by Eq. (4.11). Hence it has become necessary to search for other methods of solving ill-conditioned matrix equations. Recently, a new method has been developed to solve such ill-conditioned equations. The method essentially involves the construction of a matrix C which satisfies the sum condition on S^{-1} and which produces approximately the same result as S^{-1} when very accurate data is used. For this, it is expected that the C-matrix elements will be small in magnitude and tend to form the S^{-1} matrix elements in a certain limiting case. The computed C-matrix elements do satisfy these conditions and have been tested in many cases of assumed $J(\theta')$ functions and have been found to be satisfactory for the present problem. An outline of the derivation of the C-matrix is given as follows:

For the equations

$$\begin{aligned} C_1 &= S_{11}J_1 + S_{12}J_2 \\ C_2 &= S_{22}J_2 + S_{21}J_1 \\ C_3 &= S_{31}J_1 + S_{32}J_2 \end{aligned} \tag{4.13}$$

where J_1 and J_2 are the unknowns, using only one pair out of three possible pairs, two unique values of J_i can be determined provided that the corresponding coefficient determinants are not zero. But if a small error is introduced in the value of C_3 such that $C_3 + E_3 = S_{31}J_1 + S_{32}J_2$ then there are three different pairs of J-values (J_1^1, J_2^1), (J_1^2, J_2^2), (J_1^3, J_2^3) corresponding to the three pairs of C-values, (C_1, C_2), (C_1, C_3), (C_2, C_3). However, from

the construct

$$\begin{pmatrix} \bar{J}_1 \\ \bar{J}_2 \end{pmatrix} = \begin{pmatrix} (B^{-1})_{11} & (B^{-1})_{12} \\ (B^{-1})_{21} & (B^{-1})_{22} \end{pmatrix} \begin{pmatrix} S_{11} & S_{21} & S_{31} \\ S_{12} & S_{22} & S_{32} \end{pmatrix} \begin{pmatrix} C_1 \\ C_2 \\ C_3+E_3 \end{pmatrix} \tag{4.14}$$

where

$$(B) = \begin{pmatrix} S_{11} & S_{21} & S_{31} \\ S_{12} & S_{22} & S_{32} \end{pmatrix} \begin{pmatrix} S_{11} & S_{12} \\ S_{21} & S_{22} \\ S_{31} & S_{32} \end{pmatrix}$$

it can be seen that the solution obtained from Eq. (4.14) may be distinct from all the three pairs $(J_1^1, J_2^1), (J_1^2, J_2^2), (J_1^3, J_2^3)$ owing to the fact that the error in C_3 has been averaged out in some way in producing the set $(\bar{J}_1, \bar{J}_2)$. Also, it can be seen that in the limit of $E_3 = 0$, the solution produced by Eq. (4.14) is the same as any one of the pairs $(J_1^1, J_2^1), (J_1^2, J_2^2), (J_1^3, J_2^3)$. This method of averaging out the error in the data can be generalized to the case of a square matrix by using an intermediate matrix which has the effect of averaging the errors in the counting rate values.

Thus, consider

$$\left\{ \Psi_\mu \mid \mu = 1,2,\cdots \right\}, \quad \int_{-\pi}^{\pi} \Psi_\mu \Psi_\nu \, d\theta' = \delta_{\mu\nu} ;$$

$$J(\theta') = \sum_{\mu=1}^{N} A_\mu \Psi_\mu(\theta') ; \tag{4.15}$$

$$J_i = J(\theta_i') = \sum_{\mu=1}^{N} A_\mu \Psi_\mu(\theta_i') = \sum_{\mu=1}^{N} \Psi_{i\mu} A_\mu , \; N \leq 18 ;$$

so that Eq. (4.10) can be written

$$C_i = \sum_{j=1}^{18} S_{ij} J_j \ ;$$
$$= \sum_{j=1}^{18} S_{ij} \left(\sum_{\mu=1}^{N} \Psi_{j\mu} A_\mu \right), \ \Psi_{j\mu} = \Psi_\mu(\theta_j) \ ;$$
$$= \sum_{\mu=1}^{N} \left(\sum_{j=1}^{18} S_{ij} \Psi_{j\mu} \right) A_\mu \ .$$

Next, define

$$T_{i\mu} = \sum_{j=1}^{18} S_{ij} \Psi_{j\mu} \ , \tag{4.16}$$

$$C_i = \sum_{\mu=1}^{N} T_{i\mu} A_\mu \ . \tag{4.17}$$

Multiplication of both sides of Eq. (4.17) by the transposed T yields

$$\sum_{i=1}^{18} T_{i\nu} C_i = \sum_{i=1}^{18} \sum_{\mu=1}^{N} (T_{i\nu} T_{i\mu}) A_\mu = \sum_{\mu=1}^{N} B_{\nu\mu} A_\mu \ , \tag{4.18}$$

where $$B_{\nu\mu} = \sum_{i=1}^{18} (T_{i\nu} T_{i\mu})$$

and multiplication of both sides of Eq. (4.18) by the inverse of the B-matrix, yields further

$$\sum_{i=1}^{18} \sum_{\nu=1}^{N} (B^{-1})_{\gamma\nu} T_{i\nu} C_i = \sum_{\nu=1}^{N} \sum_{\mu=1}^{N} (B^{-1})_{\gamma\nu} B_{\nu\mu} A_\mu$$
$$= \sum_{\mu=1}^{N} \delta_{\gamma\mu} A_\mu = A_\gamma \ . \tag{4.19}$$

By Eq. (4.15) substituting A_γ from Eq. (4.19), yields

$$A_\gamma = \sum_{i=1}^{18} \sum_{\nu=1}^{N} (B^{-1})_{\gamma\nu} T_{i\nu} C_i \ ,$$

$$J_j = \sum_{\mu=1}^{N} \Psi_{j\mu} A_\mu \ ,$$

$$= \sum_{\mu=1}^{N} \Psi_{j\mu} \sum_{i=1}^{18} \sum_{\nu=1}^{N} (B^{-1})_{\mu\nu} T_{i\nu} C_i \ ; \qquad (4.20)$$

$$= \sum_{i=1}^{18} \left(\sum_{\mu=1}^{N} \sum_{\nu=1}^{N} \Psi_{j\mu} (B^{-1})_{\mu\nu} T_{i\nu} \right) C_i \ .$$

Equation (4.20) becomes, by interchanging the order of summation,

$$J_j = \sum_{i=1}^{18} C_{ji} C_i \ ,$$

where $$C_{ij} = \sum_{\mu=1}^{N} \sum_{\nu=1}^{N} \Psi_{i\mu} (B^{-1})_{\mu\nu} T_{j\nu} \ ; \qquad (4.21)$$

Equation (4.21) is of the form $$J_j = \sum_{i=1}^{18} (S^{-1})_{ji} C_i \ .$$

It can be shown that in deriving the C-matrix, the value of **N** must be chosen less than the maximum value which the **i** or **j** index can take (here, it is 18). When **N** is greater than 18, the determinant of **B** can be shown to be zero which renders the C-matrix meaningless. When

$N = 18$, it can be seen that $C_{ij} = (S^{-1})_{ij}$ for all allowed i, j values. Hence N should be chosen less than 18. It is to be noted that for N too close to 1 the initial approximation of a function $J(\theta')$ by a few elements of an orthonormal set becomes inaccurate when the range of θ' is large. Thus an optimisation of N was attempted from both theoretical and experimental sides and it was found that a good value of N is 12 for the case of a polynomial of even powers is used for the orthonormal set. It has been determined further that the selection of N should be based on (1) the predicted error in the C-values, (2) the rate at which C drops to its minimum, (3) the error in recomputing the C-values from the J-values computed from Eq. (4.20), (4) the type of orthonormal set used in computing the C-matrix. The analysis has shown that in the computation of using Eq. (4.20) the selection of N based on item (3) can be attained by computing the C-matrix elements for $N = 3, 4, 5, 6, 7, 8$ and using cosine functions as the basic orthonormal set of even functions. Thus, in a more explicit form, Eq. (4.20) may be written

$$J_i^N = \sum_{j=1}^{18} C_{ij}^N C_j \quad , \quad N = 1, 2, \cdots, 17. \tag{4.22}$$

In the final determination of J_j, a selection is made out of the set $(J^1, J^2, J^3, J^4, J^5, J^6)$ based on the accuracy with which the input C-values can be recomputed from

$$C_i^N = \sum_{j=1}^{18} S_{ij} J_j^N = \sum_{j=1}^{18} \sum_{k=1}^{18} S_{ij} C_{jk}^N C_k \tag{4.23}$$

It was determined that in all practical cases, the percentage difference $D_i^N = 200\,(C_i^N - C_i)/(C_i^N + C_i)$ is within 5% which is less than the errror in the C-data.

4.3 Directional count-rates $C_{obs}(\theta)$ and $C(\theta)$ and flux densities $J(\theta')$ vs θ, θ' for Natural and ARGUS trapping. Results and conclusions.

The analysis and procedure of Secs. 4.1 and 4.2 above were applied to Passes 414 and 454 of Explorer IV over Huntsville, Alabama for both the Natural and ARGUS trapping to attain observed count-rates $C_{obs}(\theta)$ and true count-rates (observed count-rates corrected for deadtimes, effective counter area and efficiency) $C(\theta)$ vs θ (between scintillation counter axis and the plane perpendicular to the geomagnetic field), and directional flux densities $J(\theta')$ vs θ'. Figures 4.3, 4.4, 4.5 and 4.6 along with explanatory captions are the results.

Any conclusions concerning the directional flux density distribution of trapped particles must be considered as tentative since Passes 414 and 454 only have been analysed for $J(\theta')$ vs θ'. The reason for the limited amount of data analysed to date is the inherent nature of the ARGUS trapping. A great deal of computational work is involved in the analysis of the data to achieve directional flux density distributions for ARGUS trapping as has been noted in Chaps. 2, 3, 4. It is necessary to analyse each modulation of the observed count-rate C_{obs} vs time (see Figs. 2.9, 2.10, 2.11 Lower) separately to attain a series of corresponding $J(\theta')$ vs θ' curves. In the present work this detailed analysis has been completed for Pass 414 only. For the limited results indicated by Figs. 4.3 - 4.6 the following "conclusions" are suggested

(1) The natural directional flux density distributions $J(\theta')$ vs θ' (Pass 414, Fig. 4.3 lower right; Pass 454, Fig. 4.5 right) are roughly constant in space and time in good agreement with early published results (Weber, et al 1962). The essential characteristics for the naturally

trapped radiation are

Pass	$J(\theta')$ maximum	Half-width at half-maximum (h w h m)
414	7×10^7 cm^{-2}sec^{-1}ster^{-1}	21°
454	5×10^7 cm^{-2}sec^{-1}ster^{-1}	28°

The maximum flux densities $J(\theta')$ maximum noted are in excess of those previously reported for nearby regions of space because of corrections resulting from the more recent calibrations (Baicy, et al, 1963).

(2) The ARGUS directional flux density distributions for the trapped particles are more variable in shape both with time and space location than are the corresponding natural radiations. The ARGUS $J(\theta')$ vs θ' curves (Pass 414, Fig. 4.4 lower; Pass 454, Fig. 4.6 right) are generally flatter (near the maximum of the curves) than for the corresponding natural radiation. Especially, the $J(\theta')$ vs θ' half-width at half-maximum appears to be a variable which may change for each modulation of the count-rate (see C_{obs} vs time curves, Figs. 2.9, 2.10, 2.11 Lower). As discussed in Sec 3.4 the important factor in the $J(\theta')$ vs θ' shape variation appears to be the variation in the omnidirectional penetrating background radiation which is shown by curves B in Figs. 2.10 and 2.11 Lower. The essential characteristics for the ARGUS trapped radiation are

Pass	$J(\theta')$ maximum	Half-width at half-maximum (h w h m)
414	$(1.0\text{-}1.9) \times 10^8$ cm^{-2}sec^{-1}ster^{-1}	24-30°
454	0.65×10^8 cm^{-2}sec^{-1}ster^{-1}	16°

It is necessary clearly that a great deal more data analysis for ARGUS trapping is required to understand more fully the directional flux density distributions $J(\theta')$ vs θ'. From such results the ARGUS mirror point distributions would be obtained immediately.

Fig. 4.1. Geometry involving scintillation counter axis direction ($\hat{P}$, unit vector), magnetic flux density direction ($\hat{B}$, unit vector), particle flux density direction (specified by solid angle $d\Omega'$ orientation) and various angles.

$$\cos\alpha = \cos\theta' \sin\theta \sin\phi' + \sin\theta' \cos\theta$$

and $d\Omega' = \cos\theta' \, d\theta' \, d\phi'$.

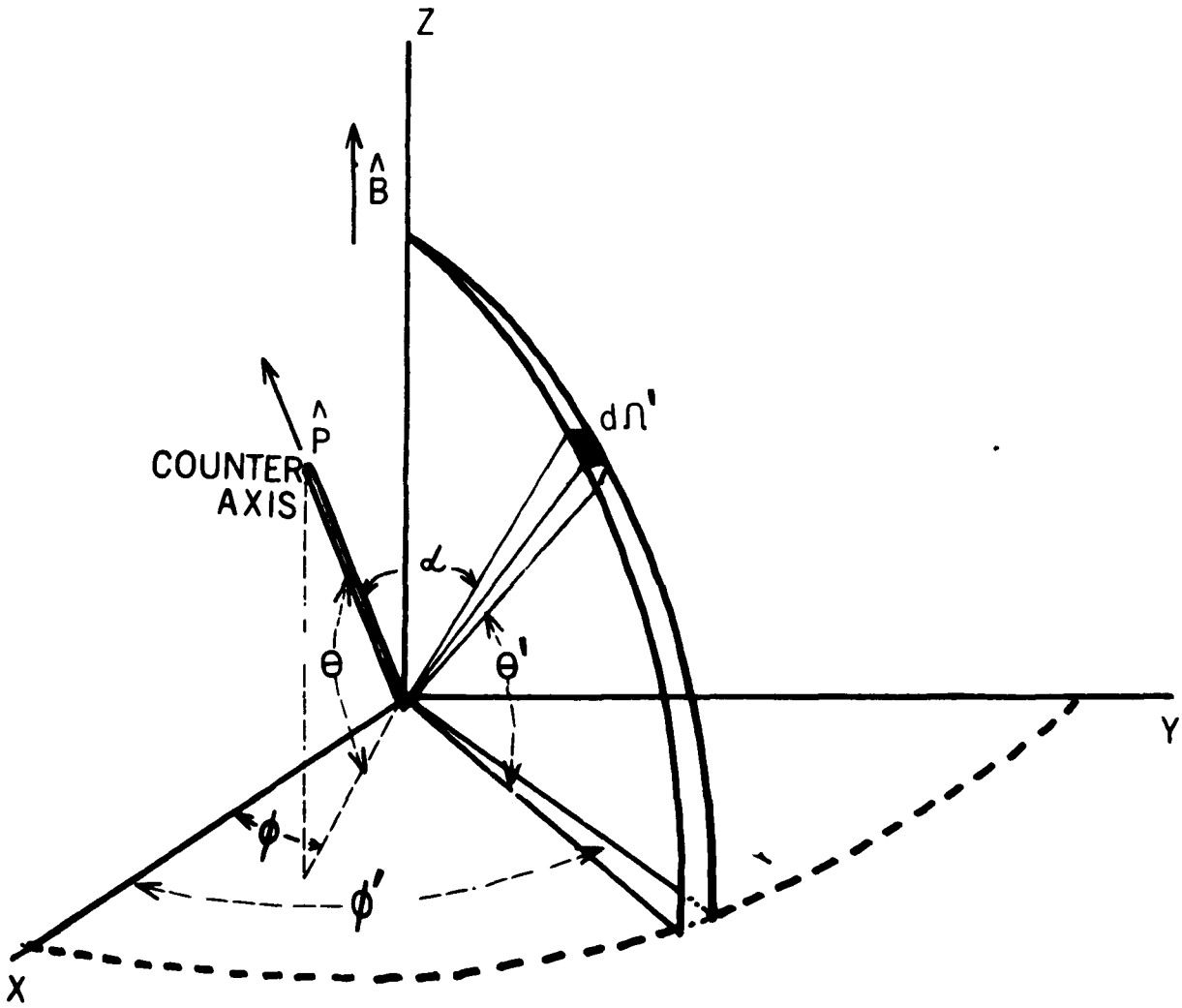
Z
B
P
COUNTER
AXIS
dΩ'
α
θ
θ'
Y
φ
φ'
X

Fig. 4.2. Response of $S(\alpha)$ of Detector A, directional scintillation counter, vs the angle α between the counter axis and the direction of the incident β-radiation (Baicy et al, 1962).

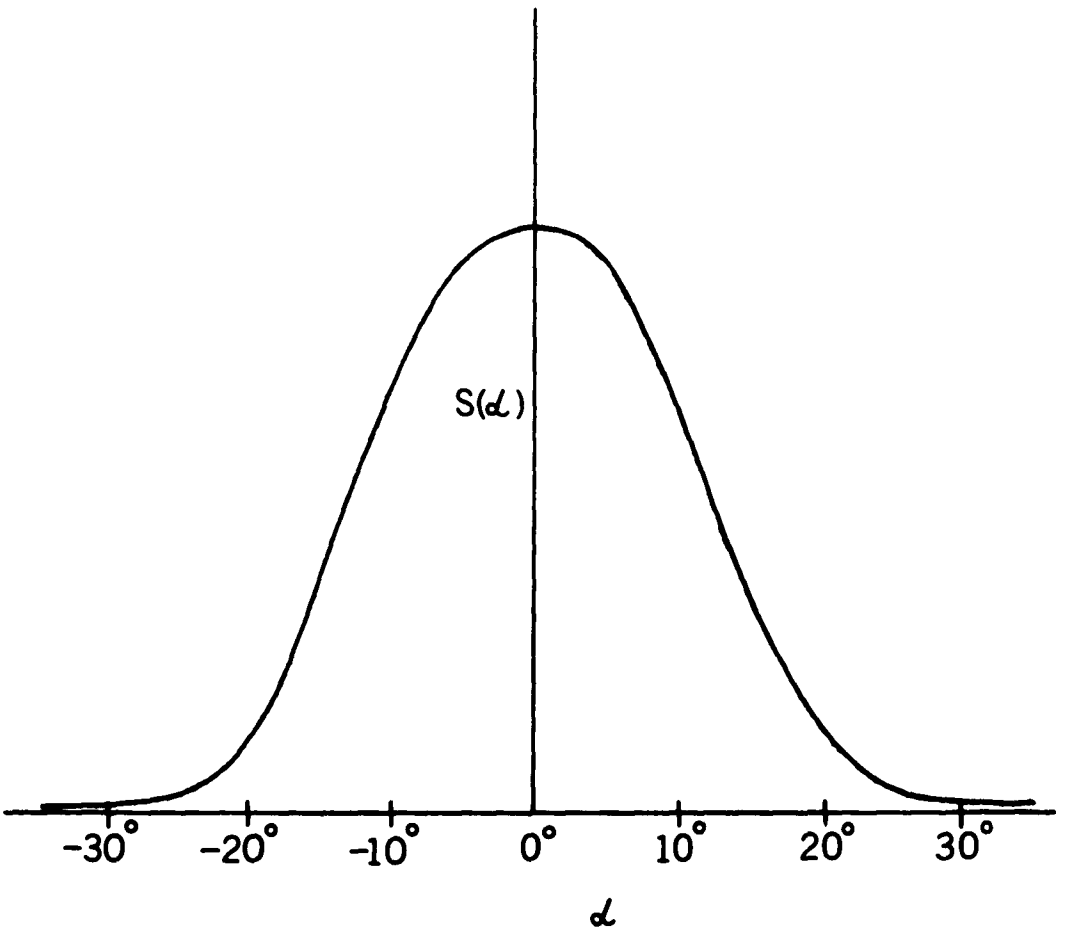
S(α)
-30°
-20°
-10°
0°
10°
20°
30°
α

Fig. 4.3 Directional count-rates and flux densities of naturally trapped radiation vs angle θ (between counter axis and plane perpendicular to geomagnetic field direction) obtained by analysis of the data from the scintillation counter (Detector A) on Explorer IV a few minutes before entering the ARGUS region (Event I), Pass 414.

The space location data are (for 250.0 UT): geographic latitude and longitude, 3.8° N and 276° E respectively; L, 1.40; B, 0.164 gauss; altitude, 1781 km.

Upper and lower left. Observed count-rates $C_{obs}(\theta)$ for time intervals noted on plots. Count-rates obtained as explained in Chap. 2. The plotted points are located by the numbers along the curve; numerals 1, 2, 3, 4, 5 indicate count-rate vs θ for individual modulations as shown by Fig. 2.9. The dashed portions of the curves are theoretical extrapolations.

Upper and lower right. True count-rate $C(\theta)$ obtained by correcting $C_{obs}(\theta)$ for deadtime, effective area and counting efficiency of the scintillation detector. Directional flux densities $J(\theta')$ obtained as explained in Chap. 4.

The $J(\theta')$ cutoff and half-width at half-maximum (h w h m) are about 72° and 21° respectively for the lower right plot.

Fig. 4.4 Directional count-rates and flux densities vs θ for the scintillation counter during penetration of the ARGUS region (Event I) a few minutes later than for Fig. 4.3. $C_{obs}(\theta)$, $C(\theta)$, and $J(\theta')$ were obtained as for Fig. 4.3.

The space location data are (for 256.3 UT): geographic latitude and longitude, 17.6° N and 285.5° E respectively; L, 1.68; B, 0.221 gauss; altitude, 1518 km.

The lower case letters b, c, e relate the data of Fig. 4.4 with that of Fig. 2.10 Lower where the same letters are employed for corresponding data.

The dotted portions of the curves are theoretical extrapolations.

The $J(\theta')$ cutoff and h w h m are about 75° and 24° respectively for the lower right plot.

Fig. 4.5 Directional count-rates and flux densities of naturally trapped radiation vs θ obtained by analysis of data from the scintillation counter (Detector A) a few minutes before Explorer IV entered the ARGUS region (Event II), Pass 454. $C_{obs}(\theta)$, $C(\theta)$, and $J(\theta')$ were obtained as for Fig. 4.3. The dotted portion of the curve is a theoretical extrapolation.

The space location data are (for 299, UT): geographic latitude and longitude, 4° N and 250° E respectively; L, 1.35; B, 0.157 gauss; altitude, 1875 km.

The $J(\theta')$ cutoff and h w h m are about 60° and 28° respectively.

Fig. 4.6 Directional count-rates and flux densities vs θ for the scintillation counter during penetration of the ARGUS region (Event II) a few minutes later than for Fig. 4.5. $C_{obs}(\theta)$, $C(\theta)$, and $J(\theta')$ were obtained as for Fig. 4.3. The dotted portion of the curve is a theoretical extrapolation.

The space location data are (for 310, UT): geographic latitude and longitude, 27.8°N and 270° E; L, 2.08; B, 0.269 gauss; altitude, 1405 km.

The $J(\theta')$ cutoff and h w h m are about 40° and 16° respectively.

Chapter 5

Omnidirectional Count-Rate versus Time. Decays of Omnidirectional Radiation.

5.1 Analysis of omnidirectional count-rates, Detectors D and C, Explorer IV

An analysis was made of the data obtained through Channels 1 (Detector D) and 3 (Detector C), the shielded (1.6 g/cm^2, lead) and unshielded Anton 302 G-M counters respectively (see Fig. 2.1 block diagram). Detector C had no intentional shielding beyond that of the satellite shell and contents and was sensitive to electrons of energy greater than 3 MeV. The shielded Detector D had an electron energy threshold of 6 MeV.

An automatic digitizer was used to analyse the telemetry playback data and transform it to punch cards and a computer program was used to obtain true count-rate by correcting for the counter deadtime, 62.5 microseconds. The Explorer IV Passes selected for analysis were those over the Huntsville ground station, as follows

ARGUS Event I

	Pass	Pass	Pass
August 27, 1958	414	415	416
August 28, 1958	427		
August 29, 1958	440		
August 30, 1958	453	454	
August 31, 1958	466		

	Pass	Pass	Pass
September 1, 1958	479		
September 2, 1958	492		
September 3, 1958	505		
September 4, 1958	518		

ARGUS Event II

August 30, 1958	453	454	455
August 31, 1958	466		
September 1, 1958	479		
September 2, 1958	492		

(The Passes tabulated above are arranged in 3 columns each of which corresponds to about the same region in space relative to the earth - the Explorer IV satellite orbital frequency was about 13 orbits/day).

Figures 5.1 and 5.2 are sets of omnidirectional count-rate data plots corresponding respectively to ARGUS Events I and II. The figure captions contain explanatory information. The curves shown are smoothed averages of true (corrected) count-rates with the actual points not included.

Figures 5.3, 5.4 and 5.5 show the decay of the ARGUS shell versus time elapsed T_e since Event I, or II, for various L (B-L geomagnetic coordinates) values. In Fig. 5.3 the data points for Passes 505 and 518 exhibit increases in ARGUS shell intensity (count-rates) which are due probably to a geomagnetic disturbance (Report, State University of Iowa, 1959).

D, Difference [A (unshielded) - B (shielded)] count-rates vs time. Assuming that electrons only are counted the difference A-B measures roughly the omnidirectional counts/sec due to all electrons of energy between 3 and 6 MeV. The differences A-B are for count-rates above background.

T_e, time elapsed (approximately) since Event I.

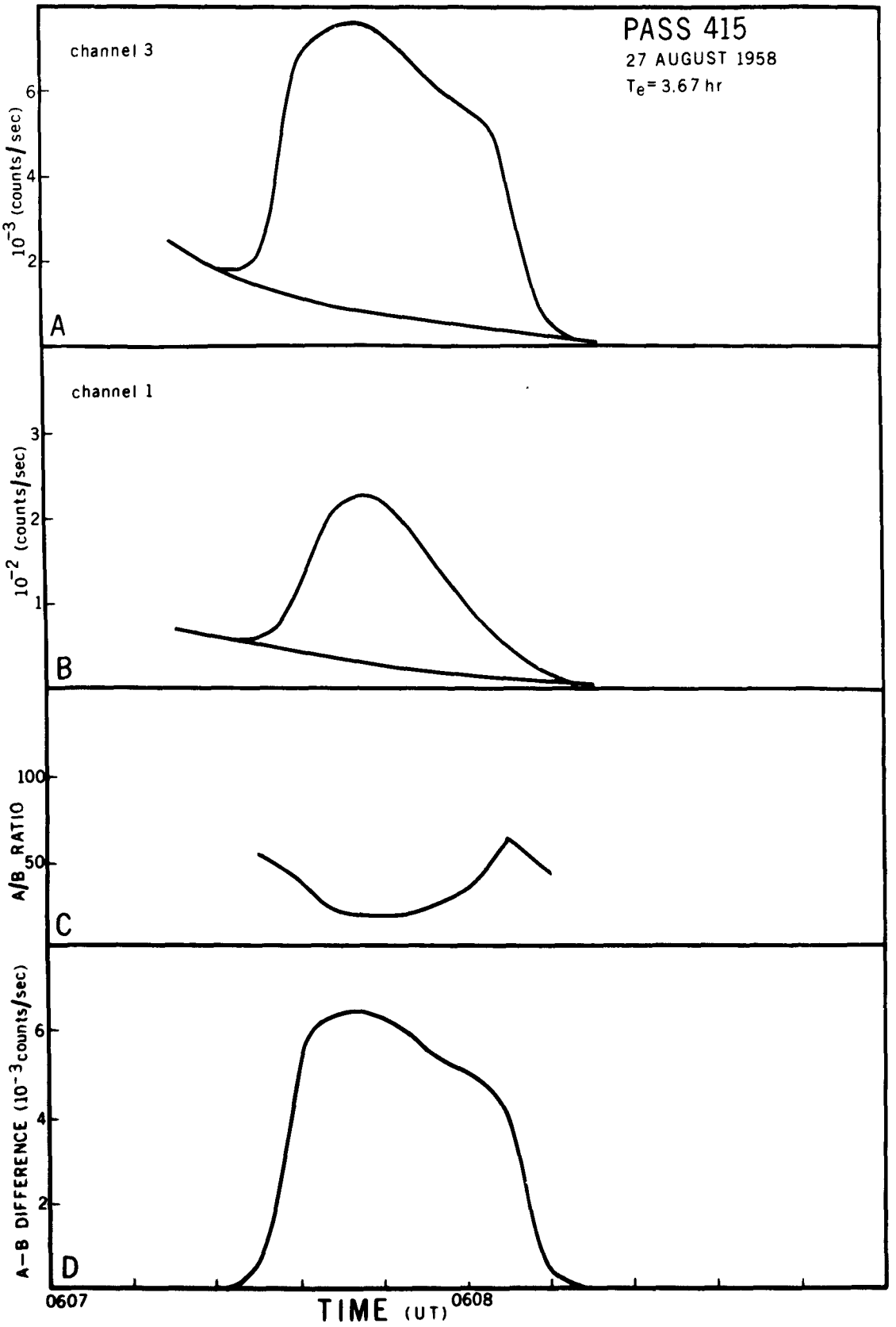
PASS 415
27 AUGUST 1958
T_e = 3.67 hr
channel 3
10^{-3} (counts/sec)
A
channel 1
10^{-2} (counts/sec)
B
A/B RATIO
C
A-B DIFFERENCE (10^{-3} counts/sec)
D
0607
TIME (UT)
0608

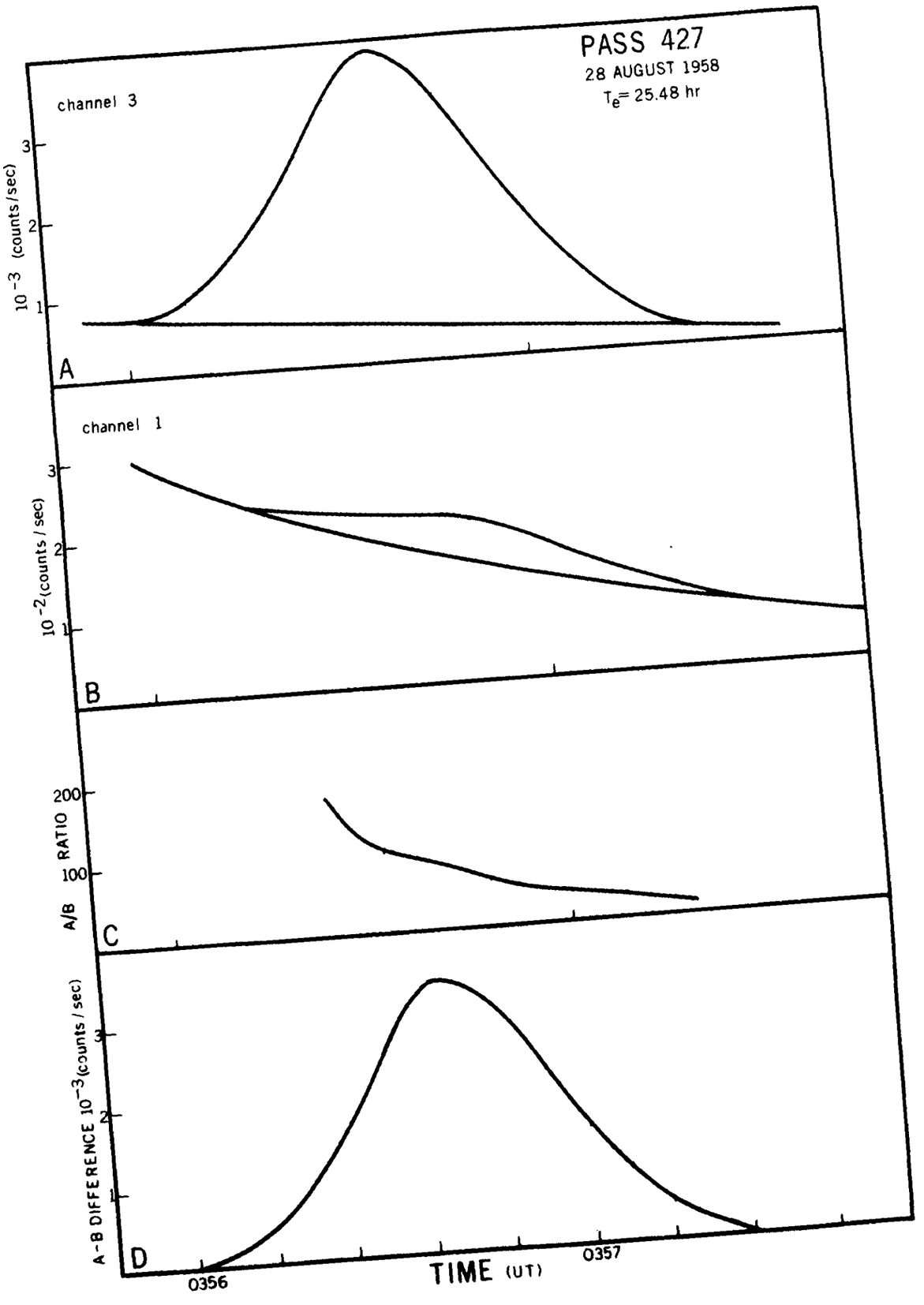
PASS 427
28 AUGUST 1958
T_e= 25.48 hr
channel 3
10^{-3} (counts/sec)
A
channel 1
10^{-2}(counts / sec)
B
A/B RATIO
C
A-B DIFFERENCE 10^{-3}(counts / sec)
D
0356
TIME (UT)
0357

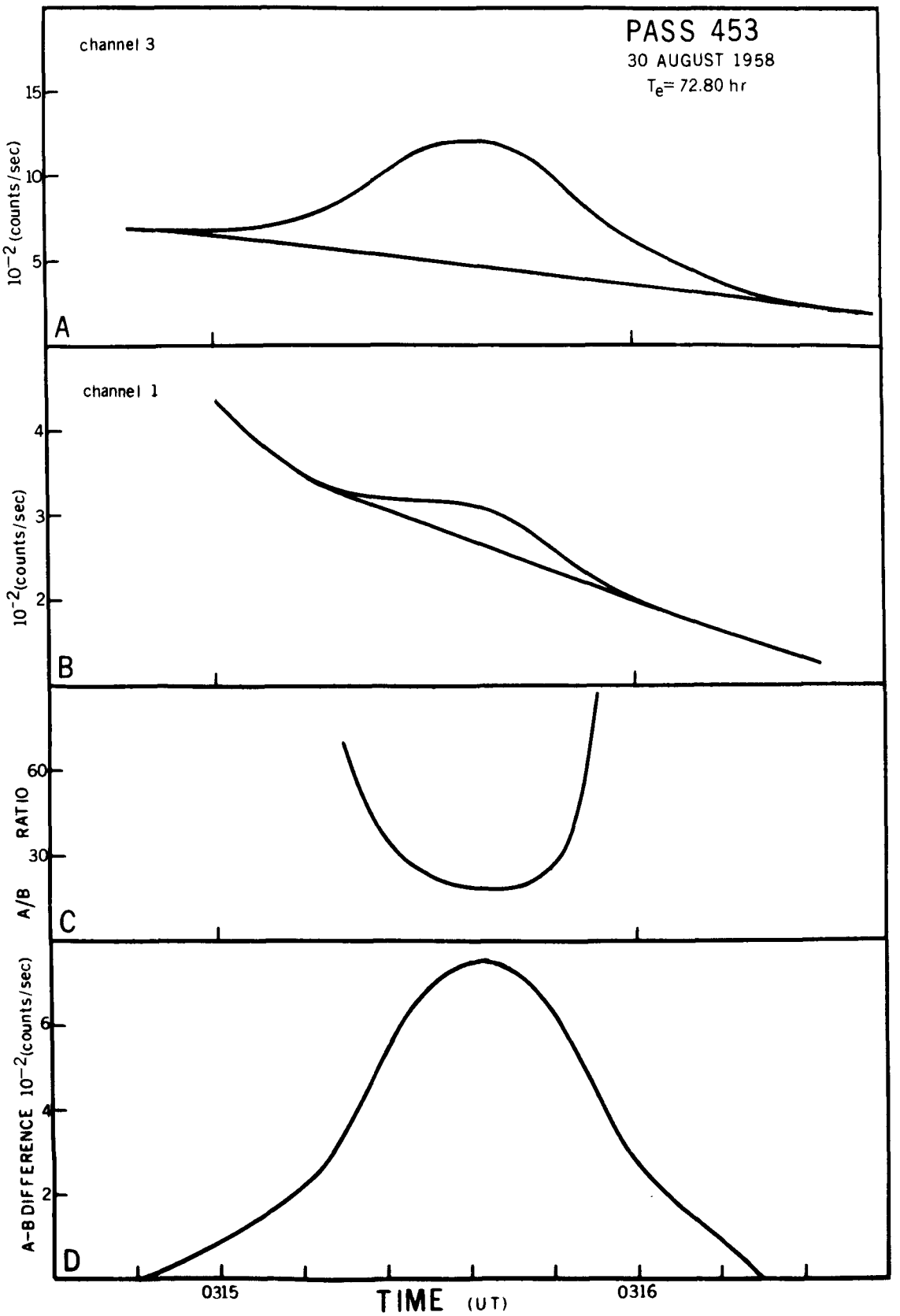
PASS 453
30 AUGUST 1958
T_e= 72.80 hr
channel 3
15
10
5
10^{-2} (counts/sec)
A
channel 1
4
3
2
10^{-2}(counts/sec)
B
60
30
A/B RATIO
C
6
4
2
A-B DIFFERENCE 10^{-2}(counts/sec)
D
0315
TIME (UT)
0316

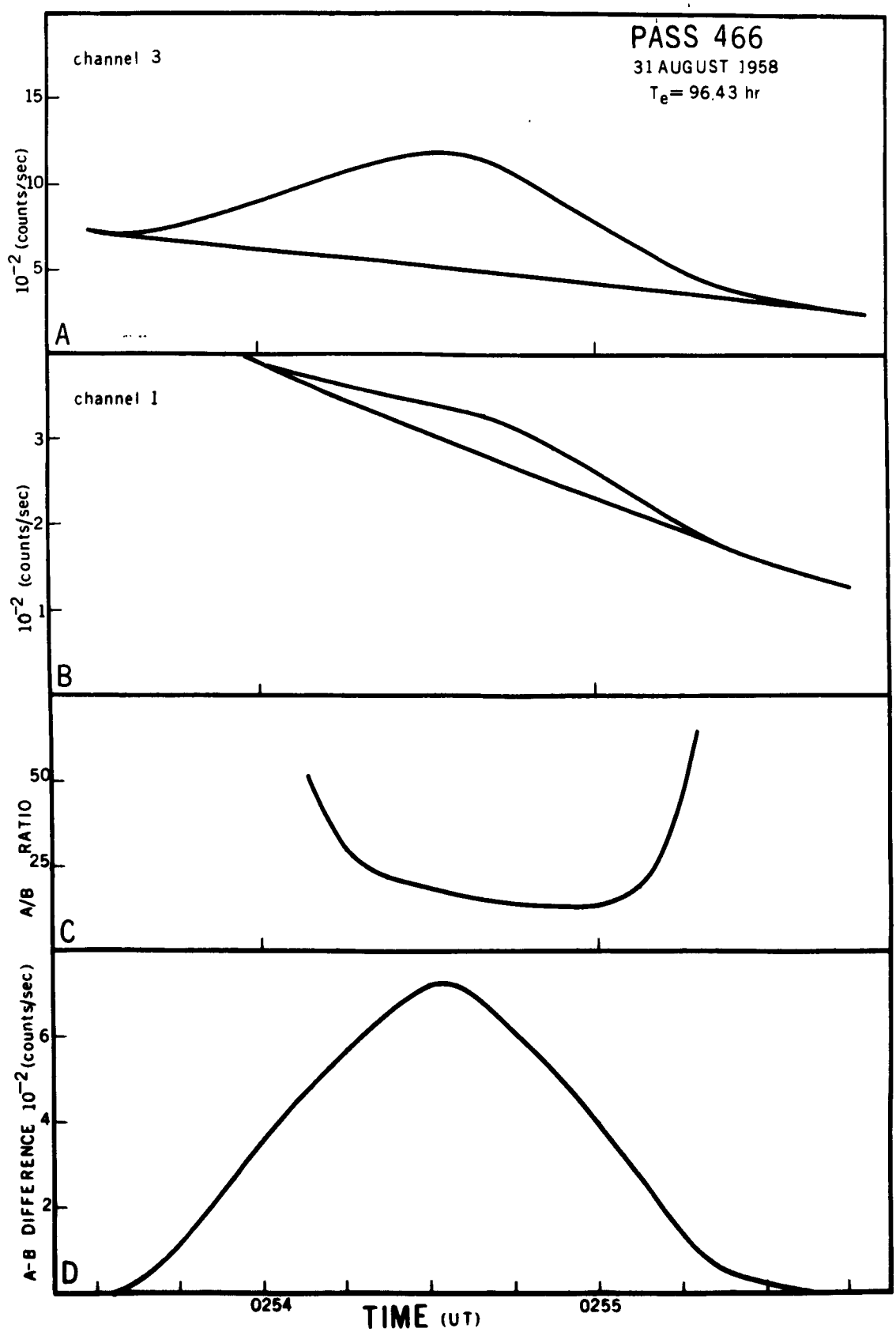
PASS 466
31 AUGUST 1958
T_e = 96.43 hr
channel 3
15
10
5
10^{-2} (counts/sec)
A
channel 1
3
2
1
10^{-2} (counts/sec)
B
50
25
A/B RATIO
C
6
4
2
A-B DIFFERENCE 10^{-2} (counts/sec)
D
0254
0255
TIME (UT)

Figs. 5.2 True count-rate vs time for omnidirectional G-M counters during ARGUS shell penetrations following Event II for Passes 453, 454, 455, 466 and 479 of Explorer IV Satellite over Huntsville, Alabama. The data have been smoothed so that the various curves are averages of points which are not plotted.

The set of 4 plots for each Pass are arranged as follows:

A, unshielded G-M counter (Detector C, Channel 3) which counts electrons of energy greater than 3 MeV; the background has been drawn in by estimation.

B, shielded G-M counter (Detector D, Channel 1) which counts electrons of energy greater than 6 MeV; the background has been drawn in by estimation.

C, Ratio of A (unshielded)/B (shielded) count-rates vs time. Assuming that electrons only are counted the A/B ratio can be expressed

$$\text{Ratio } A/B = \left[\left(\int_{3\text{MeV}}^{\infty} N(E)\, dE\right)/\left(\int_{6\text{MeV}}^{\infty} N(E)\, dE\right)\right]_t$$

where N(E) is the true omnidirectional counts/sec per energy interval in MeV, and t is the time as noted by the abscissa. The ratios are of count-rates above background.

D, Difference [A (unshielded) - B (shielded)] count-rates vs time. Assuming that electrons only are counted the difference A-B measures roughly the omnidirectional counts/sec due to all electrons of energy between 3 and 6 MeV. The differences A-B are for count-rates above background.

T_e, time elapsed (approximately) since Event II.

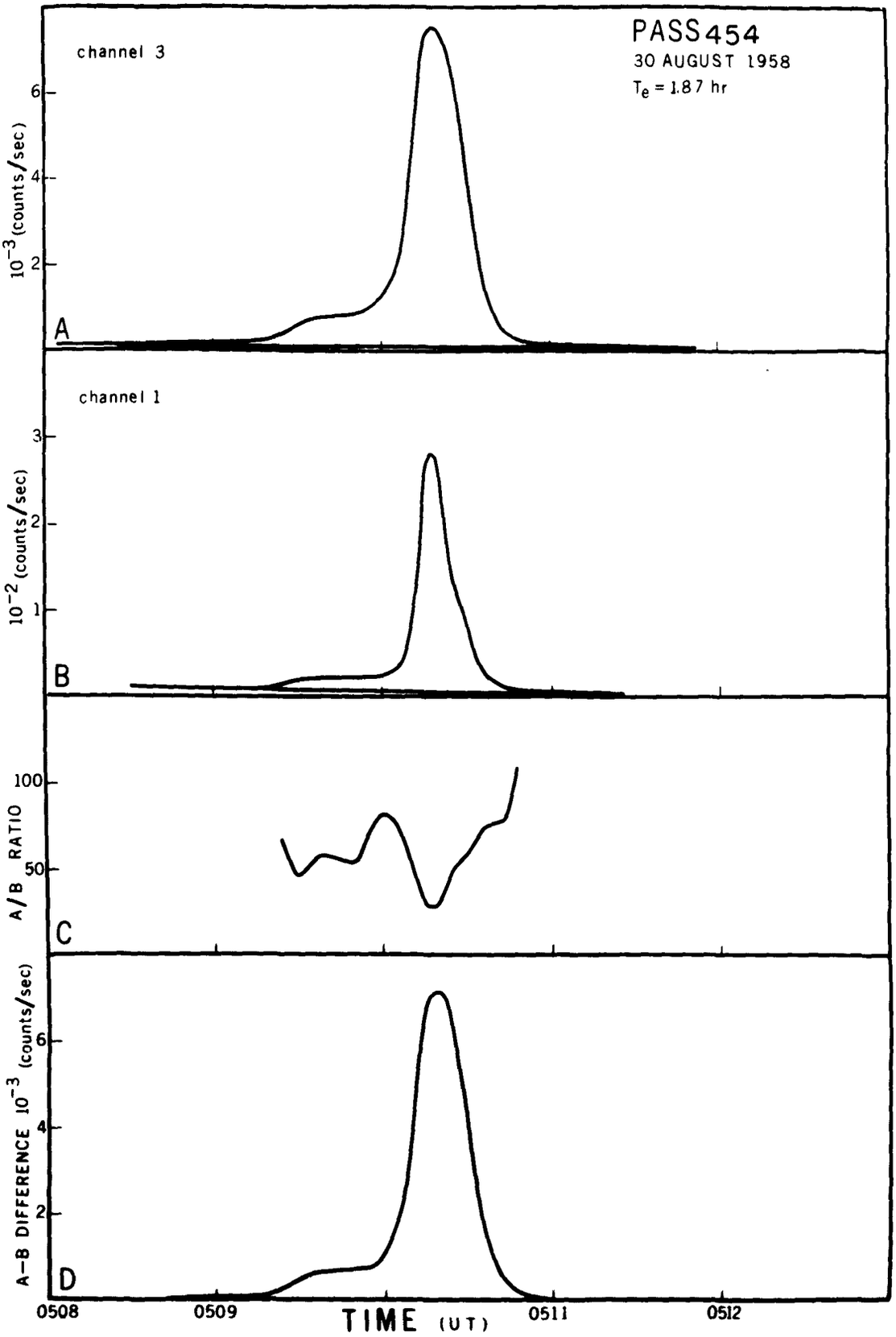
PASS 454
30 AUGUST 1958
T_e = 1.87 hr
channel 3
10^{-3} (counts/sec)
A
channel 1
10^{-2} (counts/sec)
B
A/B RATIO
C
A−B DIFFERENCE 10^{-3} (counts/sec)
D
0508
0509
0511
0512
TIME (UT)

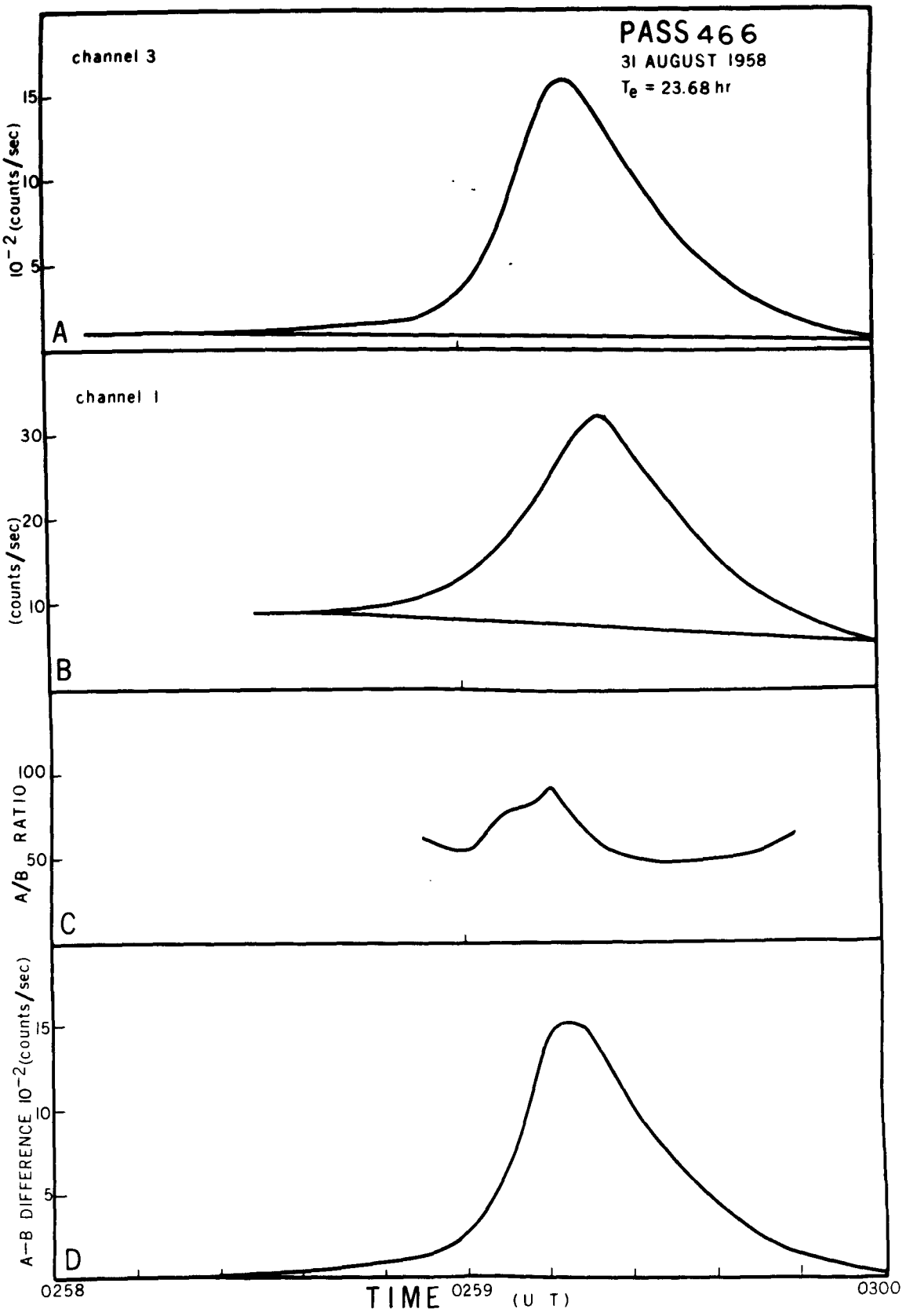
PASS 466
31 AUGUST 1958
T_e = 23.68 hr
channel 3
10^{-2} (counts/sec)
15
10
5
A
channel 1
(counts/sec)
30
20
10
B
A/B RATIO
100
50
C
A–B DIFFERENCE 10^{-2}(counts/sec)
15
10
5
D
0258
0259
0300
TIME (U T)

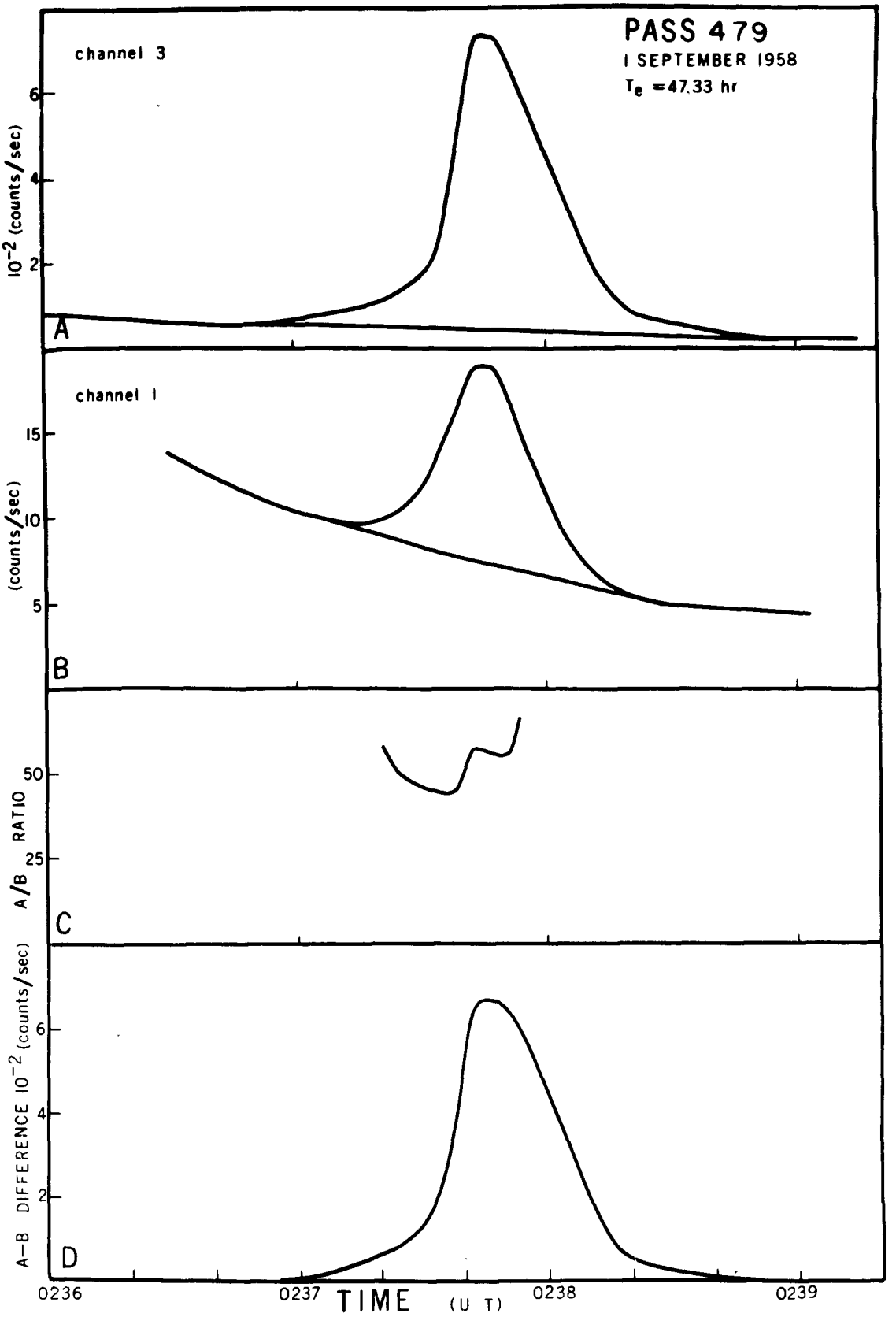
PASS 479
1 SEPTEMBER 1958
T_e =47.33 hr
channel 3
10^{-2} (counts/sec)
6
4
2
A
channel 1
(counts/sec)
15
10
5
B
A/B RATIO
50
25
C
A-B DIFFERENCE 10^{-2} (counts/sec)
6
4
2
D
0236
0237
TIME (U T)
0238
0239

Fig. 5.3 Decay of ARGUS shell vs time elapsed T_e since Event I for various L (McIllwain B-L geomagnetic coordinates) values. The plotted points are true (corrected) omnidirectional count-rates of the unshielded G-M counter (Detector C, Channel 3) during ARGUS shell Event I penetrations of several Explorer IV Passes. The count-rates are differences between total and background count-rates due to electrons (assuming β-particle trapping) of energy greater than 3 MeV.

Data for Passes 492 and 505 were taken from (Report, State University of Iowa, 1959) L values were obtained of GE TEMPO, Santa Barbara, California through the offices of Major Charles W. Hulbert, Defense Atomic Support Agency.

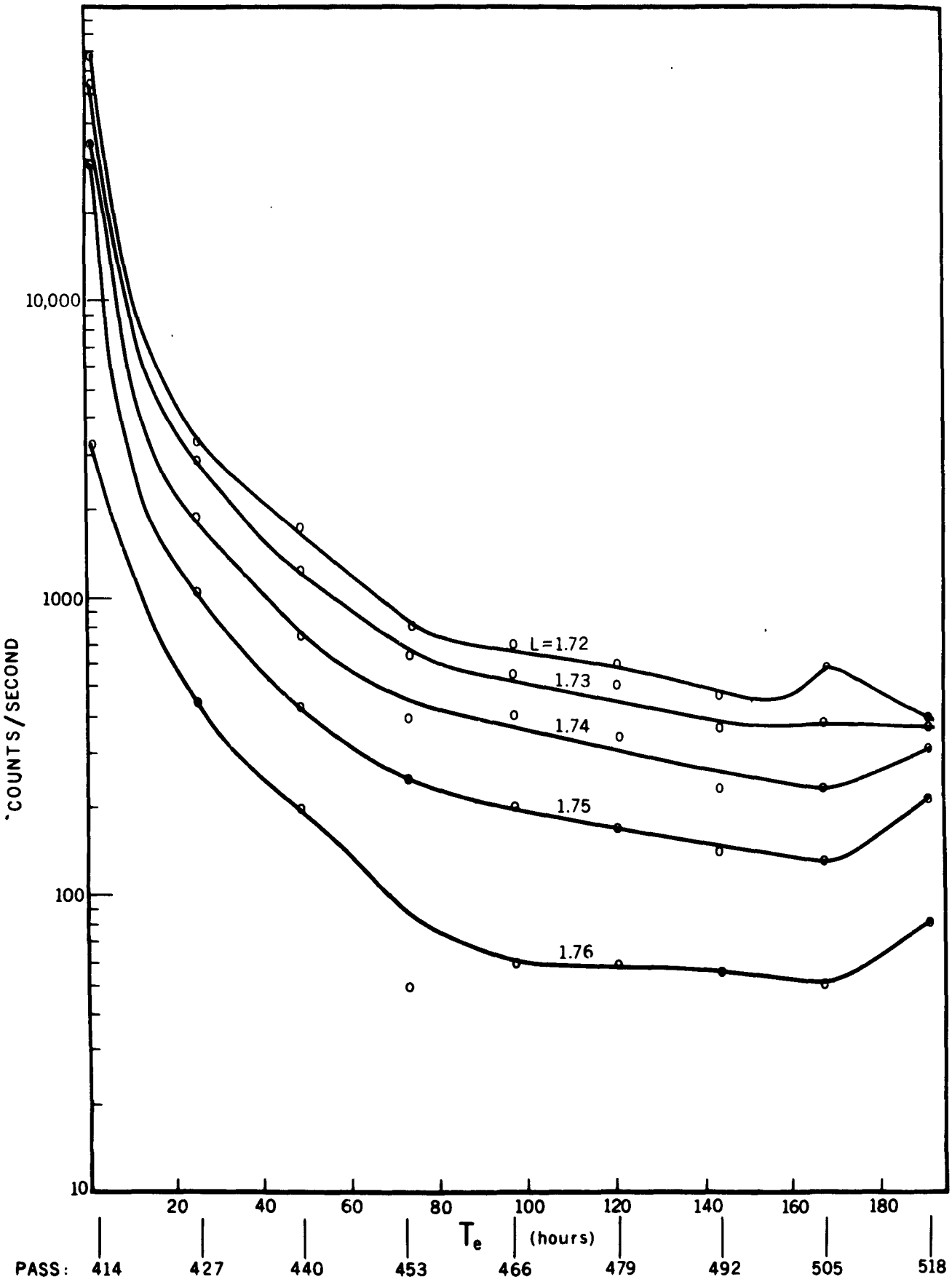
10,000
1000
100
10
COUNTS/SECOND
L=1.72
1.73
1.74
1.75
1.76
20
40
60
80
100
120
140
160
180
T_e (hours)
PASS: 414
427
440
453
466
479
492
505
518

Fig. 5.4 Decay of ARGUS shell vs time elapsed T_e since Event I for the Ratio of A (unshielded G-M counter)/B (shielded G-M counter) omnidirectional count-rates, for various L values and Passes of Explorer IV during ARGUS shell Event I penetrations.

The Ratios are of total count-rates minus background. For Pass 479 (not shown, but refer Fig. 5.3) no counts above background were observed.

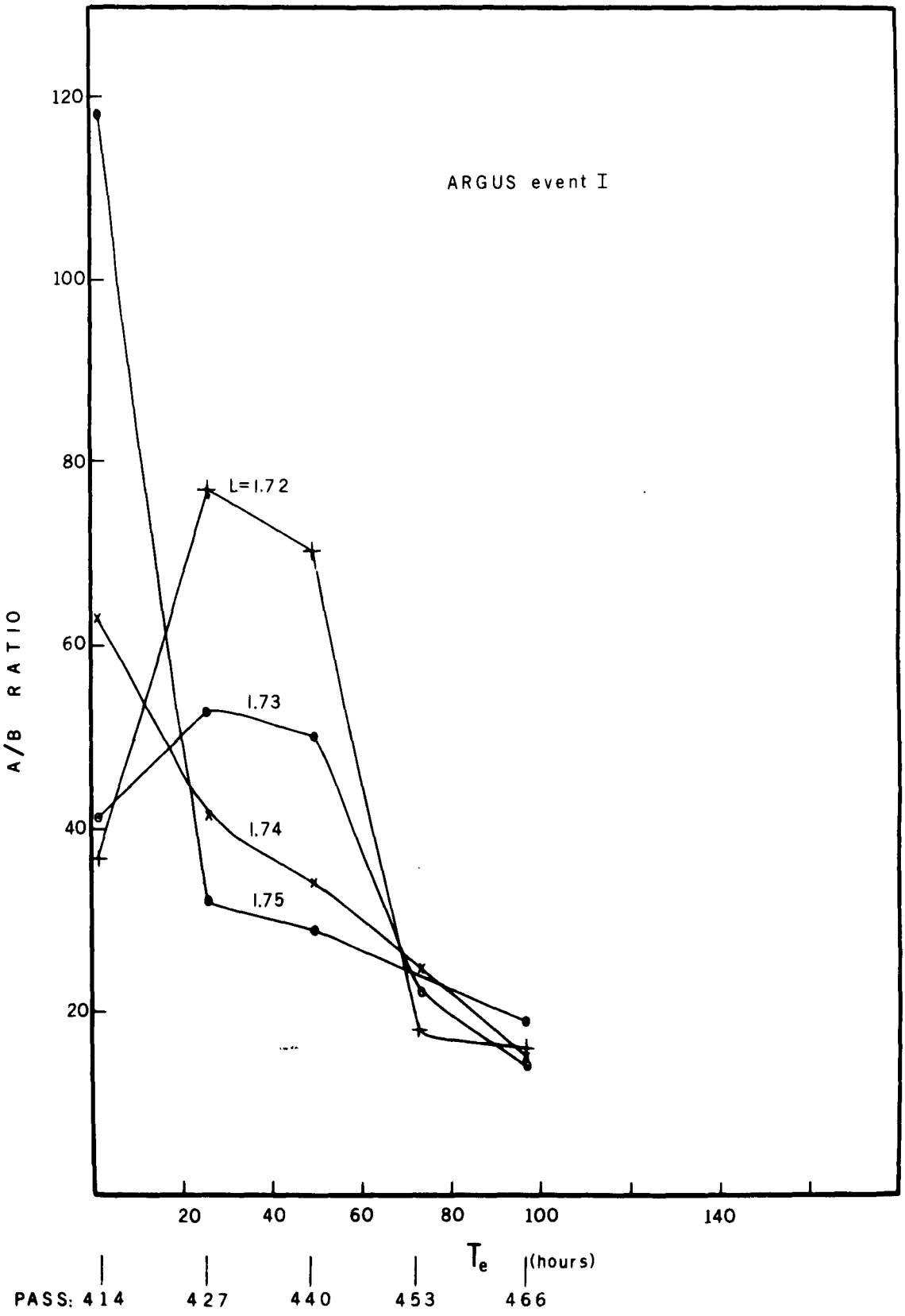
ARGUS event I
A/B RATIO
120
100
80
60
40
20
L=1.72
1.73
1.74
1.75
20
40
60
80
100
140
T_e (hours)
PASS: 414
427
440
453
466

Fig. 5.5 Decay of ARGUS shell vs time elapsed T_e since Event II for various L values. The plotted points are true (corrected) omnidirectional count-rates of the unshielded G-M counter (Detector C, Channel 3) during ARGUS shell Event II penetrations of several Explorer IV Passes. The count-rates are differences between total and background count-rates due to electrons (assumed) of energy greater than 3 MeV.

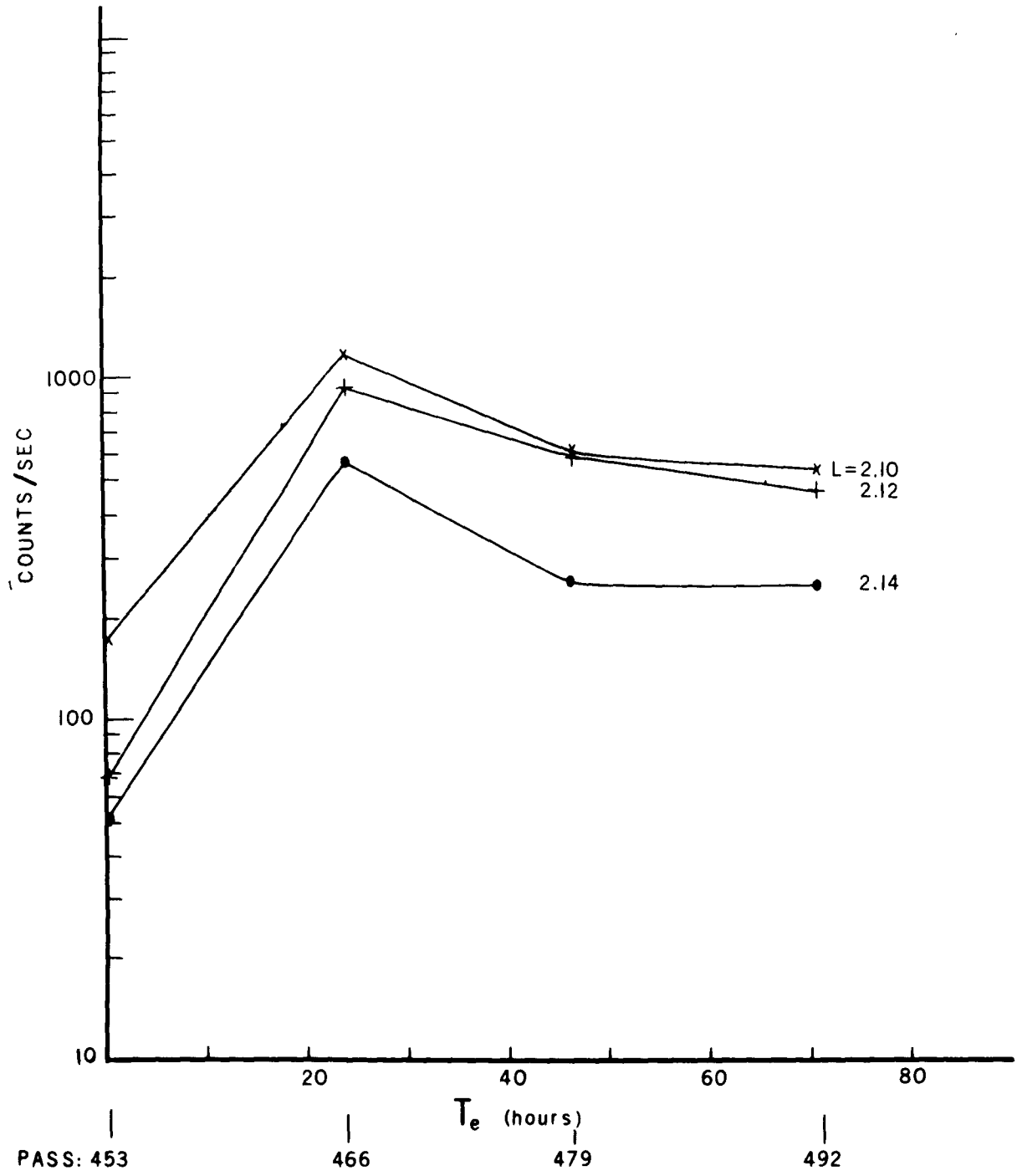
1000
100
10
COUNTS/SEC
L=2.10
2.12
2.14
20
40
60
80
T_e (hours)
PASS: 453
466
479
492

References

J. K. Bock, "Directional Dependency of Trapped Radiation After the First Nuclear High Altitude Detonation (ARGUS) as Measured by Explorer IV (1958 Epsilon)," Preliminary version of Final Report to Defense Atomic Support Agency (1964), Ballistic Research Laboratory, Aberdeen, Maryland (1964).

E. O. Baicy, J. Bock, and T. R. Jeter, "The ARGUS Experiment Calibration of Explorer IV Prototype," Defense Atomic Support Agency Report WT-1671, Ballistic Research Laboratory, Aberdeen, Maryland (1963).

H. T. Motz, and R. E. Carter, "Artificial Radiation Belt Studies with a Fission Beta-Ray Source," J. Geophys. Research, 68, 657-661 (1963).

J. A. Van Allen, L. A. Frank, and B. J. O'Brien, "Satellite Observations of the Artificial Radiation Belt of July 1962," J. Geophys. Research 68, 619-627 (1963).

R. J. Naumann, "Observed Torque-Producing Forces Acting on Satellites," (Paper presented at the International Union of Theoretical and Applied Mechanics Symposium International sur la Dynamique de Satellites, Paris France, May 28-30, 1962).

C. Lundquist, R. Naumann, and A. H. Weber, "Directional Flux Densities and Mirror Point Distribution of Trapped Particles from Satellite 1958 Epsilon Measurement," J. Geophys. Research 67, 11, 4125-4133 (1962).

R. J. Naumann, "Directional Dependence of Counting Rates from Explorer IV," Master's Thesis, Physics Department of the Graduate School of the University of Alabama, May (1961).

R. J. Naumann, "Recent Information Gained from Satellite Orientation Measurement," (Paper presented at the 4th Symposium on Ballistic Missiles and Space Technology at UCLA, Los Angeles, California, 24-27 August 1959), Proceedings published Permagon Press Oxford (1961).

S. Fields, "Body Motions of 1958 Epsilon," Army Ballistic Missile Agency, Tech Memo C1-TM-11-60 (1960).

M. L. Baker and M. W. Makemson, An Introduction to Astrodynamics, Academic Press, New York, N. Y. (1960).

R. E. Carter, F. Reines, J. J. Wagner, and M. E. Wyman, "Free Anti-neutrino Absorption Cross-Section, Z, Expected Cross-Section From Measurements of Fission Fragment Electron Spectrum," Phys. Rev. 113, 280-286 (1959).

W. C. Snoddy, "Theoretical and Measured Temperatures of Explorer IV," Report DV-TN-6-59, Thermodynamics Section, Research Projects Laboratory Development Operations Division, Army Ballistic Missile Agency, Huntsville, Alabama (1959). Limited circulation copy available ORDAB-DIR Missile File, or A. H. Weber, Saint Louis University, St. Louis, Missouri.

J. A. Van Allen, C. E. McIllwain, and G. H. Ludwig, "Radiation Observations with Satellite 1958E," J. Geophys. Research 64, 271-286 (1959a).

J. A. Van Allen, C. E. McIllwain, and G. H. Ludwig, "Satellite Observations of Electrons Artificially Injected into the Geomagnetic Field," J. Geophys. Research 64, 877-891 (1959b).

State University of Iowa Report SUI 59-28, "ARGUS I, II and III Observations with Explorer IV Satellite (Supplemental Report)," Iowa City, Iowa (1959).

Army Ballistic Missile Agency, Huntsville, Alabama, and Smithsonian Astrophysical Observatory, Cambridge, Massachusetts Report Explorer IV - 1958 Epsilon Orbital Data Series, Issue 6, 6 Vols. (1959).

H. Goldstein, Classical Mechanics, Addison-Wesley, Reading, Massachusetts (1959).

R. B. Blackman and J. W. Tukey, "The Measurement of Power Spectra, Dover, N. Y. (1958).

S. A. Husain, and J. L. Putnam, Proc. Phys. Soc. (London), A, 70, 304 (1957).

J. C. Slater, and N. H. Frank, Mechanics, McGraw Hill, New York, N. Y. (1947).

J. S. Marshall, and A. G. Ward, "Absorption Curves and Ranges for Homogeneous β-Rays," Can. J. Research, V. 15-A, 39-41 (1937).

APPENDIX 1

Power Spectrum

The present appendix includes an analysis of the roll or spin period "anomaly" discussed briefly in Sec. 3.3 and noted by Fig. 3.3. J. Bock (private communication, 1964) suggested that the anomalous decrease followed by increase in the roll period observed by Naumann (1961) might be the result of mistaking beat rates, between roll and tumble motion such as $|\dot{\phi} - 2\dot{\psi}|$ for roll rate $\dot{\psi}$. To evaluate this hypothesis, a trigonometric series analysis of the Detector A count-rate vs time was carried out for the time interval of interest, Passes 414, 427 and 454. Basically the theory involved is as follows (Blackman, 1958).

If a function X(t) is defined for all times t in the interval T in which periodicities are to be investigated, the power spectrum function, P(f) can be written

$$P(f) = \lim_{T \to \infty} 1/T \left| \int_{-T/2}^{T/2} X(t)\, e^{-i2\pi ft}\, dt \right|^2 . \qquad \text{(A1.1)}$$

The frequencies at which the maxima of P(f) occur yield the periodicities of X(t). An alternate method of calculating P(f) involves the autocorrelation function $C(\tau)$ defined as

$$C(\tau) = \lim_{T \to \infty} 1/T \int_{-T/2}^{T/2} X(t) X(t+\tau)\, dt, \qquad \text{(A1.2)}$$

where τ is called the lag time. Also, P(f) is the Fourier transform of $C(\tau)$ and so may be written

$$P(f) = \int_{-\infty}^{\infty} C(\tau)\, e^{-i2\pi f\tau}\, d\tau \,. \qquad \text{(A1.3)}$$

For functions X(t) which are defined for a finite time interval but not for all t (for example, the Detector A count rate function), an apparent autocovariance function $C_o(\tau)$ may be defined as

$$C_o(\tau) = 1/(T_m - |\tau|) \int_{-(T_m-|\tau|)/2}^{(T_m-|\tau|)/2} X(t-\tau/2)\, X(t+\tau/2)\, dt\,; \quad |\tau| < T_m, \qquad \text{(A1.4)}$$

and

$$C_o(\tau) = 0;\ \text{for } |\tau| > T_m\,;$$

where $T_m < T_n$ (typically T_m is $T_n/10$). Considering Eq. (A1.4), Eq. (A1.3) can be expressed as

$$P_o(f) = \int_{-T_m}^{T_m} C_o(\tau)\, e^{-i2\pi f\tau}\, d\tau \,. \qquad \text{(A1.5)}$$

Equation (A1.3) applied to a very long record containing sinusoidal variations with time of discrete frequencies f_k ($k = 1,2,\ldots$) would yield P(f) as a series of delta-function spikes at these discrete frequencies. The effect of using records of finite length is to broaden these sharp spikes, so that they appear in the form (sin x)/x where

$$X = 2\pi (f - f_k) T_m \,. \tag{A1.6}$$

The function (sin x)/x is symmetric about x = 0 with maxima at x = 0, 7.725, 14.066, 20.371, ... of corresponding amplitudes 1, 0.1284, 0.0709, 0.0490, ...

In the present case the integrals were approximated by finite sums with

$$C'_r = 1/(n-r) \sum_{i=0}^{n-r} X'_i \; X'_{i+r} \; ; \; r = 0,1,\ldots m, \tag{A1.7}$$

where

$\tau_r = r\Delta\tau,$

$\tau_m = m\Delta\tau,$

$\tau_n = n\Delta\tau,$

and

$$X'_i = X_i - \overline{X}, \quad \text{where} \quad X_i = X_i(i\Delta t) \,, \tag{A1.8}$$

in which $\bar{X}$ is the average count-rate defined as

$$\bar{X} = 1/n \sum_{i=1}^{n} X_i \qquad \text{(A1.9)}$$

Subtraction of $\bar{X}$ in Eq. (A1.8) has the effect of reducing the zero frequency peak in the power spectrum.

To interpret the power spectrum, it is noted that Eq. (3.11) namely

$$\theta = \arcsin \left[b_1 \sin(\dot{\psi} t + \delta) - b_2 \sin(\dot{\phi} t + \gamma) \cos(\dot{\psi} t + \delta) + b_3 \cos(\dot{\phi} t + \gamma) \cos(\dot{\psi} t + \delta) \right] \qquad \text{(3.11)}$$

combined with the empirical count-rate function used by Bock (op. cit. 1964)

$$C_{obs} = (C_{obs})_o \cos^4 \theta \qquad \text{(A1.10)}$$

yield an empirical analytic expression for C_{obs} vs time (see Figs. 2.9 and 2.10).

Thus C_{obs} vs t (Figs. 2.9 and 2.10 Lower) can be expressed in a linear series of trigonometric functions and the squares of the amplitudes of these terms should be directly proportional to the intensities for the frequencies observed in the directional count-rate data and also to the intensities resulting from the power spectrum analysis assuming a $\cos^4\theta$ distribution of particle flux. Twenty frequencies, each a linear combination of the tumble rate $\dot{\phi}$ and roll or spin rate $\dot{\psi}$

and whose amplitudes are not zero were obtained from the expansion of $\cos^4\theta$. The rates $\dot{\psi}$, $\dot{\phi}$, $3\dot{\psi}$ and $3\dot{\phi}$ have zero amplitudes and thus should not appear in the power spectrum. The intensities corresponding to the remaining frequencies are a function of $b_1 = \hat{B}\cdot\hat{L}$ only (see Sec. 3.1). These frequencies and relative intensities are listed in Table A1.

Table A1 shows that dominant frequencies are $2\dot{\phi}$, $2\dot{\psi}$, $\dot{\phi}+2\dot{\psi} = f_+$, $|\dot{\phi}-2\dot{\psi}| = f_-$. The relative intensities corresponding to these frequencies are plotted as a function of b_1 in Fig. A1. Figure A1 shows that when $b_1 = 0$ $[\arccos(B\cdot L) = 90°]$ both the $2\dot{\phi}$ and $2\dot{\psi}$ terms have equal intensity while the f_+ and f_- terms have zero intensity. As the angle between $\hat{L}$ and $\hat{B}$ decreases from 90° to 0° or increases from 90° to 180° the intensity for $2\dot{\phi}$ decreases monotonically to zero which is to be expected when $\arccos(\hat{B}\cdot\hat{L})$ approaches 0° or 180° in which cases b_2 and b_3 go to zero and b_1 goes to unity. By Eq. (3.11), if $b_2 = b_3 = 0$, θ is independent of ϕ and $b_1 = \pm 1$ and physically the count-rate would show no variation due to rotation about $\hat{L}$. It is also clear by Table A1 that for $b_1^2 = 1$ all intensities involving $\dot{\phi}$ go to zero and $2\dot{\psi}$ and $4\dot{\psi}$ alone are present.

The behavior of the intensity for frequency $2\dot{\phi}$ was thus expected physically. However the variation of the intensities of $2\dot{\psi}$, f_+, and f_- with b_1 could not be anticipated from physical considerations. It is seen (Fig. A1) that the intensity for $2\dot{\psi}$ decreases to zero for a value of about .553 for b_1; this corresponds to $\arccos(B\cdot L)$ about 56.5°. The intensity for $2\dot{\psi}$ then rises to a very large value

for $b_1 = 1$. The behavior of the intensities for $f_+ = \dot{\phi} + 2\dot{\psi}$ and $f_- = |\dot{\phi} - 2\dot{\psi}|$ is almost the reverse. They are zero at $b_1 = 0$ and 1 and are a maximum for b_1 about .668 corresponding to $\arccos(\hat{B} \cdot \hat{L})$ about 49°. Since this latter intensity is near its maximum when the intensity for $2\dot{\psi}$ is zero, it is seen that the frequencies f_+ and f_- are dominant over $2\dot{\psi}$ in the range $.33 < b_1 < .79$; while for b_1 outside this range, $2\dot{\psi}$ is the dominating frequency.

For Pass 454 during the time interval from 300.0-305.0 UT b_1 was calculated to vary from .01 to 0.36. It was during this interval that the long term periodicities mentioned by Naumann (1961) representing $2\dot{\psi}$ were measured. Figure A1 shows that $2\dot{\psi}$ should be the dominating frequency. However for Pass 414, b_1 was calculated to vary from 0.33 to 0.70 in the interval from 250.0-255.0 UT, Fig. A1 shows that $|\dot{\phi} \pm 2\dot{\psi}|$ would be the dominating frequency. In Fig. 3.3 the frequency $|\dot{\phi} - 2\dot{\psi}|$ is plotted with squares for Pass 414, 427, and 453.

The appearance of harmonic or beat frequencies in the count-rate vs time data appears to account for the apparent anomalous behavior of the roll period vs time as determined by Naumann and plotted as circle points in Fig. 3.3 (in the interval August 24-29 approximately). J. Bock (private communication, 1964) identified the dominant frequency in the anomalous region as $|\dot{\phi} - 2\dot{\psi}|$ rather than $2\dot{\psi}$ and the present analysis agrees with his identification.

An example of the power spectrum analysis is given by Fig. A2 for Pass 414 which falls within the region of apparent anomalous behavior.

The frequencies and relative intensities of the dominant peaks are

peak	frequency (cycles sec^{-1})	relative intensity
1	0.0080	703
2	0.0430	618
3	0.0628	141
4	0.1859	108
5	0.2935	138
6	0.3306	296
7	0.4792	114

Peak 1 is not physical but results from the finite range of integration over τ . Side lobes of peak 1 (due to the $\frac{\sin x}{x}$ behavior discussed above) appear to have interfered with peak 2 increasing its intensity somewhat. Peak 3 is interpreted as a side lobe of peak 2 since a side lobe calculated by Eq. (A1.6) occurs for f = 0.0635. Peak 5 is at the frequency corresponding to $2\dot{\phi}$ the tumble period being about 7 seconds. Since peak 6 appears at a larger frequency than for $2\dot{\phi}$ and has a greater intensity than for $2\dot{\phi}$ it must be interpreted as associated with the frequency $\dot{\phi}+2\dot{\psi}$ because $2\dot{\psi}$ never exceeds $2\dot{\phi}$ for Explorer IV after the propeller-like motion is established, and from Fig. A1 no other frequency could exceed that for $2\dot{\phi}$ in intensity except at large values of b_1 when the $2\dot{\phi}$ peak would be buried in noise. Peak 6 could not be associated with $|\dot{\phi}-2\dot{\psi}|$ since if $\dot{\psi} < \dot{\phi}$ one can show $|\dot{\phi}-2\dot{\psi}| < \dot{\phi}$ The interpretations of peaks 5 and 6 of Fig. A2 yield

$\dot{\phi}$ tumble frequency = 0.1468 cycles sec^{-1}

$\dot{\psi}$ roll (or spin) frequency = 0.0919 cycles sec^{-1} (A1.11)

From Eq. (A1-11), as a cross check

frequency corresponding to $|\dot{\phi}-2\dot{\psi}|$ = 0.0371 cycles/sec

frequency corresponding to $2\dot{\psi}$ = 0.1838 cycles/sec

frequency corresponding to $2\dot{\phi}+2\dot{\psi}$ = 0.4774 cycles/sec (A1.12)

The assignments above allow the identification of peak 2 (.0430 cycles sec^{-1}) as due to $|\dot{\phi} - 2\dot{\psi}|$, peak 4 (.1859 cycles sec^{-1}) as due to $2\dot{\psi}$ and peak 7 (.4792 cycles sec^{-1}) as due to $2\dot{\phi} + 2\dot{\psi}$ The values of Eq. (A1.11) compare with Bock's more accurate values for Pass 414 as follows

$\dot{\phi}$ tumble frequency = 0.14490 cycles sec^{-1}

$\dot{\psi}$ roll (or spin) frequency = 0.09382 cycles sec^{-1} (A1.13)

From Eqs. (A1.11) and (A1.13), it is seen that about a 2 percent difference exists. Using Bock's values, Eq.(A1.13), yields for frequency corresponding to $2\dot{\psi} - \dot{\phi}$ = 0.0427, in much better agreement with the peak 2 value than as stated by Eq. (A1.12). However the frequencies obtained by a power spectrum analysis would be close enough to the correct values to be useful as starting parameters in the "closure search" procedure described in Sec. 3.3.

It appears possible also to perform an orientation analysis with the power spectrum. If a separate power spectrum were computed for each minute of a pass, and the relative intensities of the relevant peaks examined by use of Fig. A1, an average b_1 for that minute could be obtained. A plot of b_1 vs time then could be made and a determination of the absolute direction of $\hat{L}$ carried out. Such procedure would be the same type as done by Bock (1964) except that he used an analog device in which only count rate maxima were involved. The method here described would use all the data and might possibly yield better results, that is if the signal-to-noise ratio were large enough. Figure A2 is the power spectrum for the entire Pass 414 consequently the intensities have been averaged over about 9 minutes, during which b_1 varies from 0.3 to about 0.8.

Table A1. Harmonics and beat frequencies of tumble rate $\dot{\phi}$ and roll (or spin) rate $\dot{\psi}$ obtained by expansion of $\cos^4\theta$ (Eq. (3.11)) in a Fourier type series.

Harmonics and beat frequencies	Calculated intensity
$2\dot{\phi}$	$I_1 = 1/2^8\ (1-b_1^2)^2\ (5-3b_1^2)^2$
$4\dot{\phi}$	$I_2 = 9/2^{12}\ (1-b_1^2)^4$
$2\dot{\psi}$	$I_3 = 1/2^8\ \ 5-18b_1^2 + 5b_1^4\ ^2$
$4\dot{\psi}$	$I_4 = 1/2^{12}\ \ 3-30b_1^2 + 35b_1^4\ \ ^2$
$\dot{\phi}+2\dot{\psi} = f_+$	$I_5 = 1/2^6\ b_1^2\ (1-b_1^2)\ (5-b_1^2)^2$
$\lvert\dot{\phi} - 2\dot{\psi}\rvert = f_-$	$I_6 = I_5$
$\dot{\phi} + 4\dot{\psi}$	$I_7 = 1/2^6\ b_1^2\ (1-b_1^2)(3-7b_1^2)^2$
$\lvert\dot{\phi} - 4\dot{\psi}\rvert$	$I_8 = I_7$
$2\dot{\phi}+2\dot{\psi}$	$I_9 = 1/2^6\ (1-b_1^2)^2\ (1+b_1^2)^2$
$\lvert 2\dot{\phi} - 2\dot{\psi}\rvert$	$I_{10} = I_9$
$2\dot{\phi}+4\dot{\psi}$	$I_{11} = 1/2^{10}\ (1-b_1^2)^2\ (1-7b_1^2)^2$
$\lvert 2\dot{\phi} - 4\dot{\psi}\rvert$	$I_{12} = I_{11}$
$3\dot{\phi} + 2\dot{\psi}$	$I_{13} = 1/2^6\ b_1^2\ (1-b_1^2)^3$
$\lvert 3\dot{\phi} - 2\dot{\psi}\rvert$	$I_{14} = I_{13}$
$3\dot{\phi}+4\dot{\psi}$	$I_{15} = 1/2^8\ b_1^2\ (1-b_1^2)^3$
$\lvert 3\dot{\phi}-4\dot{\psi}\rvert$	$I_{16} = I_{15}$
$4\dot{\phi}+2\dot{\psi}$	$I_{17} = 1/2^{10}\ (1-b_1^2)^4$
$\lvert 4\dot{\phi}-2\dot{\psi}\rvert$	$I_{18} = I_{17}$
$4\dot{\phi}+4\dot{\psi}$	$I_{19} = 1/2^{14}\ (1-b_1^2)^4$
$\lvert 4\dot{\phi}-4\dot{\psi}\rvert$	$I_{20} = I_{19}$

Fig. A1. Several harmonic and beat frequency intensities, from Table A1, vs b_1. The frequencies involved are $A, 2\dot{\phi}$; $B, 2\dot{\psi}$; $D, |\dot{\phi} \pm 2\dot{\psi}|$; $C, |2\dot{\phi} \pm 2\dot{\psi}|$. The ordinates have been multiplied by 2^{12}.

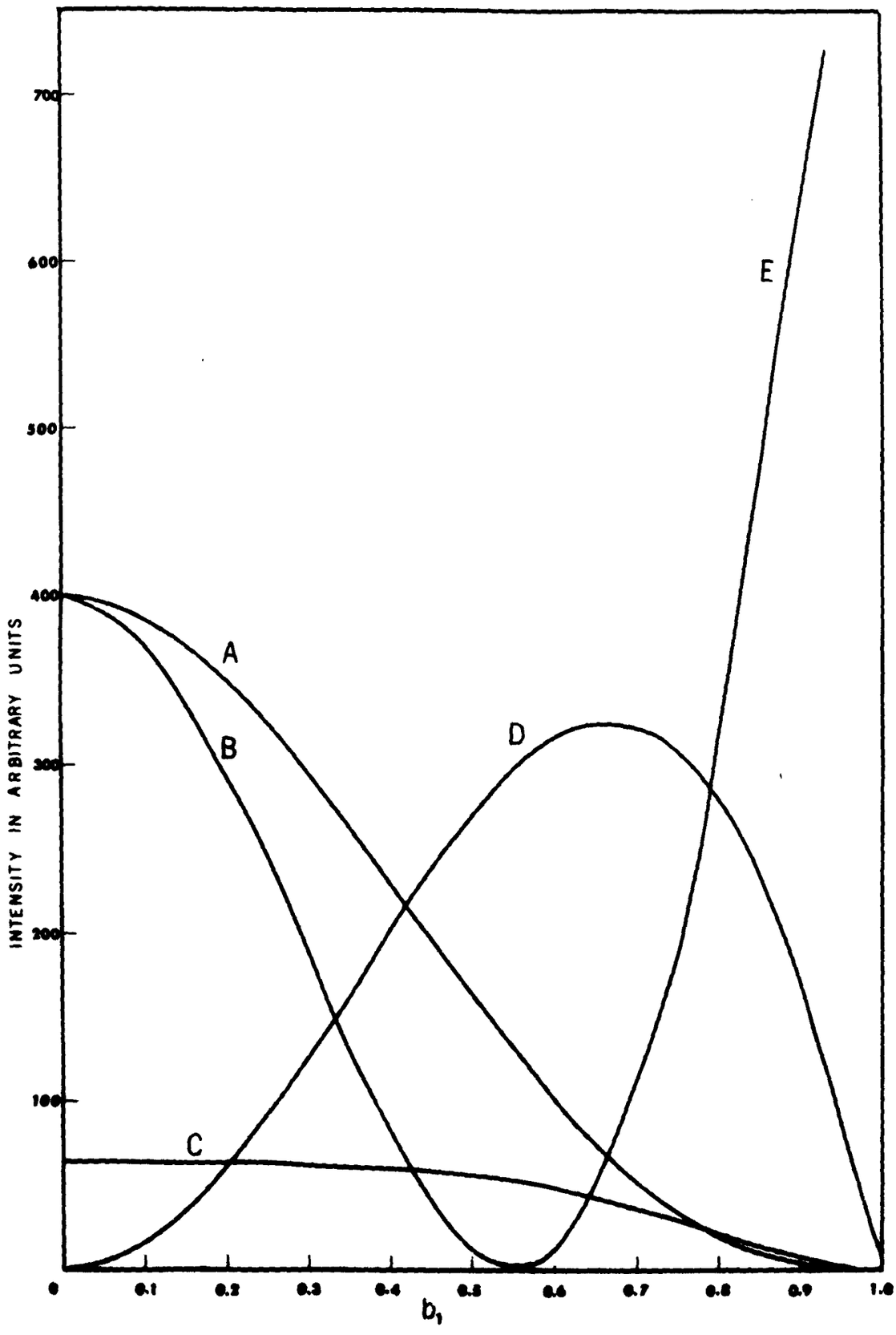
700
600
500
400
300
200
100
0
0.1
0.2
0.3
0.4
0.5
0.6
0.7
0.8
0.9
1.0
INTENSITY IN ARBITRARY UNITS
b_1
A
B
C
D
E

Fig. A.2 Power Spectrum Analysis for Pass 414. Relative power or intensity P(f) is plotted vs tumble and roll (or spin) beat frequencies or harmonics. The numbered peaks, 1 to 7, are explained in the text.

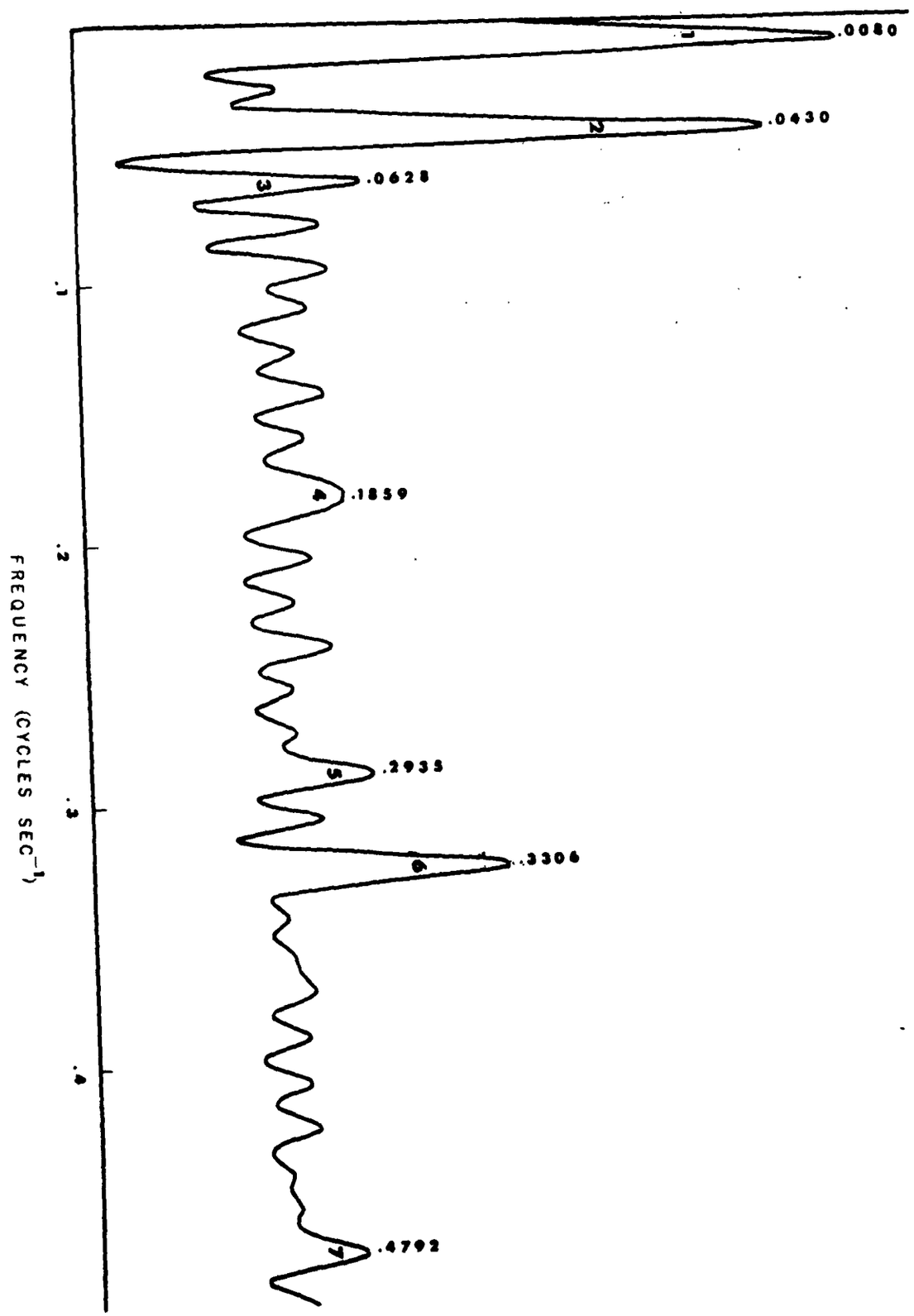
P(f) RELATIVE UNITS
1
.0080
2
.0430
3
.0628
4
.1859
5
.2935
6
.3306
7
.4792
.1
.2
.3
.4
FREQUENCY (CYCLES SEC^{-1})

Distribution List

1. Director, U. S. Army Ballistic Research Laboratories, ATTN: Mr. Ed Baicy, Aberdeen Proving Ground, Maryland 21005

2. Commanding Officer, U. S. Army Research Office - Durham, Box CM, Duke Station, ATTN: Dr. R. Mace, Durham, North Carolina 27706

3. AFWL ATTN: WLRP; WLRB; WLAX, Kirtland AFB, New Mexico 87117

4. AFCRL ATTN: Dr. L. Katz, L G Hanscom Fld., Bedford, Mass. 01731

5. Director, Goddard Space Flight Center, National Aeronautics and Space Administration, ATTN: Dr. W. Hess (3 cys), Greenbelt, Maryland

5. Director, Advanced Research Projects Agency, Washington, D. C. 20301 (5 cys)

6. DDC Cameron Stn., Alexandria, Virginia (20 cys)

7. Director, Defense Atomic Support Agency, ATTN: Document Library (5 cys); RAEL, Washington, D. C. 20301

8. RAND Corporation, 1700 Main Street, Santa Monica, California, ATTN: Dr. P. Tamarkin

9. Aerospace Corporation, P. O. Box 95085, Los Angeles, California, ATTN: Dr. S. Freden, Dr. J. Vette, Dr. R. Harrison

10. Lockheed Missiles and Space Company, A Division of Lockheed Aircraft Corporation, 1111 Lockheed Way, Sunnyvale, California, ATTN: Dr. M. Walt, Dr. R. Smith, Dr. J. Caldis, Dr. W. Imhof, Dr. R. Meyerott

11. Lawrence Radiation Laboratory, P. O. Box 808, Livermore, California, ATTN: Dr. C. McIlwain, Dr. H. West, N. Christofilos, Dr. G. Bing

12. State University of Iowa, Administration Building, Iowa City, Iowa, ATTN: Document Control Station for Dr. J. Van Allen

13. Bell Telephone Laboratories, Whippany Road, Whippany, New Jersey, ATTN: Dr. W. Brown, Dr. C. Roberts

14. North American Aviation, Space and Information Systems Division, 12214 Lakewood Boulevard, Downey, California

15. The Catholic University of America, Washington, D. C. 20017, ATTN: Dr. C. Chang

Distribution List (continued)

16. General Electric Company, Technical Military Planning Operation, 735 State Street, Santa Barbara, California, ATTN: Dr. R. Hendrick, DASA Data Center (2 cys)

17. IIT Research Institute, 10 West 35th Street, Chicago, Illinois 60616, ATTN: Dr. B. McCormac, Dr. L. Reiffel

18. Los Alamos Scientific Laboratory, P. O. Box 1663, Los Alamos, New Mexico, ATTN: Dr. A. Petchek, Report Librarian

19. General Atomic, A Division of General Dynamics Corporation, P. O. Box 1111, San Diego, California 92112, ATTN: Dr. David B. Chang

20. Director, Applied Physics Laboratory, John Hopkins University, 8621 Georgia Avenue, Silver Spring, Maryland, ATTN: Dr. R. Fischell

21. Air Force Technical Applications Center, Washington 25, D. C., ATTN: Mr. D. Northrup